Coupled Plasmonic Systems and Devices: Applications in Visible Metamaterials, Nanophotonic Circuits, and CMOS Imaging

Thesis by

Stanley P. Burgos

In Partial Fulfillment of the Requirements

for the Degree of

Doctor of Philosophy

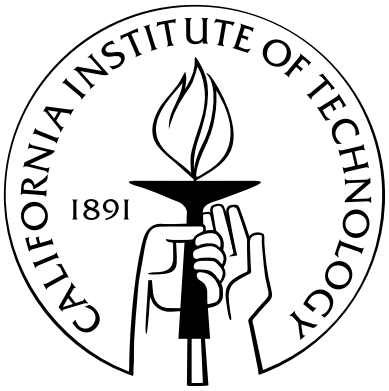

California Institute of Technology

Pasadena, California

2013

(Defended May 21, 2013)

Acknowledgements

I have been fortunate enough to have come across several important people throughout my studies, to whom I would like to convey my deepest appreciation. First on the list is my advisor, Prof. Harry Atwater, for all his support throughout my career as a student at Caltech. Harry has been extremely instrumental in determining the outcome of my studies, having provided me with invaluable advice and encouragement, which have helped shape both my academic and personal life. His dedication, enthusiasm, and positive outlook have definitely helped me aspire throughout my PhD. I am extremely grateful for him having opened the doors to the research playground that is his lab, and for allowing me the freedom to pursue my research interests. I feel extremely fortunate to have had the opportunity to be a part of his lab.

I would also like to thank Profs. Kerry Vahala and Oskar Painter for their invaluable support, guidance, and advice, spanning from my undergraduate to graduate studies at Caltech. It is with the utmost appreciation that I thank them for their willingness to help even in the most inconvenient of circumstances. I likewise thank Professor Keith Schwab for his advice and perspective; he was definitely instrumental in helping me decide my post-doctoral career path. Similarly, I would like to thank my undergraduate professors at Occidental College: Profs. Daniel Snowden-Ifft, George Schmiedeshoff, and Alec Schramm, who were not only excellent professors, but also great advisors and people whom I could always turn to for help. They have positively helped shape the person and researcher I am today. Also, having had the privilege of doing research under the guidance of Prof. Snowden-Ifft, I thank him for being a great advisor on an exciting project; his dedication and guidance has definitely helped me aspire to be the best researcher I can be. Equally, I would like to thank

Profs. Scott Funkhouser and Adrian Hightower for their guidance and support while at Oxy. Professor Hightower's advice was instrumental in my attending Caltech, 'surviving' graduate school, and embarking on the next stage of my research career.

As I started in Harry's group, I was also lucky enough to have worked with Prof. Jennifer Dionne, Dr. Luke Sweatlock, Dr. Carrie Hoffmann, and Dr. Brendan Kayes (all students at the time). Luke, Carrie, and Brendan all facilitated my start with plasmonics and with the Atwater group – Luke helped me get started with computational plasmonics, and Carrie and Brendan helped me get started with electron microscopy. Beyond that, their guidance was absolutely critical in the development of my research career. Also, I had the pleasure of working with Jennifer, who has been one of my role models throughout my graduate career; her perspective and excitement for the theory and application of plasmonics definitely left an impression on me, which has helped lead me to where I am today. I thank her for her guidance and support, as well for teaching me the FIB.

During my graduate studies, I also had the privilege of working with a lot of unique individuals, many of whom I am honored to call my friends. One of those individuals is Dr. Eyal Feigenbaum, who is one of the most intelligent, enthusiastic, and compassionate individuals I know. Eyal, with his critical perspective and genuine excitement for research, has helped me aspire to become a better individual. Similarly, I was extremely fortunate to have shared an office with Prof. Jeremy Munday who showed me that you can be a great researcher while building your own resonator guitar! Also, I had the privilege of overlapping time in the group with Profs. Marina Leite and Deirdre O'Carrol, with whom I shared many an afternoon espresso. Having met them definitely made my studies at Caltech more enjoyable. Similarly, I would also like to thank Prof. Domenico Pacifici for being a good friend, a great mentor, and, additionally, a good gym buddy! Likewise, I would like to thank Prof. Koray Aydin for his advice and support. I was also lucky enough to have overlapped with Dr. Henri Lezec, a person whose mastery of both the field of plasmonics as well as the FIB helped me not only to get started in the field, but also to aspire throughout my PhD. Similarly, I would like to thank Dr. Michael Kelzemberg and Dr. Rob Walters for

their help and support as I started in the Atwater group. Mikes computer knowledge definitely came in handy throughout the computational parts of this thesis.

I would also like to acknowledge Dr. Min Seok Jang, with whom I shared not only an office but also many discussions on our perspectives on research and life. Min's seemingly effortless intelligence and appreciation for leisure time make him one of the most interesting individuals I've had the pleasure of meeting at Caltech. I was also fortunate to have worked with Dr. Ryan Briggs. Ryan helped me get started in KNI and he was kind and talented enough to help fabricate the integrated RGWN network investigated in Chapter 10. Also, toward the end of my studies, I was fortunate to have worked with Dr. Howard Lee, who helped me complete part of the experiments described in Chapter 10. Howards attention to detail and willingness to help was absolutely critical in the completion . I also thank Dr. Ragip Pala for his advice, perspective, kindness, and willingness to help. Equally, I thank Dr. Jonathan Gradidier, Dr. Ruzan Sokhoyan, Dennis Callahan, Seokmin Jeon, and Seyoon Kim for being good friends and people I could to turn to for advice and meaningful discussions.

I would also like to thank several Atwater people for making my stay at Caltech more enjoyable: Nick Batara, Jeff Bosco, Ana Brown, Chris Chen, Naomi Coronel, Michael Deceglie, Carissa Eisler (take care of Bebe), Jim Fakonas, Vivian Ferry, Dagny Fleischman, Cristofer Flowers , Yousif Kelaita, Lise Lahourcade, Krista Langeland, Andrew Leenheer, Josue Lopez, Gerald Miller, Prineha Narang, Georgia Papadakis, Morgan Putnam, Imogen Pryce, Bryce Sadtler, Faisal Tajdar, Raymond Weitekamp, and Kelsey Whitesell.

Working in the Atwater group has also allowed me to work in several international collaborations that have led me to meet some truly amazing individuals. I had the pleasure of working with Prof. Albert Polman and his students Dr. Rene DeWaele, Ruben Maas, and Marie van de Haar. Albert was kind enough to let me work in his lab at AMOLF in the Netherlands, where I had the pleasure of working with Ruben and Marie in work related to Part 1 of this thesis. Similarly, I had the privilege of working with Rene while he was a visiting student in the Atwater group as I started my PhD. I was lucky to have shared an office with him and there found that we

shared many of the same perspectives on research and life, making for a fun and fruitful collaboration (described in Part 1). Rene definitely helped me get started with research and aided in setting the course of my thesis. I would also like to thank Profs. Ewold Verhagen and Femius Koenderink for their guidance and support as well as Piero Spinelli, Rutger Thijssen, Toon Coenen, Claire van Lare, Jorik van de Groep, and Benjamin Brenny for welcoming me to their lab and showing me around Amsterdam.

Similarly, I have had the privilege of working with Prof. Ulf Peschel and his students Arian Kriesh and Daniel Ploβ. Arian came from Prof. Peschels lab to work in the Atwater group for a couple of months in 2010, and it was then that I learned about the amazingly motivated and intelligent person that he is. Then, about a year later, Prof. Peschel was kind enough to invite me to work in his lab in Germany. There I met Daniel Ploβ, Sarina Wunderlich, and Sabina Dobmann, some of the most friendly and intelligent people I've had the pleasure of meeting. I would also like to thank Hannes Pfeif, Alois Regensburger,Vincent Schultheiβ, and Ali Mahdavi for welcoming me to their lab and showing me around Germany. Also, I would like to thank Prof. Peter Banzer, Thomas Bauer, and Uwe Mick for their hospitality during my visit to Germany.

I also had the privilege of working with Dr. Sozo Yokogawa, a researcher from Sony who visited our group for a year in 2010, looking for ways to use plasmonics in combination with Sony's CMOS IS technology. The work that came out of that collaboration is discussed in Part 2 of this thesis. Sozo is one of the nicest, most hardworking, and intelligent individuals that I know, and I feel fortunate to have worked with him.

I would also like to thank several people, without whom many of the devices presented in this thesis would not be possible: Bophan Chhim, Guy de Rose, Melissa Melendes, Nils Asplund, Ali Ghaffari, and Jim Lacy. I would also like to thank the amazing administrative support both inside and outside of the Atwater group, consisting of April Niedholdt, Lyra Haas, Jennifer Blankenship, Tiffany Kimoto, Christy Jenstead, Connie Rodriguez, Rosalie Rowe, and Eleonora Vorobief. April was amaz-

ing at helping Harry manage a group as large as ours; her positive energy and support definitely reflected in the group dynamics. Similarly, Jennifer and Tiffany did a great job at filling in her shoes – I thank them for putting up with me and for making my last years at Caltech more enjoyable.

And of course, this thesis would not be possible without the support of my family. I would like to thank Vanessa for all her support while I worked at completing my studies. Similarly, I would like to thank all her family for the support they have provided me throughout all these years. And lastly, I would like to thank my mom, grandma, and family for always believing in me. This thesis is as much an accomplishment for all of them as it is for me.

I would finally like to thank the NSF Graduate Fellowship program for helping me get started on my PhD career. Similarly, I would like to thank everyone else who made my stay at Caltech more enjoyable and successful, namely the staff of the Financial Aid and Registrars Office, as well as that of Brown Gym, the Health Center, and Chandler. These people are the unsung heroes of Caltech, working behind the scenes to make for a smooth infrastructure so that we can do the science that we love. Lastly, I would like to thank Oxy and Caltech for giving me such a great experience in going from a 3/2 Physics undergraduate at Occidental to a graduate student at Caltech. If I could do it all again, I probably wouldn't change a thing, for it is those experiences, both positive and negative alike, that have led me to where I am today.

Stanley P. Burgos

May 2013

Pasadena, CA

Abstract

With the size of transistors approaching the sub-nanometer scale and Si-based photonics pinned at the micrometer scale due to the diffraction limit of light, we are unable to easily integrate the high transfer speeds of this comparably bulky technology with the increasingly smaller architecture of state-of-the-art processors. However, we find that we can bridge the gap between these two technologies by directly coupling electrons to photons through the use of dispersive metals in optics. Doing so allows us to access the surface electromagnetic wave excitations that arise at a metal/dielectric interface, a feature which both confines and enhances light in subwavelength dimensions – two promising characteristics for the development of integrated chip technology. This platform is known as plasmonics, and it allows us to design a broad range of complex metal/dielectric systems, all having different nanophotonic responses, but all originating from our ability to engineer the system surface plasmon resonances and interactions. In this thesis, we demonstrate how plasmonics can be used to develop coupled metal-dielectric systems to function as tunable plasmonic hole array color filters for CMOS image sensing, visible metamaterials composed of coupled negative-index plasmonic coaxial waveguides, and programmable plasmonic waveguide network systems to serve as color routers and logic devices at telecommunication wavelengths.

The first part of this thesis is dedicated to studying the coaxial metal-dielectric-metal (MDM) waveguide configuration as it applies to coupled negative index waveguide metamaterials and ultra-small mode-volume nanocavities. We begin by presenting transmission measurements done in combination with an analytic and numeric study to experimentally determine the dispersion relation of the positive index coaxial mode, demonstrating how their facet-end reflection coefficients can be tuned to engi-

neer ultra-small mode-volume mode cavities. This study is followed by a theoretical investigation of the negative index modes in MDM coaxial waveguides, along with a study of the effect of geometry and materials on the configuration. We then move on to coupled waveguide geometries, in which we present a new type of metamaterial design, consisting of coupled negative index coaxial waveguides, demonstrating how these photonic material composites can be engineered to operate with refractive indices that are continually tunable from negative to positive values at visible frequencies.

In the second part of this thesis, we explore the optical response of another type of coupled system, consisting of hole arrays, demonstrating, based on a hole-pair scattering model, that the transmission of large-size hole arrays is determined by local (2nd nearest neighbor) rather than long-range order. Furthermore, using this model, we find that the peak transmission efficiency of hole arrays reach $\sim 90\%$ that of an infinite array at $\sim 6 \times 6\ \mu\text{m}^2$ - the smallest size array showing near-infinite array transmission properties. We substantiate these findings with a set of experiments in which we investigate the response of hole arrays in terms of spatial color cross-talk, random defects, and array size. Finally, we demonstrate their performance as efficient color filters by integrating them onto a CMOS image sensor and analyzing the quality of their high-resolution full-color images.

Finally, in the last section of this thesis, we investigate Resonant Guided Wave Networks (RGWNs), another new type of artificial photonic material concept based on the interaction of closed-loop wave resonances in waveguide networks. We describe their building blocks in detail and demonstrate how they can be engineered to form high-Q plasmonic resonators as well as di- and tri-chroic routers operating at telecommunication wavelengths. We demonstrate the concept of RGWNs in a hybrid Si-photonic/plasmonic experimental platform, using NSOM measurements to demonstrate efficiency coupling from SOI ridge waveguides to subwavelength channel plasmon polariton (CPP) networks. We furthermore demonstrate ultracompact 4-way equal power splitters, the basic element of an RGWN, and 2×2 plasmonic resonators operating as a logic device – the first demonstration of a truly subwavelength

integrated plasmonic circuit.

Contents

List of Figures

List of Tables

Chapter 1

Introduction

1.1 Perspective on Metal Optics

The interaction of naturally occurring materials (whether insulating, semiconducting, or metallic) with electromagnetic radiation is characterized by the material's permittivity (ϵ) and permeability (μ) – the two quantities that tell us how *susceptible* the material's electronic composition is to the two driving fields of electromagnetic radiation. For visible frequencies, it turns out that most materials have a very weak magnetic response, which has to do with the strength of their atomic magnetic dipole density, thus making their relative permeabilities very close to that of freespace μ_0. Fortunately, however, the story for permittivity is a lot more interesting. The permittivity of a material relates to the strength of its polarizability, which is appreciable since, electrons, whether bound or free, can be driven to oscillate in response to an electric field. For insulators, the permittivity is determined by the oscillation of bound electrons, and as a result we get dielectrics with relative permittivities > 1. Combining this index platform with Maxwell's equations, we get the field of photonics, which hinges on our ability to confine and manipulate light through the engineering of interesting dielectric index environments such as photonic crystals and fiber optics.

The field of photonics has given rise to such critical technology as fiber optic telecommunication and lasers, but it also suffers from the limitation that it can not be easily miniaturized due to the diffraction limit of light, $\sim \lambda/2n$. Among other driving factors, we find that as the density of transistors keeps increasing and the size

of technology keeps being miniaturized, we find ourselves looking for ways to engineer new smaller photonic technologies in order to keep up with current technology trends. To circumvent this limitation, we find that we can *shrink* light past the diffraction limit if we are willing to trade off loss for confinement by using metals. Loss can in general be considered bad for designing efficient systems, but as long as the system functionality is within the propagation length of the light inside the system, metals in optics could still be beneficial.

Metals, unlike dielectrics, are characterized by negative permittivities that originate from the restoring force their free electrons experience as they scatter off of the metal's lattice in response to a driving electric field. This *sloshing* of electrons transfers some of the field energy to the lattice and, as a result, we get Ohmic loss in the material. However, at optical frequencies, these electrons also form some very useful and tunable charge density oscillations both in the material bulk as well as the surface, and, as a result, we get bulk and *surface plasmon polaritons* [108], with which we can manipulate the properties of light. Similar to the field of photonics, we can confine and manipulate light by designing interesting high-order metal/dielectric systems, such as metal/dielectric/metal (MDM) slab [33] and coaxial waveguides [5], and coupling them to create still higher-order systems such as coupled waveguide networks [135] and hole arrays [55, 40]. However, unlike photonics, plasmonics has the advantage of being able to confine light to sub-wavelength dimensions and enhancing the field as its starting point.

Although plasmonics and photonic crystals both existed in some form before the 1980s, both fields were kicked off at around the same time $\sim$ 30 years ago (at the time of this thesis, 2013), and within that time the number of publications per year of plasmonics have exceeded that of photonic crystals [1]. Part of this increase is due to technological advances that have occurred within that time frame in nano-fabrication, -characterization, and -imaging, as well as advances in computation power and techniques [namely, the finite-difference time-domain (FDTD) method and the finite-element method (FEM)] – allowing us to probe deeper into the field of plasmonics. However, another factor is, of course, the many advantages brought about

by integrating metals into optics. For example, the strong field enhancements in plasmonics allow us to study applications in nano-lasers [9], sensing [16], non-linear behavior [98, 20, 24], ultra-fast electron processes [77], and photovoltaics [4], to name a few. Other applications include using the Ohmic loss induced by plasmonics for useful heating applications, as in heat assisted magnetic recording (HAMR) [100]. And still, there are applications that are just beginning to arise, such as the use of acoustics [106], magnetic field [26], and superconductivity [41] to modulate the plasmon response. At the time of this thesis, quantum- and graphene-plasmonics were at the forefront of the field, making us reflect how far the field has come in only ∼30 years, and wonder where it will be in the next 10.

1.2 Scope of this Thesis

This thesis is divided into three parts, describing the theory and application of plasmonics as it pertains to I) coaxial plasmonic waveguides and metamaterials, II) hole array color filters and CMOS image sensing, and III) resonant guided wave networks and hybrid plasmo-photonic circuitry.

1.2.1 Coaxial Plasmonic Waveguides and Metamaterials

As mentioned in §1.1, naturally occurring materials are characterized either by decaying negative refractive indices (metals) or by propagating positive indices (dielectrics) – plasmonics allows us to bridge the gap between these two regimes through the use of propagating negative index modes, which brings us into another recently developed field in optics called *metamaterials* [122] (∼14 years old at the time of this thesis, 2013). Within this field, artificial photonic materials are designed to have almost arbitrarily selected effective refractive indices via the design of their constituent *meta-atoms*. Metamaterials started off at microwave frequencies in the late 1990s where mm-size split-ring resonators were printed on circuit boards to generate the desired diamagnetic response that gives rise to negative index. Since then, aided by advances in nano-fabrication, researchers incrementally miniaturized the size of the

resonant meta-atoms to bring their operation into the telecommunication and visible part of the electromagnetic spectrum, where they could be used for imaging [46] and communication applications [91]. However, due to the small scattering cross-section of these constituent meta-atoms as they are miniaturized, the operation of resonant-based metamaterials saturates at near-infrared frequencies, making it difficult to bring down their operation into the visible [75].

Plasmonics, via the metal/dielectric/metal (MDM) waveguide configuration, is able to access H-field anti-symmetric negative index modes near the surface plasmon resonance of the metal/dielectric material combination [33]. As discussed in §1.1, this resonance can be tuned into the visible by setting the dielectric permittivity to some high value. As a result, we can bring the negative index waveguide mode out of the ultraviolet into the visible – working from the opposite direction than conventional metamaterials. However, due to the transverse-magnetic nature of SPs, the planar MDM configuration is polarization and angle-of-incidence sensitive [34], but this limitation can be circumvented by wrapping the planar MDM geometry to form coaxial MDM waveguides, which support similar types of modes [30].

Because the negative index mode exists near the SP resonance, the mode is characterized by high loss, i.e.,unlike the H-field symmetric positive index mode, its modal volume is heavily delocalized into the cladding metal layer [29]. As such, in making an array of negative index coaxial waveguides, they can easily couple to each other through the connecting metal layer, forming a type of metallic photonic crystal in the in-plane direction [131]. What we find is that the in-plane Bloch mode created by the coupled propagating negative index axial mode can be tuned to have the same negative index behavior as that of an isolated negative index waveguide mode. Through this method, we are able to design a negative index plasmonic metamaterial that operates at visible frequencies, all with a single thin layer of coupled negative index coaxial waveguides [17].

The basis for coaxial MIM waveguides is discussed in Chapter 3, consisting of transmission measurements done in combination with an analytic and numeric study to experimentally determine the dispersion relation of their positive (H-field symmet-

ric) index modes. This study is followed by a theoretical investigation in Chapter 4, in which we study the nature of the negative index modes in MDM coaxial waveguides, along with a study of the effect of geometry and materials on the configuration. Having studied single waveguide geometries, we move to coupled waveguide geometries in Chapter 5, in which we present the negative index metamaterial design consisting of coupled negative index waveguides.

1.2.2 Hole Array Color Filters and Plasmonic CMOS Image Sensing

Outside of metamaterials, plasmonics also has tremendous potential in imaging applications. In contemporary Si-based image sensor technologies such as charge-couple devices (CCDs) and complementary metal-oxide semiconductor (CMOS) image sensors, color sensitivity is added to photo detective pixels by equipping them with on-chip color filters, composed of organic dye-based absorption filters [88]. However, organic dye filters are not durable at high temperatures or under long exposure to ultraviolet (UV) radiation [61] and cannot be made much thinner than a few hundred nanometers due to the low absorption coefficient of the dye material. Furthermore, on-chip color filter implementation using organic dye filters requires carefully aligned lithography steps for each type of color filter over the entire photodiode array, thus making their fabrication costly and highly impractical for multi-color and hyperspectral imaging devices composed of more than the three primary or complementary colors.

It is well known that plasmonic hole arrays in thin metal films can be engineered as optical band-pass filters, owing to the interference of surface plasmons (SPs) between adjacent holes. Unlike current on-chip organic color filters, plasmonic filters have the advantage of being highly tunable across the visible spectrum and require only a single perforated metal layer to fabricate many colors. Plasmonic hole array color filters have recently been integrated with a CMOS image sensor [21, 23], demonstrating filter viability in the visible, but full color imaging using the plasmonic color filter

technology platform still remains to be reported. Furthermore, hole array research has mostly been focused on the transmission properties of large size filters, with little emphasis given to other important filter performance aspects necessary for state-of-the art image sensor applications, such as the filter transmission dependence on array size, spatial color-crosstalk, and robustness against defects.

In Chapter 6, we report on such optical properties as they pertain to various configurations of hexagonal arrays of subwavelength holes fabricated in 150-nm-thick Al films suitable for image sensor integration. In Chapter 7, we investigate the transmission and imaging characteristics of a 360 × 320 pixel plasmonic color filter array composed on 5.6×5.6 μm^2 size RGB color filters integrated onto a commercial black and white 1/2.8 inch CMOS image sensor, the first demonstration of high resolution full color plasmonic imaging. And, finally, in Chapter 8 we demonstrate that the transmission spectra of hole array filters can be accurately described by the 2$^{\text{nd}}$ nearest neighbor scattering-absorption interactions of hole pairs – thus making hole arrays appealing for close packed hole array filters for imaging applications.

1.2.3 Resonant Guided Wave Networks and Hybrid Plasmo-Photonic Circuitry

As mentioned in §1.1, one of the most compelling aspects of plasmonics is the ability to confine electromagnetic radiation in subwavelength modes at metal/dielectric interfaces – a promising characteristic for miniaturizing photonic communications technology at the scale and density of electronics. However, in order to simultaneously achieve low waveguide propagation loss and high mode confinement, we require chip-based hybrid photonic/plasmonic circuits that feature (1) low-loss silicon photonic waveguides, (2) high-confinement plasmonic waveguide building blocks, and (3) methods for efficient mode coupling between them. The channel plasmon polariton (CPP) configuration supports and confines slot plasmon polaritons in a highly confined channel (similar to the H-field symmetric MDM plasmonic mode) [13].

Incidentally, these same CPP channels can also serve as plasmonic building blocks

for another type of artificial material design called *resonant guided wave networks* (RGWNs) [48] consisting of isolated plasmonic waveguides in a network configuration. RGWNs, through the use of waveguides to accumulate phase and waveguide crossings to split power, can serve as artificial materials for engineering dispersion through the interaction of closed-loop wave resonances that arise throughout the waveguide network as a result of the isolated waveguides that couple only through their intersections.

In Chapter 9 we give a theoretical premise for RGWNs, describing their building blocks and demonstrating how they can be engineered to form high-Q plasmonic resonators. We then move on to describe a more comprehensive example of how the RGWN resonances can be engineered in anisotropic layout to function as di- and tri-chroic routers operating at telecommunication wavelengths. In Chapter 10 we provide an experimental realization of a plasmonic RGWN coupled to Si photonics, demonstrating that light can be efficiently coupled from silicon-on-insulator ridge waveguides to channel plasmon polariton waveguides. By proper control of mode polarization in the silicon-on-insulator waveguide, we demonstrate that parasitic excitation of surface plasmon polaritons (SPPs) on the metal surface is suppressed, only exciting the desired CPP mode of the RGWN structure. We substantiate these findings with near-field scanning optical measurements (NSOM) to demonstrate efficient coupling into the channel plasmon polariton mode from Si ridge waveguides at $\lambda_0 = 1520$ nm with light incoupled via grating couplers. Using NSOM, we also demonstrate an ultracompact 4-way equal power splitter, the fundamental element for ultracompact resonators and plasmonic circuits. We highlight their functionality by fabricating and measuring a 2×2 plasmonic resonator operating as logic device, similar to that described in Chapter 9.

Chapter 2

Introduction to Metal Optics

2.1 Optical Properties of Metals

As mentioned in §1.1, the optical response of metals is characterized by their complex permittivitity, which, in general, depends on frequency, due to the different types of processes that occur within the material at different parts of the electromagnetic spectrum. For example, at near-infrared frequencies, a metal's permittivity is determined by its free electron response to a driving electric field (an intraband process), while at visible frequencies, there is an additional contribution that comes from the interband promotion of electrons to higher energy bands. The free electron dynamics can be accurately described by the Drude model, whereas the interband transitions can be described by the Lorentz (damped oscillator) model.

In the Drude model, electrons are considered as charged (but non-interacting) particles, each with effective mass m_e and charge q, which can be accelerated in the presence of a driving electric field, and decelerated as they scatter off of the metal's atomic lattice. Classically considering the free electrons to be at rest in the absence of an external force, they undergo a displacement $\mathbf{r}$ from their rest positions, creating a density of dipole moments $\mathbf{p} = q\mathbf{r}$ within the material. These dipole moments manifest themselves as a macroscopic *polarization* per unit volume of the material $\mathbf{P} = n\mathbf{p}$, where n is the number of electrons per unit volume.

As mentioned in section §1.1, the polarization $\mathbf{P}$ of a material relates to how the charges respond to an incident driving electric field. These two quantities are

proportional to each other, connected via the electric susceptibility of the material, χ_e, whose value depends on its electronic response to the incident electric field (Eq. 2.1).

$$\mathbf{P} = \epsilon_0 \chi_e \mathbf{E} \tag{2.1}$$

Now, in the absence of the material, light would simply propagate according to the permittivity of freespace, $\epsilon_0\mathbf{E}$, so in the precense of a material, we are adding a term to this expression (see Eq. 2.2). We designate this quantity the name *electric displacement vector*, $\mathbf{D}$.

$$\begin{aligned} \mathbf{D} &= \epsilon_0\mathbf{E} + \mathbf{P} \\ &= \epsilon_0\mathbf{E} + \epsilon_0\chi_e\mathbf{E} \\ &= \epsilon_0(1+\chi_e)\mathbf{E} \\ &= \epsilon\mathbf{E} \end{aligned} \tag{2.2}$$

From Eqs. 2.1 and 2.2 and we get that the permittivity of a material is defined according to Eq. 2.3.

$$\begin{aligned} \epsilon &= \epsilon_0(1+\chi_e)\mathbf{E} \\ &= \epsilon_0\left(1+\frac{\mathbf{P}}{\mathbf{E}}\right) \end{aligned} \tag{2.3}$$

Since the polarization $\mathbf{P}$ of a material is related to the dipole moments $\mathbf{p}$ within the material, all that remains to be known is the average displacement vector of its electrons, $\mathbf{r}$. We do this by applying the equations of motion to the free electron gas as they are accelerated by the driving field and are decelerated by collisions with the atomic lattice.

2.2 The Drude Model

Starting with electrons at rest, an applied electric field $\mathbf{E}$ with an $e^{i\omega t}$ temporal dependence will have the effect of applying a accelerating force of $\mathbf{F_E} = q\mathbf{E}e^{i\omega t}$ to the electrons. The electrons are accelerated until they encounter a scattering lattice site, causing them to decelerate. This damping term is similar to that of a drag force in that it opposes the initial direction of the electron's momentum, with a magnitude that is inversely proportional to the average collision time, $\Gamma = 1/\tau$. Putting it all together, we get Eq. 2.4.

$$m_e \frac{\partial^2 \mathbf{r}}{\partial^2 t} - m_e \Gamma \frac{\partial \mathbf{r}}{\partial t} = q\mathbf{E}e^{i\omega t} \tag{2.4}$$

Assuming an $e^{i\omega t}$ response of the displacement vector, which is sensible since the electrons are being driven at this frequency, we get that the material polarization is given by Eq. 2.5.

$$\begin{aligned} \mathbf{P} &= q\mathbf{r} \\ &= \frac{-q^2/m}{\omega^2 + i\Gamma\omega}\mathbf{E} \end{aligned} \tag{2.5}$$

Combining this result with Eq. 2.3, we arrive at the expression for the frequency dependent permittivity function of a metal (Eq. 2.6), where $\omega_p = \sqrt{q^2 n/m_e \epsilon_0}$ is the characteristic bulk plasma frequency of the metal.

$$\begin{aligned} \epsilon_r(\omega) &= \epsilon(\omega)/\epsilon_0 \\ &= 1 - \frac{\omega_p^2}{\omega^2 + i\Gamma\omega} \end{aligned} \tag{2.6}$$

The plasma ω_p and damping Γ frequency values can be obtained by fitting Eq. 2.6 to empirical permittivity measurements, obtained, for example, by ellipsometry. Values obtained by fitting to Palik data are shown in Table 2.1. Using the conversion 1 eV = 1240 nm, we see that the plasma frequency for these metals is in the ultraviolet, at around $\lambda_0 = 200$ nm. The permittivity data along with the fitted curves are shown in Fig. 2.1. A couple of things stand out from Fig. 2.1 and Eq. 2.6 that are worth

Metal	ω_p (eV)	Γ (meV)	ω_{ib} (eV)
Silver (Ag)	7.65	75.9	4.13
Gold (Au)	7.96	90.3	2.48
Copper (Cu)	12.94	177.8	1.55
Aluminum (Al)	6.78	127.0	2.25

Table 2.1: Plasma ω_p, damping Γ, and interband ω_{ib} frequency values of some metals used in plasmonics. The plasma and damping values are obtained by fitting to the Drude model, and the interband frequency values are obtained by fitting to a Drude-Lorentz model.

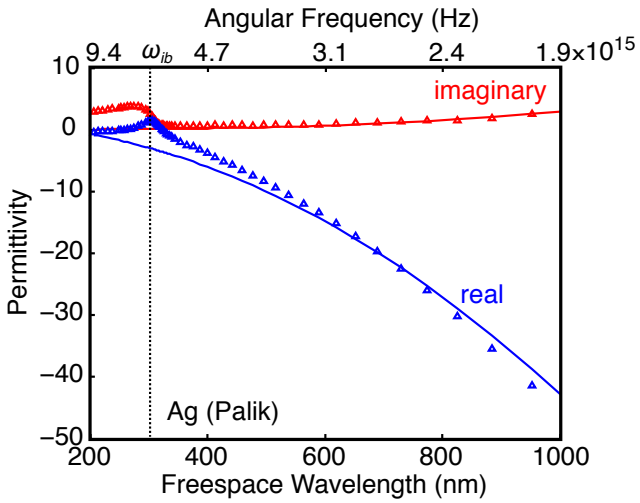

Figure 2.1: Real and Imaginary parts of the permittivity data for Ag at visible frequencies. Solid line plots are obtained by fitting the Drude model to tabulated Palik data.

mentioning. In the high frequency regime, $\omega >> \Gamma$, the Drude permittivity can be further approximated as the purely real quantity shown in Eq. 2.7.

$$\epsilon_r(\omega) = 1 - \frac{\omega_p^2}{\omega^2} \tag{2.7}$$

In looking at Eq. 2.7 together with Fig. 2.1, we see that the real part of the permittivity crosses from being negative ($\omega < \omega_p$) to positive ($\omega > \omega_p$) at the plasma frequency ω_p. Thus, given a metallic permittivity function, one only needs to see where the real part of the permittivity crosses zero to approximate the plasma frequency of the material. Similarly, a negative permittivity corresponds to exponentially decaying

solutions, i.e., imaginary wave vectors, whereas a positive permittivity corresponds to real valued propagating wave vectors. Thus, in this high frequency limit, we see that light will propagate inside the metal for frequency values larger than ω_p and decay exponentially for frequency values smaller than ω_p. Physically, this has to do with the ability of the bulk electron plasma to oscillate at the driving frequency of light for low values of frequency ($\omega < \omega_p$), but unable to keep up at higher frequencies ($\omega > \omega_p$).

Furthermore, we see from Fig. 2.1 that the Drude model is good at predicting the premittivity of metals at near infrared wavelengths, but fails to capture the interband transitions, which happen at different parts of the visible spectrum for different metals (see Table 2.1). These can be modeled classically as damped harmonic oscillators via a Drude-Lorentz model, but will not be discussed further here for brevity.

2.3 Maxwell's Equations

In order to understand how light will propagate in the presence of a metal, we need to examine how light propagates in a material with a general complex permittivity $\tilde{\epsilon}(\omega)$. As with every electromagnetic problem, we begin by writing down the set of four electromagnetic equations, which are individually named after the famous physicists that empirically discovered their form, but collectively take the name of Maxwell, since it was he who unified them via the addition of the displacement current term $\mathbf{D}$. Maxwell's equations are summarized in Eq. 2.8.

$$\nabla \times \mathbf{E} = -\frac{\partial \mathbf{B}}{\partial t} \tag{2.8a}$$

$$\nabla \times \mathbf{H} = \mathbf{J} + \frac{\partial \mathbf{D}}{\partial t} \tag{2.8b}$$

$$\nabla \cdot \mathbf{D} = \rho \tag{2.8c}$$

$$\nabla \cdot \mathbf{B} = 0 \tag{2.8d}$$

We can connect these equations by taking the curl of Eq. 2.8a and relating it to Eq. 2.8b via the vector identity $\nabla(\nabla \times \mathbf{A}) = \nabla(\nabla \cdot \mathbf{A}) - \nabla^2\mathbf{A}$ and Eq. 2.8c. Note how this connection would not be possible without Maxwell's displacement current term. Then, using the relations $\mathbf{D} = \epsilon\mathbf{E}$, $\mathbf{B} = \mu\mathbf{H}$, and $\mathbf{J} = \sigma\mathbf{E}$, we arrive at the general form of the wave equation (Eq. 2.9).

$$\nabla^2\mathbf{E} = \mu\sigma\frac{\partial\mathbf{E}}{\partial t} - \nabla(\nabla \cdot \mathbf{E}) + \epsilon\mu\frac{\partial^2\mathbf{E}}{\partial t^2} \tag{2.9}$$

In the absence of sources, $\sigma = 0$ and $\nabla \cdot \mathbf{E} = 0$, and assuming a harmonic response of the form $e^{i(\mathbf{k}\cdot\mathbf{r}-\omega t)}$, we arrive at the expression known as the dispersion of light in freespace, $\mathbf{k}^2 = \epsilon\mu\omega^2$. This expression gives us the propagation wave vector $|\mathbf{k}| = 2\pi/\lambda$ of light, given its frequency and the material in which it propagates, characterized by (ϵ, μ). Since $c = 1/\sqrt{\epsilon\mu}$, we get that the propagation wave vector is proportional to the frequency of the light and inversely proportional to its phase velocity.

2.4 Surface Plasmons

In order to understand how electron oscillations couple to light at a metal/dielectric interface, we need to think about what solutions are admissible by the problem. Assuming a system with permittivity ϵ_1 for $y > 0$ and permittivity ϵ_2 for $y < 0$ (see Fig. 2.2), we look for solutions that are bound at and propagating along the material interface. More specifically, we want oscillatory solutions along the z-direction (could have equally chosen the x-axis) and exponentially decaying solutions along the y-direction. Mathematically, this means we are looking for solutions of the form shown in Eq. 2.10, where the number subscripts refer to which permittivity medium (1 or 2) the equation applies. Note that I have conveniently selected the TM form of the solution in anticipation of surface plasmons.

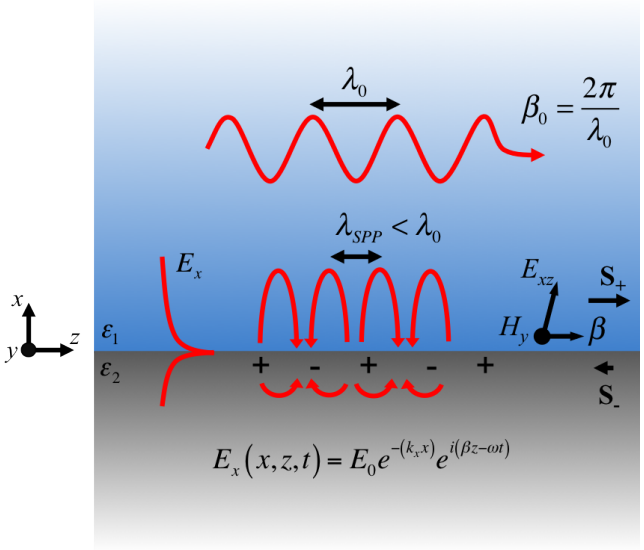

Figure 2.2: Surface plasmon geometry composed of permittivity ϵ_1 for $y > 0$ and permittivity ϵ_2 for $y < 0$. The corresponding propagating wave vector and associated field vectors are displayed by black arrows inside the material, along with a schematic of the resulting field intensity, shown in red. The '+' signs represent a charge depletion area, which is periodic along the propagation wave vector direction of the surface plasmon.

$$\mathbf{E}_{(1,2)} = \begin{pmatrix} 0 \\ E_{y(1,2)} \\ E_{z(1,2)} \end{pmatrix} e^{i(k_z z - \omega t)} e^{i k_{y(1,2)} y} \tag{2.10}$$

But in order for Eq. 2.10 to be a solution we must (1) impose restrictions on the decomposed wave vectors based on the total wave vector as it applies to each material, (2) make sure that it satisfies the wave equation (Eq. 2.9), and (3) apply the appropriate boundary conditions at the material interface so that our solution is consistent with Maxwell's equations.

(1) To restrict the wave vectors, we simply note that in the absence of an interface, light would simply propagate with wave vector $k^2_{(1,2)} = \epsilon_{(1,2)} k_0^2$ in each medium. Thus, in decomposing the field, as done in Eq. 2.10, we need to make sure that in each medium, the magnitude of the decomposed wave vectors equals magnitude of the

medium wave vector (Eq. 2.11).

$$\epsilon_{(1,2)} k_0^2 = k_{y(1,2)}^2 + k_z^2 \tag{2.11}$$

(2) To impose that Eq. 2.10 satisfies the wave equation (Eq. 2.9), we impose the condition that $\nabla \cdot \mathbf{E} = 0$, since there are no static sources generating electric field. (Note that in this case $\sigma \neq 0$, since we *do* have a material conductivity that arises from the oscillating free electrons.) Applying this restriction to Eq. 2.10, we obtain a relation between the amplitude of the fields in each medium (see Eq. 2.12).

$$k_{y(1,2)} E_y + k_z E_{z(1,2)} = 0 \tag{2.12}$$

(3) Lastly, we apply the boundary conditions for an electric field at an interface with no static sources, $E_{(1)\parallel} = E_{(2)\parallel}$ and $\epsilon_1 \mathbf{E}_{(1)\perp} = \epsilon_1 \mathbf{E}_{(2)\perp}$, which yields the set of equations shown in Eq. 2.13.

$$\begin{aligned} E_{z(1)} &= E_{z(2)} \\ \epsilon_1 E_{y(1)} &= \epsilon_2 E_{y(2)} \end{aligned} \tag{2.13}$$

Equations 2.12 and 2.13 form a homogeneous set of equations (Eq. 2.14a), whose solution is determined by finding the nontrivial solution to $\det[\mathbf{M}] = 0$ (Eq. 2.14b), which yields the relation $\epsilon_1 k_{y(2)} = \epsilon_2 k_{y(1)}$ (Eq. 2.14c).

$$\mathbf{M} = \begin{pmatrix} k_{y(1)} & k_z & 0 & 0 \\ 0 & 0 & k_{y(2)} & k_z \\ 0 & 1 & 0 & -1 \\ \epsilon_1 & 0 & -\epsilon_2 & 0 \end{pmatrix} \tag{2.14a}$$

$$\det[\mathbf{M}] = 0 \tag{2.14b}$$

$$\epsilon_1 k_{y(2)} = \epsilon_2 k_{y(1)} \tag{2.14c}$$

Equation 2.14c allows us to combine the two (up to now independent) dispersion

relations of Eq. 2.11 to obtain the combined dispersion relation for the surface wave supported at the interface between the two materials (Eq. 2.15).

$$k_z = \sqrt{\frac{\epsilon_1 \epsilon_2}{\epsilon_1 + \epsilon_2}} k_0 \tag{2.15a}$$

$$k_{y(1,2)} = \frac{\epsilon_{1,2}}{\sqrt{\epsilon_1 + \epsilon_2}} k_0 \tag{2.15b}$$

Requiring exponentially decaying solutions away from the interface translates into having imaginary $k_{y(1,2)}$ wave vectors, which, in looking at Eq. 2.15b, is only possible if the sum $(\epsilon_1 + \epsilon_2) < 0$. Similarly, requiring that we get propagating solutions parallel to the material interface means that we need to have real k_z wave vectors. Combining the form Eq. 2.15a with the restriction imposed by Eq. 2.15b indicates that real propagating wave vectors will exist when the additional condition $(\epsilon_1 \epsilon_2 < 0)$ is satisfied. Thus, we get that in order to have solutions with these desired properties, we require one of the permittivities to be negative, thus requiring one of the materials to be metallic.

To illustrate some of the properties of these surface waves, some properties of the dispersion relation (Eq. 2.15) are plotted for the case where $\epsilon_1 = \epsilon_{\mathrm{Si}}$ and $\epsilon_2 = \epsilon_{\mathrm{Ag}}$ (Fig. 2.3). Panel (a) plots the real part of the Ag/Si plasmon propagation wave vector $\Re[k_z]$ (red), together with that of bulk Si (green), bulk Ag (blue), and air (black). Panel (b) plots the propagation length, $L_z = 1/2\Im[k_z]$, defined as the propagation distance at which the field intensity reaches a fractional value of $1/e$. This quantity is plotted for the Ag/Si surface plasmon (red), bulk Si (green), and bulk Ag (blue). Panel (c) plots the surface plasmon penetration depth, $L_{y(1,2)} = 1/2\Im\left[k_{y(1,2)}\right]$, into both the Si (green) and Ag (blue) – similarly defined as perpendicular distance away from the interface at which the field intensity reaches a fractional value of $1/e$ from its value right at the interface.

Starting at low frequencies (long freespace wavelengths), we see from Fig. 2.3a, that the surface plasmon propagation wave vector (green) equals that of Si (red), i.e., light behaves as if there is no metal present in the system. The only way this could happen is if the light had a negligible penetration depth into metal. Indeed, we see

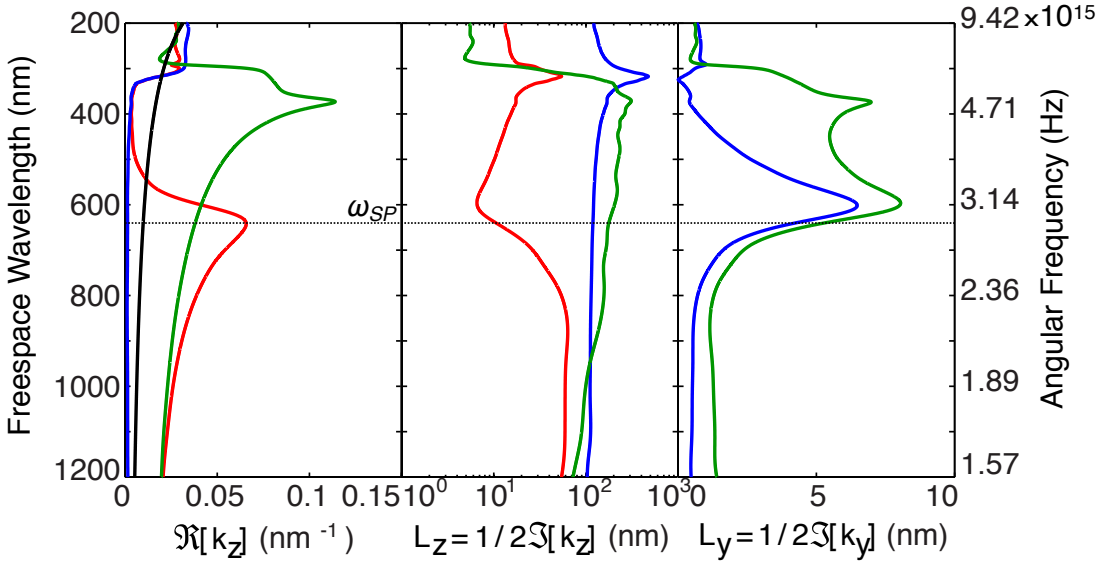

Figure 2.3: Dispersion relation properties (Eq. 2.15) for the case where $\epsilon_1 = \epsilon_{\mathrm{Si}}$ and $\epsilon_2 = \epsilon_{\mathrm{Ag}}$. Panel (a) plots the real part of the Ag/Si plasmon propagation wave vector $\Re[k_z]$ (red), together with that of bulk Si (green), bulk Ag (blue), and air (black). Panel (b) plots the propagation length, $L_z = 1/2\Im[k_z]$, defined as the propagation distance at which the field intensity reaches a fractional value of $1/e$. This quantity is plotted for the Ag/Si surface plasmon (red), bulk Si (green), and bulk Ag (blue). Panel (c) plots the surface plasmon penetration depth, $L_{y(1,2)} = 1/2\Im\left[k_{y(1,2)}\right]$, into both the Si (green) and Ag (blue), similarly defined as perpendicular distance away from the interface at which the field intensity reaches a fractional value of $1/e$ from its value right at the interface.

from Fig. 2.3c, that the surface plasmon mode is almost completely expelled from the metal, having most of its modal overlap with the Si. This has to do with the fact that the Ag permittivity is large and negative (see Fig. 2.1), as the surface electrons in the metal are able to keep up with the low driving frequency of the light, thus expelling its penetration. For these frequencies, we thus get a surface plasmon mode that resembles a mode just propagating in the Si. Indeed, we see from Fig. 2.3b that for long wavelengths, we get a surface plasmon propagation length (red) that approaches that of bulk Si (green). In this regime, the surface plasmon mode is characterized as having a weak field confinement, which leads to it having little dispersion and long propagation lengths (limited only by the absorption in Si in this example).

However, as the frequency of light is increased to visible frequencies (going towards shorter wavelengths), we see from Fig. 2.3c that the penetration depth into the metal increases, which has to do with the fact that the real part of the Ag permittivity is becoming less negative (see Fig. 2.1) as the surface electrons in the metal start becoming less efficient at keeping up with the increasing driving frequency of the light. As a result, light begins to slow down as it couples with the plasma oscillations of the metal at its surface. This is reflected by the fact that the surface plasmon propagation wave vector deviates away from the Si light line towards higher values. This means that the mode effective wavelength is shortened, giving rise to dispersion. But, as mentioned in §1.1, this interaction of light with the metal's free electrons comes at the cost of Ohmic losses in the metal, as reflected in Fig. 2.3b, where we see that the surface plasmon propagation length decreases as the penetration depth and dispersion increase.

This trend continues until we reach the frequency point where the permittivities satisfy the relation $(\epsilon_1 + \epsilon_2) \sim 0$ (see Eq. 2.15b), a frequency known as the surface plasmon resonance of the system. (I say approximate because in this case both the Ag and Si permittivities are complex, making it impossible to get both real and imaginary parts to cancel at the same frequency point. But to good approximation, this frequency point can be found by satisfying the relation with the real parts of the permittivities). At this point, the electrons are in resonance with the driving

frequency of light, forming a coupled photo-electron system. This point is reflected in Fig. 2.3a as the highest wave vector point in the dispersion. But again, this comes at the cost of Ohmic loss in the system as is evident in the low propagation lengths which arise from the high penetration depth into the metal.

As the frequency of light is increased further toward shorter freespace wavelengths, larger in frequency than the surface plasmon resonance but lower than the bulk plasmon resonance, we pass a transition regime in which we go from a surface plasmon mode into a bulk plasmon mode, which is characterized by a forbidden band in the dispersion described by small wave vectors (smaller than that of Si) and high loss (Fig. 2.3b). In this regime, as the frequency is increased, the surface electrons are increasingly inefficient at oscillating at the driving frequency of the light, leading to us lose the confinement of the SP mode. Meanwhile, the bulk electrons also lose their ability to oscillate at the frequency of the driving electric field, causing them to be less efficient at screening its penetration. Finally, as we increase the frequency past the plasmon resonance of the material, the bulk electrons are completely unable to keep up with the driving frequency of light, and we get propagation modes inside of the metal as discussed in §2.2. This is evident from Fig. 2.3a, where we see the propagation wave vector increase again past the light line.

Part I

Coaxial Plasmonic Waveguides and Metamaterials

Chapter 3

Plasmon Dispersion in Coaxial Waveguides from Single-Cavity Optical Transmission Measurements

Abstract: *This chapter introduces plasmonic coaxial waveguides, describing how we experimentally determine their dispersion relation via optical transmission measurements performed on isolated coaxial nanoapertures fabricated on a Ag film using focused ion-beam lithography. The dispersion depends strongly on the dielectric material and layer thickness. Our experimental results agree well with an analytical model for plasmon dispersion in coaxial waveguides. We observe large phase shifts at reflection from the end facets of the coaxial cavity, which strongly affect the waveguide resonances and can be tuned by changing the coax geometry, composition, and surrounding dielectric index, enabling coaxial cavities with ultrasmall mode volumes.*

3.1 Introduction

In only a few years' time the rapidly growing field of plasmonics has generated a large array of new nanophotonic concepts and applications. The ability of metal nanostructures to localize light to subwavelength volumes [86, 32, 132] has provided opportunities for sensing applications[89] and nanoscale optical lithography [65, 60]. Plasmonics also provides a way to finely tailor the dispersion relation of light, giving

the ability to shrink the wavelength of light down to only a few tens of nanometers at optical frequencies,[83] or create materials with negative index of refraction [103]. Possible applications where precise control of the optical dispersion is essential range from true-nanoscale optical components for integration on semiconductor chips to lenses for subwavelength imaging [103, 45] and invisibility cloak [105, 2].

Recently, coaxial plasmon waveguides with a circular dielectric channel separating a metallic core and cladding have received a great deal of attention in connection to observed enhanced transmission from two-dimensional arrays of coaxial nanoapertures at infrared wavelengths [44, 111, 94]. The transmission enhancements have been ascribed to standing optical waves along the axis of the coaxial apertures [5, 58, 59]. Past studies have been limited to short (<200 nm) coaxial channels, allowing observation only of the lowest order resonances [44, 111, 94]. Furthermore, optical transmission has only been measured for arrays of coaxial waveguides, making it hard to separate transmission enhancements owing to channel resonances from enhancements related to collective resonances of the array [44, 111, 94, 130]. To investigate the optical resonances of coaxial waveguides in detail, measurements on single coaxial nanostructures are necessary. Furthermore, a systematic study is needed of the phase shifts upon reflection from the waveguide ends, as they strongly affect the resonances of a short waveguide.

Here, we report optical transmission measurements of isolated coaxial plasmon waveguides in Ag with systematically varied lengths in the range 265 – 485 nm. By variation of the channel length, the dispersion relation for these structures was determined for the first time. The experimental results agree well with an analytical model for plasmon dispersion in coaxial waveguides. We observe a significant enhancement of the wave vector of light when coupled to coaxial waveguides from freespace, even at frequencies well below the surface plasmon resonance. It is found that the phase shift upon reflection off the waveguide ends can be tuned by changing the waveguide geometry. We anticipate that the combination of strong optical confinement and relatively low propagation loss make coaxial waveguides very promising as nanoscale optical components.

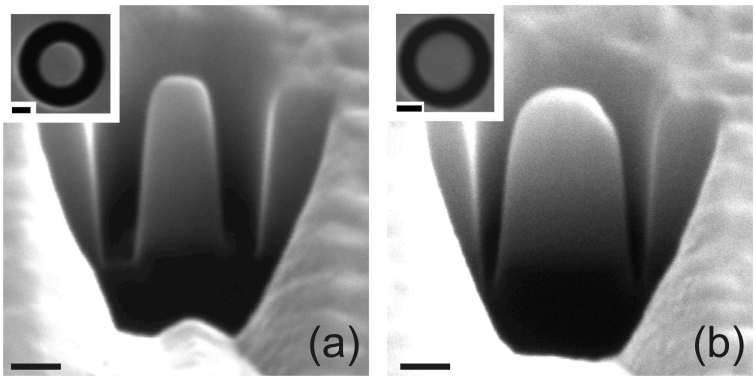

Figure 3.1: SEM images of the cross-sectional profile of coaxial plasmon waveguides with lengths of 485 nm, dielectric channel widths of ∼100 nm (a) and ∼50 nm (b), and outer radii of ∼175 nm. The insets show top-view SEM images of the waveguides before cross sectioning. Scale bars are 100 nm.

3.2 Measuring the Dispersion of a Coaxial Plasmonic Waveguide

The plasmon dispersion in coaxial waveguides was determined from transmission measurements of isolated coaxial channels prepared using focused ion beam (FIB) milling on films of Ag. Ag was deposited by thermal evaporation on quartz substrates. The Ag thickness was varied between 265 and 485 nm in 20 nm increments, using a shutter. We fabricated coaxial waveguides by FIB milling 20–100-nm-wide circular channels through the Ag layer. Figure 3.1 shows scanning electron microscope (SEM) images of 485-nm-long coaxial channels with an outer radius of ∼175 nm and channel widths of ∼100 nm (a) and ∼50 nm (b). The main panels in Fig. 3.1 were taken at a 55° angle with respect to the sample normal, after a cross section was made using FIB milling. The images display a small degree of tapering of the channels (∼7° taper angle), which is mainly caused by redeposition of Ag in the waveguide during FIB milling, an effect that becomes more pronounced deeper in the Ag layer. The insets in Fig. 3.1 are top-view SEM images of the coaxial channels that show excellent uniformity of the channel radii and width. Coaxial channels were separated by 50 μm to avoid coupling between waveguides.

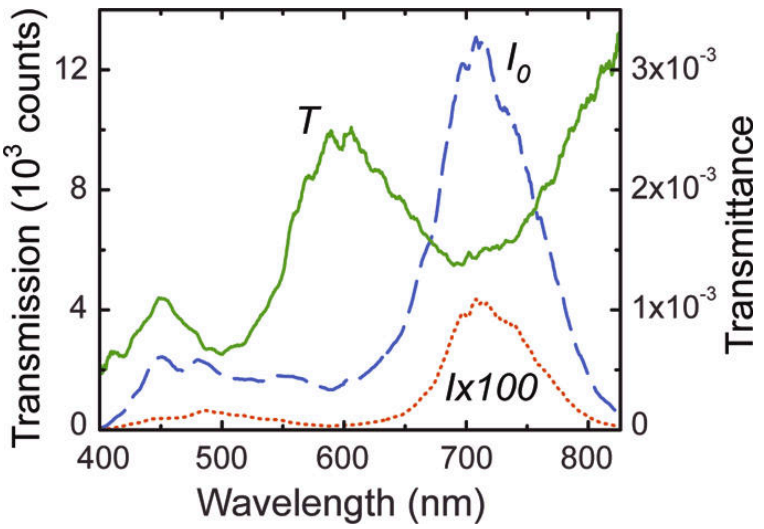

Figure 3.2: Transmission measurement (red dotted spectrum, I multiplied by 100) of a 485-nm-long coaxial waveguide with a ∼100-nm-wide dielectric channel (see Fig. 3.1b) and a reference spectrum (blue dashed line, I_0). The transmittance defined as the waveguide transmission spectrum divided by the reference spectrum is depicted by the green curve (green drawn line, T).

To investigate the influence of channel length and width on the optical response of coaxial waveguides, we performed optical transmission measurements. Radiation from a supercontinuum white light source was focused onto individual coax structures using a 0.95 NA objective. The transmitted light was collected by a 0.7 NA objective and directed into a spectrometer equipped with a CCD detector to measure optical spectra. For reference, we measured transmission spectra of 10 × 10 μm open squares, in which the Ag layer had been completely removed by FIB milling. Figure 3.2 shows transmission spectra of a 100-nm-wide, 485-nm-long coax channel (I) and of a reference area close to the waveguide (I_0). The transmittance spectrum ($T = I/I_0$) is obtained by normalizing the waveguide transmission to the reference spectrum and is also shown in the figure. Three distinct maxima can be resolved in the transmittance spectrum, at ∼450, ∼600, and >820 nm, which we attribute to Fabry-Perot cavity resonances of the coaxial waveguide. To corroborate this hypothesis, we have measured the transmittance of a series of coaxial waveguides of equal channel width but varying channel lengths.

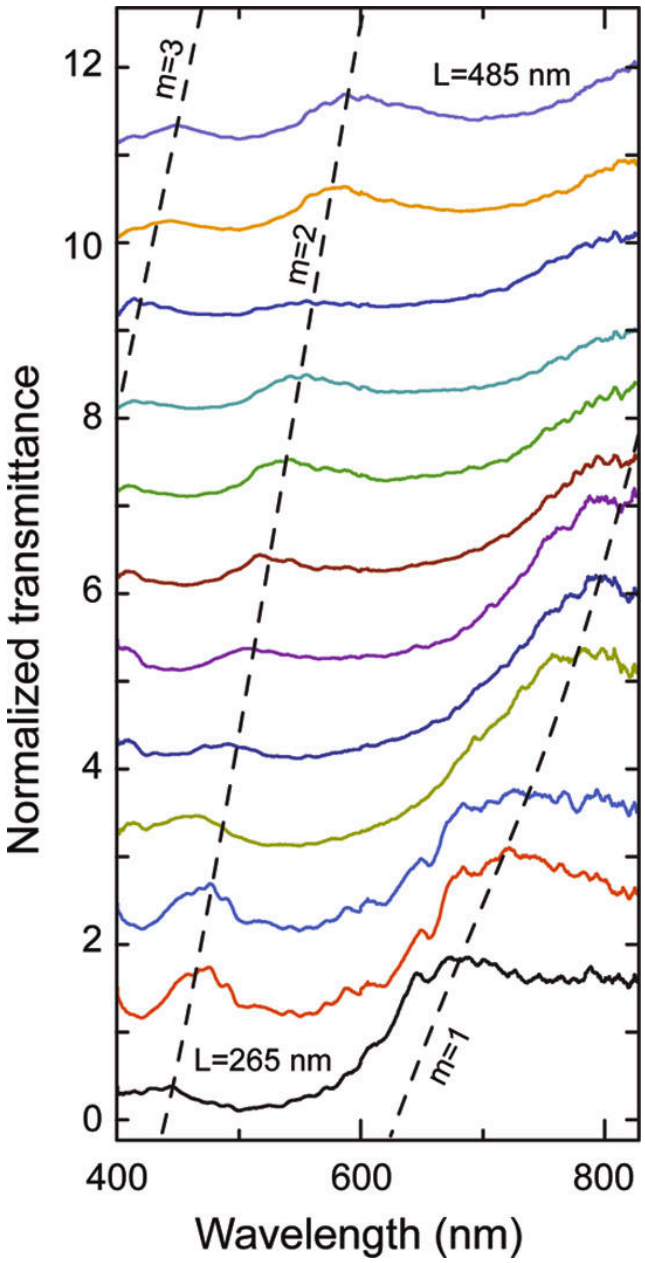

Figure 3.3: Transmittance spectra of coaxial waveguides with varying lengths. The outer radius and channel width were ∼175 and ∼100 nm, respectively, while the waveguide length was decreased from 485 nm (top curve) to 265 nm (bottom curve) in increments of 20 nm. Data are shifted vertically for clarity. The black dashed lines are guides for the eye and connect the resonance peaks $m = 1 - 3$).

Figure 3.3 shows transmittance spectra of 100-nm-wide coaxial channels with length decreasing from 485 nm (same data as in Fig. 3.2) to 265 nm in 20-nm increments. Several features are observed. First, the resonance at 600 nm for the longest waveguide gradually blue shifts to 450 nm for the shortest waveguide. Also, the resonance at 450 nm, observed for the largest channel length, blue shifts to a wavelength below 400 nm for waveguides shorter than 400 nm. The broad peak in the long-wavelength range of the spectra also blue shifts as the length of the cavity is decreased, showing a main peak at a wavelength of 650 nm for the shortest waveguides. Furthermore, the lowest-order resonances observed in the three shortest waveguides appear to be much broader than other resonances. This is possibly the result of a longer-wavelength resonance that arises when all propagating modes in the resonator are in cutoff [130].

Fabry-Perot resonances result from interference between forward and backward propagating plasmon waves in the cavity. On resonance, the condition shown in Eq. 3.1 must be fulfilled, with L the length of the waveguide, $k_{spp}(\omega)$ the wave vector of the plasmon at frequency ω, $\Delta\phi_{1,2}$ the phase shifts as a result of plasmon reflection at either end of the waveguide, and m the mode number.

$$2Lk_{spp}(\omega) + \Delta\phi_1 + \Delta\phi_2 = 2\pi m \tag{3.1}$$

Before we can determine the plasmon dispersion in coaxial waveguides, it is necessary to assign mode numbers to the measured Fabry-Perot resonances. With this in mind, we performed exact calculations of $k_{spp}(\omega)$ by solving Maxwell's equations for a cylindrical structure of infinite length [5, 58, 93, 79, 128]. The azimuthal dependence of the electric and magnetic fields in the waveguide is described by the harmonic function $e^{in\psi}$ of order n. Note that we expect to only excite modes of odd azimuthal order in the experiment as the incident electric field has even parity about the center of the waveguide aperture. The radial dependence of the fields in all three domains (Ag-dielectric-Ag) is described by solutions to the second-order Bessel differential equation. We apply a Bessel function of the first kind, J_n, to the Ag core

and a Hankel function of the first kind, $H_n^{(1)}$, to the Ag cladding. Inside the dielectric channel the radial field dependence is described by a linear combination of Bessel and Hankel functions of the first kind. On each domain boundary we formulate four continuity conditions for the tangential components of the electric and magnetic fields. The optical eigenmodes of the coaxial waveguide are found when the determinant of the resulting homogeneous system of eight equations with eight unknown coefficients vanishes, similar to that described in §2.4.

3.3 Comparing Experiment with Theory

In this way dispersion relations were determined for waveguides of any chosen channel width. To account for the tapered profile of the resonators in the experiment, we calculated the effective dispersion relation by index-averaging $k_{spp}(\omega)$ over a series of dispersion curves corresponding to the varying lateral dimensions of the waveguide determined from SEM images (Fig. 3.1). By inserting this index-averaged dispersion into Eq. 3.1, we obtain the resonance frequency as function of cavity length and mode number m. We compared these results to experimental values of the resonance frequency, obtained by fitting the transmittance spectra with Lorentzian line shapes, as a function of waveguide length. This comparison makes it possible to assign mode numbers to the measured resonances and construct the plasmon dispersion relation for the coaxial waveguides. In the following first analysis, we assume that the plasmon phase shift upon reflection at the cavity ends, which will be discussed further on, is zero.

Figure 3.4a shows the dispersion data for coaxial channels with an average outer diameter of ∼175 nm and a ∼50-nm-wide air channel (see Fig. 3.1b) along with the calculated dispersion curve for azimuthal order $n = 1$, taking into account the tapering in the structures as determined from SEM data (Fig. 3.1). Good agreement between experiment and calculations is observed. Different symbols indicate measured resonances characterized by mode numbers, $m = 1$ and 2. Dispersion in air and at a Ag/air interface are plotted for reference. The figure shows up to $\sim$ 60% larger

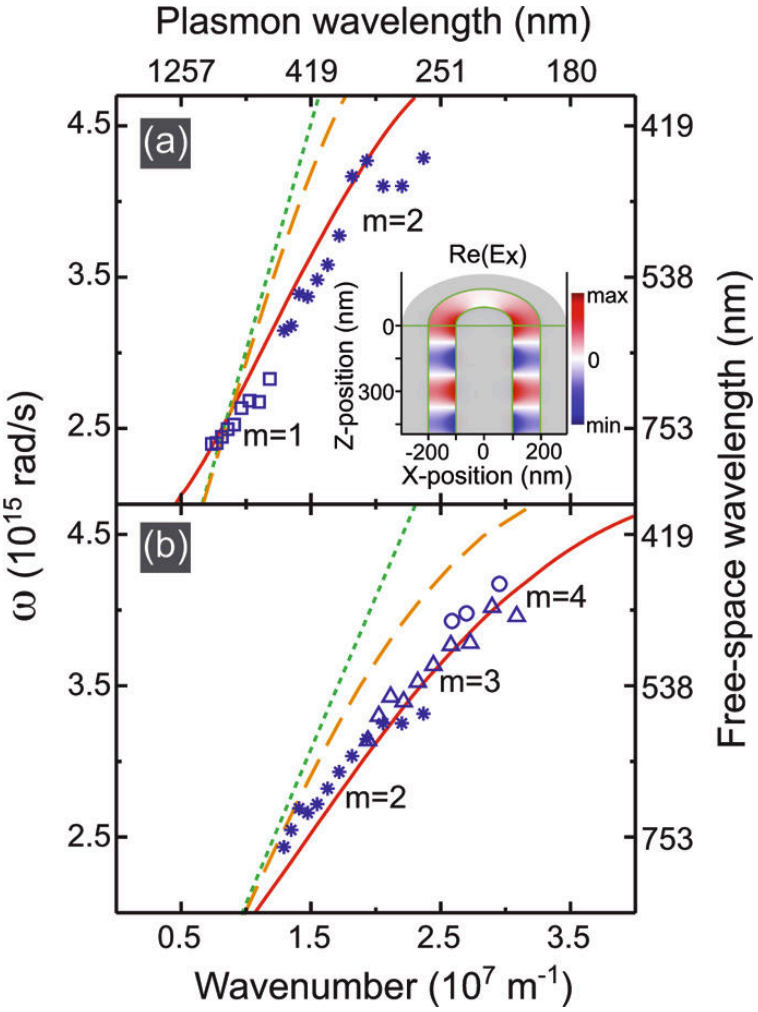

Figure 3.4: Measured dispersion data and calculated index-averaged dispersion relations (red drawn lines) for coaxial plasmon waveguides with (a) ∼50-nm-wide air channel and (b) ∼50-nm-wide spin-on-glass (SOG) filled channel. Light lines for air (a) and SOG (b) are also shown (dotted green lines), along with the plasmon dispersion (dashed orange curves) at a flat Ag/air interface (a) and Ag/SOG interface (b). Symbols in the figure correspond to different Fabry-Perot mode numbers, m, where $\square = 1$, $* = 2$, $\triangle = 3$, and $\circ = 4$. The inset in (a) shows the calculated electric field distribution of the mode of azimuthal order $n = 1$, in an SOG-filled coaxial waveguide with outer radius of 200 nm and channel width of 100 nm at $\omega = 3.5 \times 10^{15}$ rad/s.

wave vectors in coaxial waveguides compared to free space. At lower frequencies $\omega < 2.5 \times 10^{15}$ rad/s, as the mode approaches cutoff, the calculated dispersion relation flattens slightly and crosses the air light line, in agreement with experimental data in that frequency range. This behavior is not observed in studies of cylindrical metal waveguides when the excited plasmon mode has azimuthal symmetry ($n = 0$),[35, 113] as that mode does not experience cutoff.

To further increase the dispersion, we infilled the coaxial nanostructures by spin-coating the sample with a ∼200-nm-thick layer of spin-on-glass (SOG, $n = 1.46$). SEM of FIB-milled cross sections confirmed that SOG infilled the structures entirely. Figure 3.4b shows the dispersion data for infilled coaxial waveguides of the same dimensions as in (a). In this case, resonances with mode numbers $m = 2 - 4$ were observed. We further note a shift of the dispersion data to higher wavenumbers compared to the air case of Fig. 3.4a, as well as a clear increase in the curvature of the dispersion relation. In this case we observe up to ∼2.2 times larger wave vectors in coaxial waveguides compared to free space. Figure 3.4b also shows the calculated plasmon dispersion (red drawn curve).

3.4 The Phase Shift at Reflection

Thus far we have demonstrated cases where the calculated dispersion relations match the experimental data quite well. Figure 3.5a compares the dispersion data (assuming zero phase change on reflection) and calculated dispersion relation (red drawn curve) for air-filled waveguides with a dielectric channel width of ∼100 nm. Although the data follow the same general trend as the calculated curve, the two show a clear offset in wavenumber with respect to each other. In the final part of this chapter we will show that the observed discrepancy between the data and theory results from a net phase shift ($\Delta\phi_1 + \Delta\phi_2$) that the plasmons gain when they reflect off the cavity ends, which can be tuned by changing the cavity geometry.

As Eq. 3.1 shows, a nonzero net phase shift causes the resonance wavelengths to shift. To study the phase shift, we have performed finite difference time domain

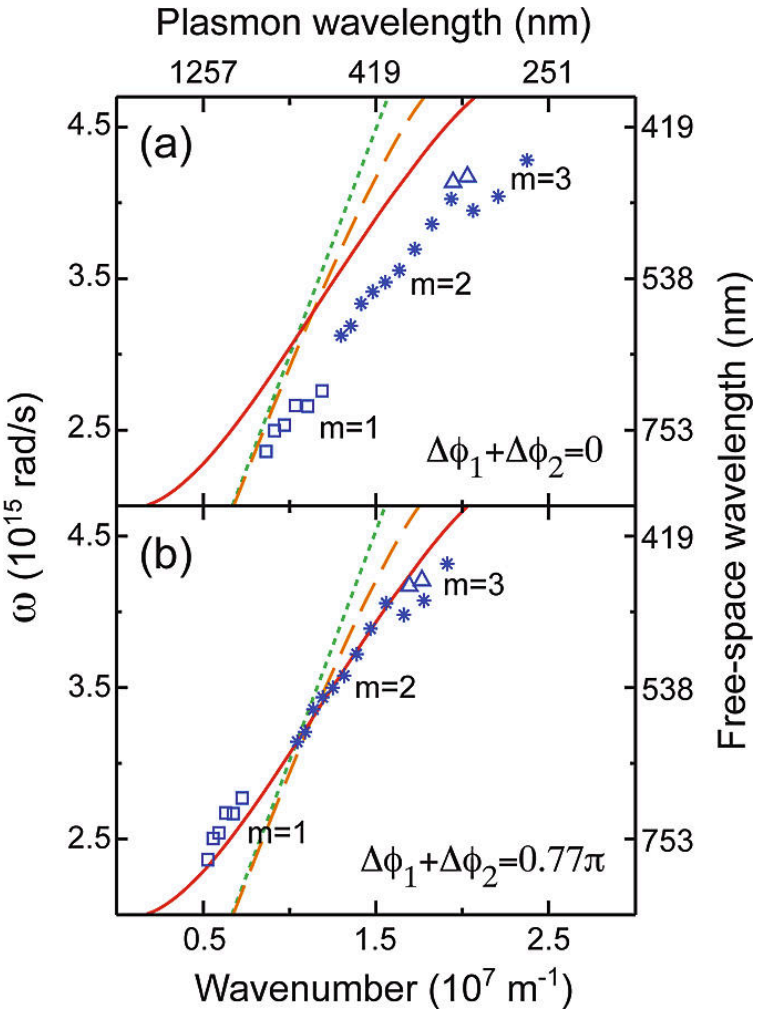

Figure 3.5: Measured dispersion data and calculated index-averaged dispersion relations (red drawn lines) for coaxial plasmon waveguides with a 100-nm-wide air channel. In (a) the dispersion data are plotted, assuming a zero net phase shift as a result of reflections at the end facets of the cavity. In (b) the data are plotted for an overall reflection phase shift of 0.77π, which was determined using simulations. Light lines for air are also shown (dotted green lines), along with the plasmon dispersion (dashed orange curves) at a flat Ag/air interface. Symbols in the figure correspond to different Fabry-Perot mode numbers, m, where $\square = 1$, $* = 2$, $\triangle = 3$.

(FDTD) simulations to obtain the field profile in structures similar to those used in the experiment. In the simulations we used a broad band optical pulse with Gaussian beam profile to excite the structures. By applying a discrete Fourier transform of the time-dependent fields, we obtain the spatial field intensity profiles at any given optical frequency. In Fig. 3.1 we show the simulation results for an air-filled coaxial waveguide of the same dimensions as the structure shown in Fig. 3.1a, excited at an angular frequency of 4.2×10^{15} rad/s (freespace wavelength of 450 nm). Figure 3.6a shows the steady-state intensity distribution in the plane of polarization for the electric field component that is parallel to the polarization direction of the incident light. As in the experiment, the waveguide is excited at the air-side (left-side in the figure).

In the steady state, the field profile in the cavity is a superposition of plasmon waves propagating in forward and backward direction after any number of reflections at the input or distal end of the cavity. The analytical expression of the resulting electric field in the cavity as a function of position in the direction parallel to the waveguide axis, is given by Eq. 3.2, where k is the plasmon wave vector (which depends on z as a result of waveguide tapering),$\langle k \rangle$ is the index-averaged wave vector, and $|r_1|$ and $\Delta\phi_1$ are the reflectance and reflection phase shift at the distal end of the cavity, respectively.

$$E(z) \propto e^{ikz} + |r_1| e^{i(k(L-z)+\langle k \rangle L+\Delta\phi_1)} \tag{3.2}$$

Note that the field profile inside the cavity is not affected by the reflectivity of the input end of the waveguide. In fact, the field profile is simply proportional to the original plasmon wave and the plasmon wave after one reflection, added together.

Figure 3.6b plots the intensity distribution in the cavity as a function of position along the waveguide axis (blue dotted curve), obtained by vertically summing the intensity values in Fig. 3.6a. To obtain the phase shift at the distal end of the waveguide (right end in Fig. 3.6a), we fit the intensity distribution with $|E(z)|^2$ (Eq. 3.2). As the plasmon wave vector is calculated analytically, the only fit parameters, besides an

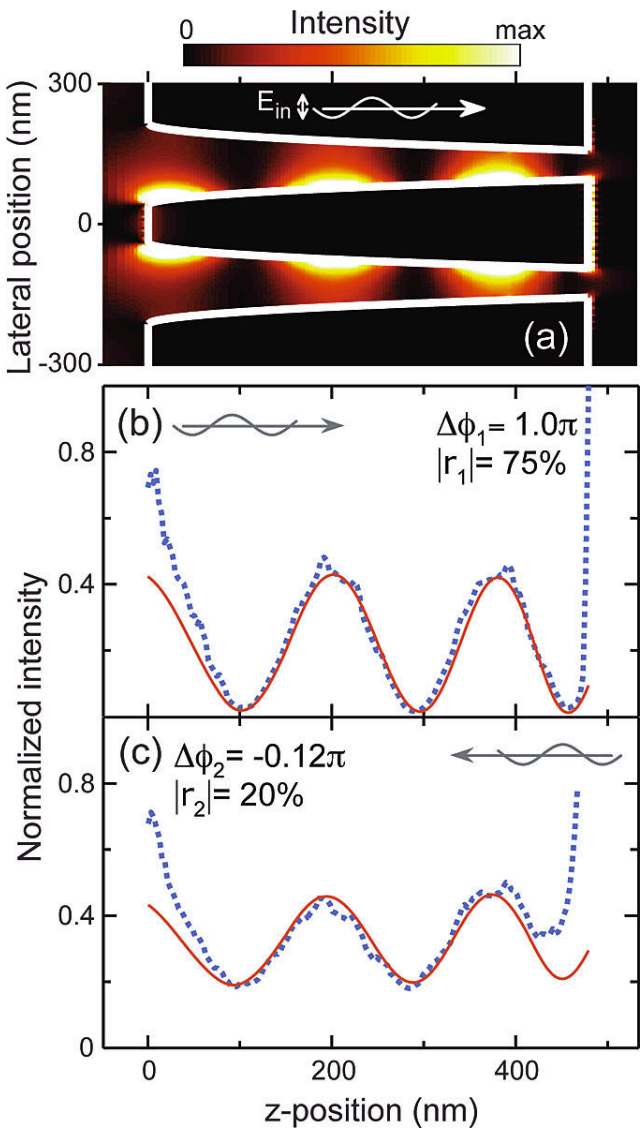

Figure 3.6: Steady-state simulation results of the electric field intensity profile inside a 485-nm-long coaxial cavity with an air-filled ∼100-nm-wide dielectric channel excited at an angular frequency of $\omega = 4.2 \times 10^{15}$ rad/s (freespace wavelength of 450 nm). (a) Electric field intensity distribution inside the coaxial cavity for light incident from the left. (b, c) Intensity as a function of position integrated along the lateral direction (dotted lines) for light incident from the left (b) and right (c). The red drawn curves are fits of the intensity profile that were used to find the reflectance and reflection phase shifts at the distal end facets. The reflection phase shift is 1.0π at the substrate side and -0.12π at the air side of the cavity, while the values for the reflectance are 75% and 20%, respectively.

amplitude constant, are $\Delta\phi_1$ and $|r_1|$. The result of the fit is plotted in Fig. 3.6b (red drawn curve). From the fit it follows that the phase shift as a result of the reflection at the substrate end of the waveguide is close to π. The visibility of the oscillation depends on the reflectance $|r_1|$ at the distal cavity end. On the basis of the fit we find that the reflectance of the substrate-side end facet is equal to 75%.

To obtain the reflection phase shift at the input end facet, $\Delta\phi_2$, the intensity distribution in the waveguide was simulated for light impinging on the nanostructure from the substrate side of the cavity. We show the result of this simulation in Fig. 3.6c. Owing to a lower reflectance of the air-side end facet of 20%, the visibility of the intensity distribution is smaller. Furthermore, we find that the phase shift upon reflection at the air-side cavity end is close to zero. Using the reflectance values as determined from the fits and the calculated waveguide losses, we obtain a cavity quality factor of only $\sim$4, which explains the broad spectral width of resonances in measured spectra. We note, however, that the cavity losses are almost entirely due to the rather poorly reflecting end facets of the cavity. By improving the end face reflectivity, it should be possible to attain quality factors of more than 80. Furthermore, on the basis of comparisons with simulations of untapered waveguides, it is important to note that waveguide tapering does not significantly affect the end facet reflectance and, as a result, does not add to the resonance line width. However, tapering does result in a larger dielectric channel width at the input side of the cavity, which, as shown, may give rise to lower end facet reflectance, resulting in a reduction of the quality factor of the cavity.

3.5 A More Comprehensive Study

The analysis in Fig. 3.6 was done at a frequency of 4.2×10^{15} rad/s (freespace wavelength of 450 nm). At lower frequencies, we find that the overall phase shift tends to decrease (data not shown). The average net phase shift we find for frequencies within the experimental bandwidth equals $\sim 0.77\pi$. In Fig. 3.5b we plot the dispersion relation taking into account this average phase shift and observe a close agreement

between theory and experiment. Note that in our analysis of waveguides with a ∼50-nm-wide dielectric channel (Fig. 3.4) or waveguides filled with SOG, best agreement between experiment and theory was found for phase shifts close to zero, demonstrating that the phase shifts on reflection can be tuned by changing the geometry.

To further investigate the tunability of the reflection coefficients of the coaxial end facets, we simulate the response of waveguides as we vary the refractive index of the dielectric channel and surrounding medium. The simulations are performed using untapered waveguides of 485 nm length and 175 nm outer radius, that are composed of a 75-nm-wide dielectric channel separating a Ag core and cladding.

Figure 3.7 shows the reflectance $|r_1|$ and reflection phase $\Delta\phi_1$ obtained by fitting the longitudinal field intensity profile using Eq. 3.1 for a waveguide with Ag core and cladding and a dielectric channel at $\lambda_0 = 800$ nm. In Fig. 3.7a the refractive index of the dielectric channel is kept fixed at $n_{in} = 1.5$, while the refractive index of the surrounding medium is varied from 1.0 to 3.5. The data demonstrate that the reflection phase depends strongly on the surrounding index and can be tuned to any value between 0 and π. It is worthwhile to note that the observed trend qualitatively agrees with the trend given by a calculation using the Fresnel equations (blue dotted line) using the mode index of the cavity. Quantitatively, however, the trend observed for coaxes is very different, and may only be obtained analytically if we consider mode overlap between waveguide modes, surface waves, and freespace modes. Interestingly, a change in the refractive index of the surrounding medium hardly affects the end facet reflectance of $\sim 70\%$.

Figure 3.7b shows the influence of a change in the dielectric channel index on the reflection coefficients of the coaxial waveguide when the refractive index of the surrounding medium is fixed at $n_{out} = 1.0$. As the refractive index of the dielectric in the coaxial waveguide is increased from 1.0 to 2.5, we find that the end facet reflectance increases from $\sim 55\%$ to $\sim 85\%$, while the phase shift on reflection off the cavity ends remains at a value of $\sim 0.1\pi$. In general, we find that an increase of the effective mode index of the waveguide either by a change in the refractive index of the dielectric or by a change in the geometry leads to an improved cavity end reflectance.

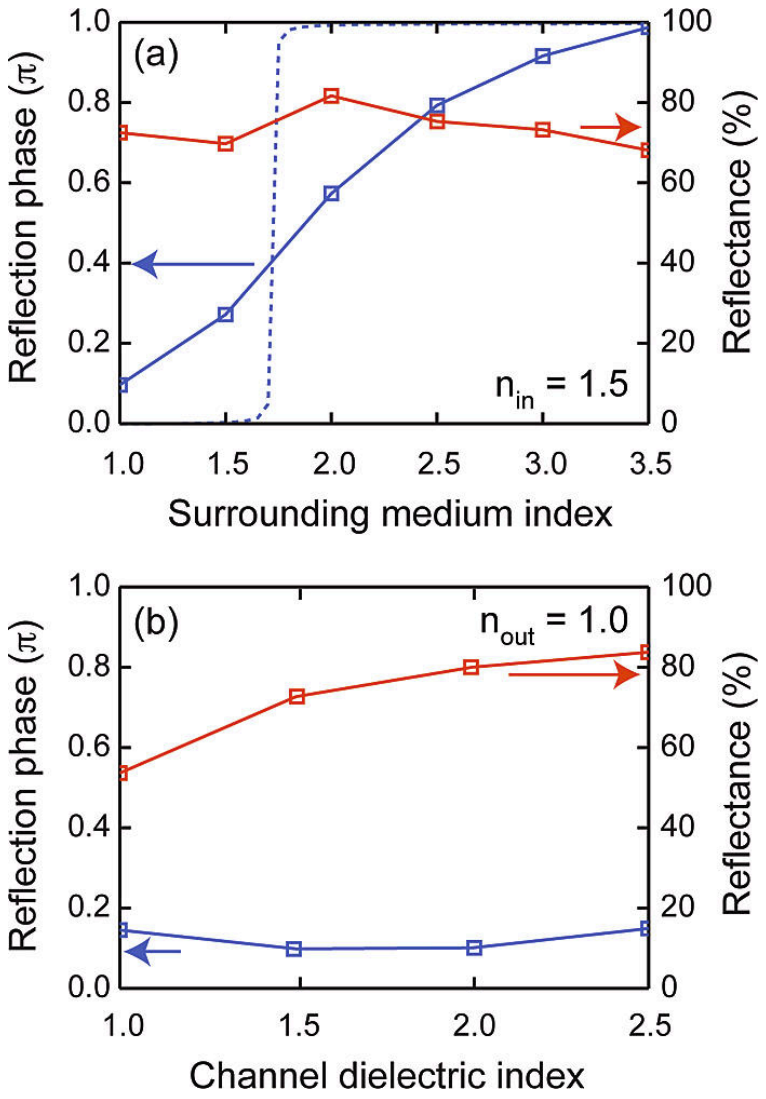

Figure 3.7: Reflection phase ($\Delta\phi$) and reflectance ($|r|$) of the end facets of an untapered coaxial waveguide with 75-nm-wide dielectric channel and outer radius of 175 nm at a wavelength $\lambda_0 = 800$ nm, derived from finite difference time domain simulations. (a) $\Delta\phi$ and $|r|$ are plotted as a function of the surrounding dielectric index for waveguides with fixed dielectric channel index, n_{in}) 1.5. The dotted blue line gives the result obtained from Fresnel equations using the (single) mode index of the coaxial cavity. (b) Plot of $\Delta\phi$ and $|r|$ as a function of the refractive index of the dielectric channel of the coaxial waveguide, while the surrounding dielectric index is kept fixed, $n_{out} = 1.0$.

Figure 3.7 demonstrates that the reflection phase and reflectance of the cavity end facets can be independently tuned. This opens the way to realization of plasmonic cavities with ultrasmall mode volumes, where the reflection phase can effectively cancel the phase accumulated during propagation in the coaxial waveguide [52], enabling cavities with a length considerably shorter than $\lambda/2$. The quality factor of the cavity is mainly dependent on the reflectance of the cavity mirrors, which, as we have shown, can be improved by increasing the effective index inside the coax, for instance, by reducing the dielectric channel width in the cavity. Counterintuitively, a reduction in channel width may thus give rise to a smaller mode volume as well as a greater quality factor.

3.6 Conclusion

In conclusion, we have shown that the plasmon dispersion in coaxial waveguides with subwavelength dimensions can be determined from single-cavity transmission measurements. Our dispersion data agree well with an analytical model for dispersion in coaxial waveguides of infinite length and demonstrate the large degree of tunability by varying the coaxial cavity dimensions and dielectric medium. A plasmon phase shift up to π occurs upon reflection off the cavity ends and strongly affects the cavity resonance. The phase shift depends greatly on the waveguide geometry and dielectric medium inside and outside the cavity, providing further tunability of the coaxial cavity resonances and enabling cavities with ultrasmall mode volumes. The fundamental insights obtained in this chapter are important in further studies of nanoscale waveguiding, field enhancement, and imaging with coaxial cavities, as well as their use in negative-index metamaterials as will be discussed in Chapters 4 and 5.

Chapter 4

Negative Refractive Index in Coaxial Plasmon Waveguides

Abstract: *Having seen in Chapter 3 how we can experimentally measure the positive index mode dispersion of plasmonic coaxial waveguides, in this chapter we focus on a theoretical study showing that coaxial waveguides also exhibit negative refractive index modes over a broad spectral range in the visible. For narrow dielectric gaps (10 nm GaP embedded in Ag) a figure-of-merit of 18 can be achieved at $\lambda_0 = 460$ nm. For larger dielectric gaps the negative index spectral range extends well below the surface plasmon resonance frequency. By fine-tuning the coaxial geometry, the special case of $n = 1$ at a figure-of-merit of 5, or $n = 0$ for a decay length of 500 nm can be achieved.*

4.1 Introduction

Controlling the propagation of light at the nanoscale is one of the challenges in photonics. Surface plasmons, electromagnetic modes that propagate at a metal/dielectric interface, provide a key opportunity to achieve this goal, due to their relatively small evanescent fields [6, 95]. Moreover, as their dispersion can be strongly controlled by geometry, their effective wavelength can be shrunk well below the freespace wavelength, enabling further miniaturization of optical components. Initial experiments on plasmon optics were carried out at planar metal/dielectric interfaces, demonstrating basic control of plasmons. Plasmonic components such as mirrors [141, 126] and waveguides [8, 112] were realized, however, still of relatively large size due to the

$>$ 100-nm evanescent tails, and with limited control over dispersion. Subsequently, dielectric-metal-dielectric structures were investigated, and have demonstrated confinement of light to $<$ 100 nm length scales in taper geometries [127, 132], though at high loss. The reverse, metal-dielectric-metal (MDM) geometries, have demonstrated lower loss, higher dispersion [33, 83], and, recently, the attainment of a negative index of refraction [70, 119, 34].

A disadvantage of planar MDM structures is that they only confine light in one transverse direction. Recently, coaxial MDM waveguides, composed of a metal core surrounded by a dielectric cylinder clad by a metal outer layer have been introduced, that confine light in all transverse directions [44, 5]. We have recently reported optical transmission measurements through single coaxial waveguides, from which the dispersion diagram for these nanoscale waveguides was determined [31].

Inspired by the earlier work on MDM waveguides, a natural question arises: whether coaxial waveguides would posses a negative refractive index, and, if so, for what geometry and over what spectral range. Since the coaxial waveguides are essentially 3-dimensional objects, the observation of negative index in individual coaxes also inspires the design of 3-dimensional negative-index metamaterials [103, 122, 36, 114, 129] composed of arrays of coaxial waveguides [17].

Here, we theoretically study the dispersion of coaxial Ag/Si/Ag plasmon waveguides and demonstrate that, for well-chosen geometries, modes with a negative refractive index are observed. These modes are dominant over other waveguide modes for a wide range of frequencies above the surface plasmon resonance frequency. We discuss the influence of waveguide geometry and material on the mode index and demonstrate that the figure-of-merit (FOM), defined as the magnitude of the real part of the propagation constant in the waveguide divided by the imaginary part [34, **?**], can be as high as 18.

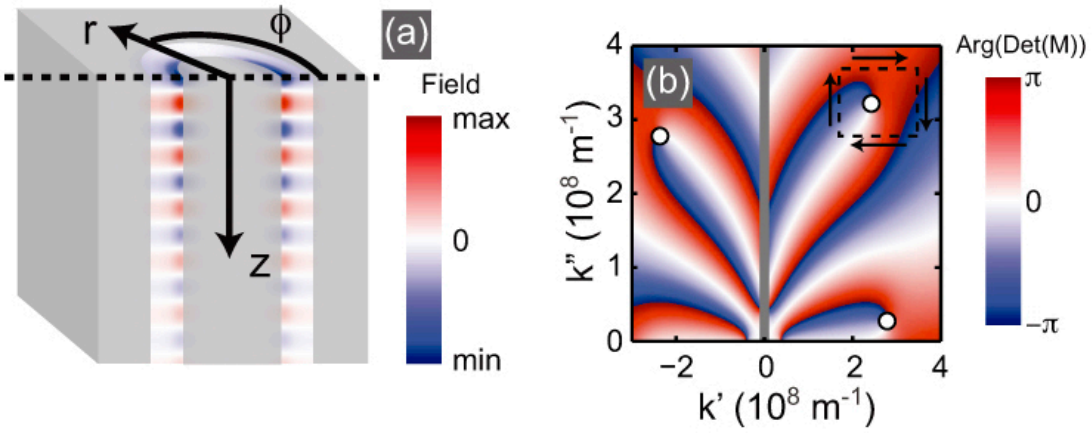

Figure 4.1: Coaxial plasmon waveguide geometry and numerical mode solving method. (a) Schematic cross-section of a coaxial waveguide with the definition of the cylindrical polar coordinates, r, ϕ and z. The metallic inner core and outer cladding separate a dielectric channel. A schematic wave propagating in the waveguide in the direction of positive z is also indicated. (b) Argument θ of the determinant, $\det[M(k)]$, plotted in the complex k-plane for a Ag/Si/Ag waveguide with 75 nm inner core diameter and 10-nm-wide dielectric channel at $\omega = 3 \times 10^{15}$ rad/s . By cycling around the closed loop, indicated by the dashed square, the net number of discontinuities in θ is determined. Zero positions are indicated by the white circles.

4.2 Anlaytic Methods

The azimuthal dependence of the fields is described by the harmonic function $e^{in\phi}$ of order n. In the remainder we only consider modes with $n = 1$, since these are the lowest order modes that couple to freespace radiation. As seen in §3.2, the radial dependence of the fields in all three domains (metal-dielectric-metal) is described by solutions to the 2^{nd} order Bessel differential equation. We apply a Bessel function of the first kind, J_n, to the metal core, as that function remains finite at the waveguide axis. A Hankel function of the first kind, $H_n^{(1)}$, is applied to the metal cladding. Inside the dielectric channel the radial field is described by two linearly independent cylinder functions. The arguments of the cylinder functions in each of the three domains is $\kappa_i r$, where κ_i is the radial wave number in medium i, defined via Eq. 4.1 where ϵ_i is the complex dielectric constant in domain i. To satisfy the condition that fields decay to zero at radial infinity, we take the square root of Eq. 4.1, such that the radial wave number has a positive imaginary part.

$$\kappa_i^2 = \epsilon_i \frac{\omega^2}{c^2} - k^2 \tag{4.1}$$

On each domain boundary we formulate four continuity conditions for the tangential components of the electric and magnetic fields. The optical eigenmodes of the coaxial waveguide are found when the determinant of the resulting homogeneous system of eight equations with eight unknown coefficients vanishes (Eq. 4.2), where M is the matrix of the system of equations.

$$\det[M(k)] = 0 \tag{4.2}$$

We have used two independent methods for determining the optical modes, $k(\omega)$, of the structure. One involved a numerical procedure developed to detect local minima of the determinant of the system in the complex k-plane. The other method relies on the fact that the argument, θ, given by 4.3 is undefined when $\det[M(k)] = 0$.

$$\det[M(k)] = |\det[M(k)]|\, e^{i\theta} \tag{4.3}$$

This can be visualized in a plot of θ in the complex k-plane. An example is shown in Fig. 4.1(b), where θ is plotted for a coaxial waveguide with a Ag core and cladding and a 10 nm silicon spacer layer. We used empirically determined optical constants for the metal [64] and dielectric [97]. Contour lines in the figure appear to close in on each other at each of the zeros, which are indicated by the white dots in the figure. By counting each discontinuity $-\pi \to \pi$ and $\pi \to -\pi$ about a closed loop in the figure (for an example, see the dashed square loop in Fig. 4.1b) we are able to determine the number of zeros in the enclosed area. In case we find that one or more zeros reside in the area, we split the area up in smaller pieces and repeat the procedure until the location of the zero(s) is determined with double computer precision.

Using this method, solutions for k were found for real frequency, so that dispersion relations, $\omega(k)$, could be constructed. Calculations were performed in the optical angular frequency regime 1×10^{15} rad/s $< \omega < 5 \times 10^{15}$ rad/s (free-space wavelength,

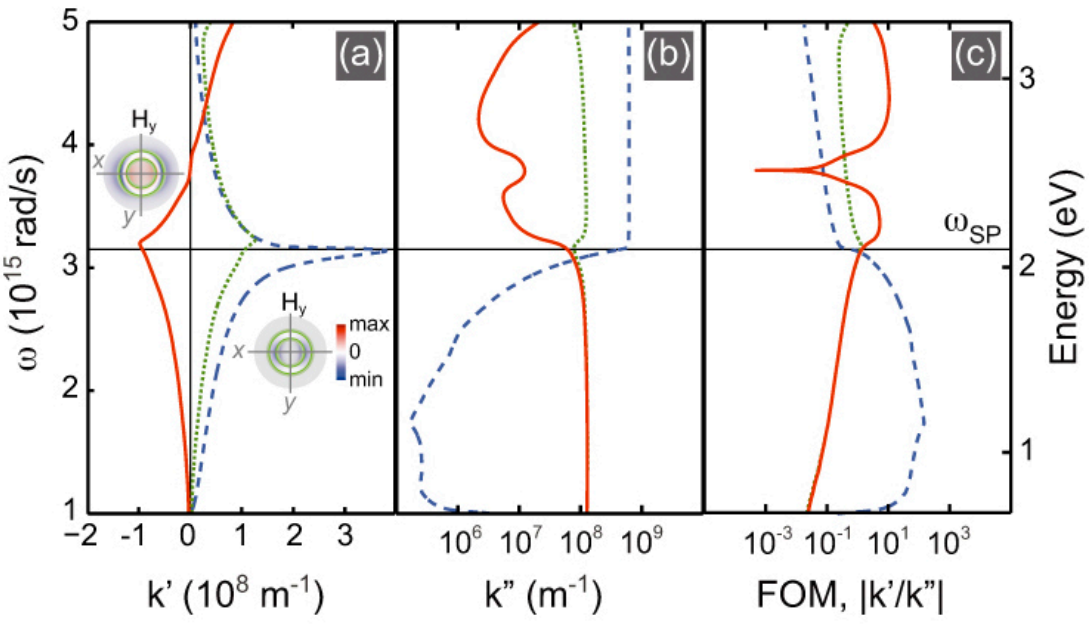

Figure 4.2: Dispersion relations of the three lowest-order modes of a coaxial waveguide with 75-nm-diameter Ag core, 25-nm-wide Si channel, and infinite outer Ag cladding. Radial frequency is plotted versus propagation constant k' (a), attenuation constant k'' (b), and figure-of-merit k'/k'' (c). The Ag/Si surface plasmon resonance frequency $\omega_{SP} = 3.15 \times 10^{15}$ rad/s ($\lambda_0 = 598$ nm) is indicated by the horizontal line. Panel (a) shows two modes with positive index (blue dashed curve and green dotted curve) and one mode with a negative index below a frequency of $\sim 3.8 \times 10^{15}$ rad/s (red drawn curve). The insets in (a) show the H_y field distribution in the transverse plane of the waveguide at 2.8×10^{15} rad/s for the positive-index mode (blue dashed dispersion curve) and at 3.6×10^{15} rad/s for the negative-index mode.

λ_0 = 377–1884 nm). We only consider modes with positive energy velocity, v_e, or equivalently, positive attenuation constant k'' [34]. Therefore, to achieve antiparallel energy and phase velocity, which is the unique requirement for a negative mode index, the propagation constant k needs to be negative.

4.3 Coaxial Waveguide Dispersion

Figure 4.2 shows the dispersion relation, $\omega(k)$, for the three lowest-order modes in a coaxial waveguide consisting of a 75-nm-diameter Ag core, surrounded by a 25-nm-thick Si layer and infinite Ag cladding. In (a) the angular frequency is plotted against

k', while (b) shows the frequency as function of k'', which determines the propagation length of light in the waveguide via Eq. 4.4. The surface plasmon resonance frequency $\omega_{SP} = 3.15 \times 10^{15}$ rad/s ($\lambda_0 = 598$ nm) is indicated by the horizontal line.

$$L = \frac{1}{2k''} \tag{4.4}$$

Figure 4.2a shows two coaxial modes (blue dashed line and green dotted line) with positive propagation constants over the entire spectral range. Both dispersion curves closely resemble the dispersion of a surface plasmon polariton propagating along a planar Si/Ag interface. However, the corresponding propagation constants (Fig. 4.2a), are nearly three times as large as for the planar single interface plasmon. This is due to the fact that confinement of the plasmon in the coaxial waveguide geometry leads to larger mode overlap with the metal. Figure 4.2a also shows the existence of a third mode (red drawn curve) that has a negative propagation constant k for frequencies below 3.8×10^{15} rad/s ($\lambda_0 = 496$ nm). The effective index $n = ck'/\omega$ ranges from $9 < n < 5$ in the frequency range of Fig. 4.2. The insets in (a) show the H_y field in the transverse plane for the negative-index mode (calculated at $\omega = 3.6 \times 10^{15}$ rad/s), as well as for the most dispersive positive mode (blue dashed curve in Fig. 4.2a, $\omega = 2.8 \times 10^{15}$ rad/s). From the images it is clear that the mode with positive effective index has a symmetric field distribution with respect to the two centers of the dielectric channel on the x-axis. The H_y field is primarily concentrated at the boundary between the metal core and dielectric channel. The negative-index mode, in contrast, has its field primarily concentrated at the outermost channel boundary and has an H_y field distribution that is anti-symmetric about the center of the dielectric channel, similar to modes with negative index in planar metal-dielectric-metal waveguides [34].

Figure 4.2(b) shows that for frequencies below the surface plasmon resonance frequency ω_{SP}, the lowest-order positive-index mode (blue dashed line) has lowest loss and will therefore be dominant over other modes. Interestingly, above $_{SP}$ the negative-index mode (red curve) becomes the dominant mode, as its losses are significantly

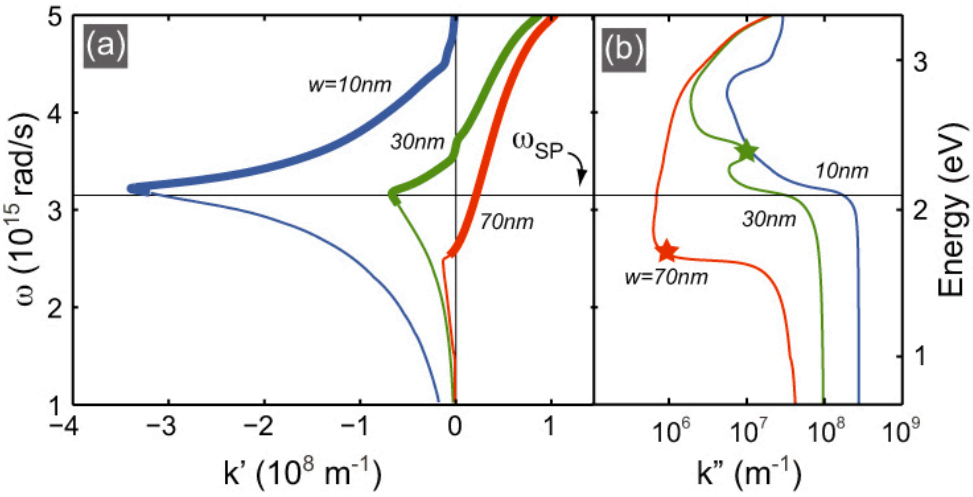

Figure 4.3: Dispersion relations for negative-index coaxial waveguides with Ag core and cladding and Si dielectric channel, (a): $\omega(k')$; (b): $\omega(k'')$. The inner core diameter is fixed at 75 nm, and the Si-channel thickness w is 10 nm, 30 nm, and 70 nm. Positive-index modes [as shown in Fig. 4.2(a)] are not shown in the figure. The bold sections of the dispersion curves indicate the spectral range over which the negative-index mode is dominant, i.e., has lower loss than the positive index modes. The frequency where the red and green dispersion curves cross $k' = 0$ is indicated by the star-symbols.

lower than those for the positive-index modes. Figure 4.2(c) shows the figure-of-merit (FOM), k'/k'', of the modes. As can be seen, the negative-index mode has a FOM that approaches 10 for a narrow frequency interval around 3.4×10^{15} rad/s ($\lambda_0 = 554$ nm). The data in Fig. 4.2 clearly demonstrate that dominant modes of negative index indeed exist in coaxial plasmon waveguides.

4.4 Conditions for Achieving a Negative Mode Index

Next, we investigate the conditions that are required to achieve a negative index by varying the geometry and materials of the waveguide. Figure 4.3 shows the effect of changing the dielectric layer thickness on the dispersion of the negative index mode. Calculations were performed for a Ag/Si/Ag coaxial waveguide with a core diameter of 75 nm for a dielectric layer thickness of 10 nm, 30 nm, and 70 nm. Figure 4.3a

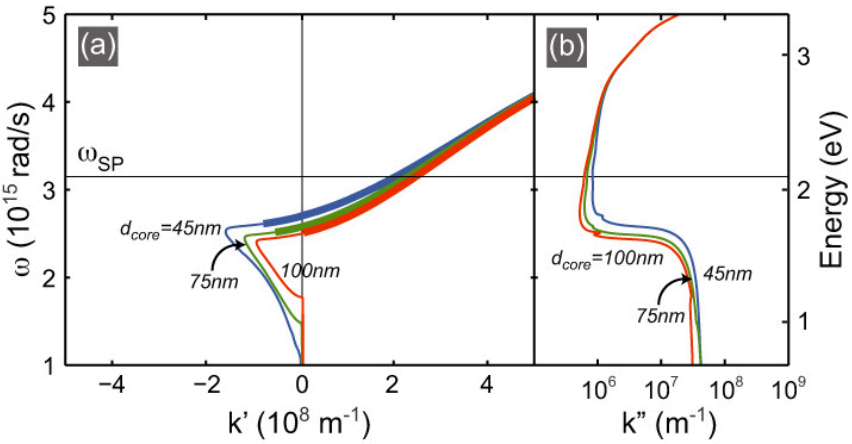

Figure 4.4: Dispersion relations for coaxial waveguides with Ag core and cladding and 70-nm-wide Si dielectric channel, (a): $\omega(k')$; (b): $\omega(k'')$. The inner core diameter, d_{core}, is 45 nm (blue curves), 75 nm (green curves) and 100 nm (red curves). Only modes with negative index are plotted. Bold lines indicate the spectral range where the mode is dominant over the positive-index mode.

shows that the variation in dielectric layer thickness has a very dramatic effect on the dispersion of the negative-index mode. First of all, the largest negative index is observed for the thinnest dielectric. Second, while for the 10-nm and 30-nm dielectric gaps the frequency of the resonance associated with the negative index mode appears close to the surface plasmon resonance at 3.2×10^{15} rad/s, for the 70-nm gap this resonance is significantly red-shifted to 2.5×10^{15} rad/s. The spectral range over which the mode is dominant, indicated by the bold curves in Fig. 4.3a, also extends to lower frequencies when increasing the channel width. For the 70-nm gaps a narrow frequency range is found near 2.4×10^{15} rad/s ($\lambda_0 = 785$ nm), where the index is negative and the figure-of-merit is 5.

As the dispersion branches cross the $k'' = 0$ line, the effective refractive index of the mode vanishes [3]. Coaxial waveguides with a narrow dielectric gap suffer high loss at this frequency. The green star in Fig. 4.3(b) indicates the frequency at which the dispersion curve crosses the $k' = 0$ line for the 30-nm gap; a high value of $k'' = 10^7$ m^{-1} is found. In contrast, for the 70-nm-wide dielectric channel waveguides, the losses at the $k' = 0$ crossing (red star in Fig. 4.3b) are much lower ($k'' < 10^6$ m^{-1}),

corresponding to a decay length of 500 nm. Note that in the spectral range where the phase velocity ω/k' goes to zero, the group velocity, $v_g = d\omega/dk$, is much larger than zero.

The two striking effects observed here are: a) waveguide resonances that shift with geometry, and b) increased propagation length for $k' = 0$ modes for increasing dielectric thickness are in strong contrast to what is observed in planar metal-dielectric-metal waveguides [34]. This suggests that coupling of plasmon fields across the nanoscale diameter of the metal core strongly influences the dispersion of the negative index modes. To investigate this, we studied the influence of the metal core diameter on the dispersion of the mode, while keeping the channel width fixed to 70 nm. Figure 4.4 shows the results for waveguides with inner core diameters of 45, 75 and 100 nm. The figure shows that the spectral range where the mode is both dominant and characterized by a negative index becomes smaller, going from a 45-nm-diameter core to a 75 nm core, and vanishes when the core size is increased to 100 nm. This behavior coincides with a red-shift of the resonance in k'' when the core diameter is increased (Fig. 4.4b). We attribute the resonance red-shift for increasing core diameter to a depolarization effect similar to what is known for bulk metallic particles, which show a plasmon resonance red-shift for increasing diameter [81]. Based on this insight, we predict that a large degree of control over dispersion and resonance red-shift may also be attained in planar structures composed of a multi-layered stack of metal and dielectric. In fact, negative index materials based on metal-dielectric multi-layers have been reported in literature [63]. A final observation that can be made in Fig. 4.4 regards the special case of $n = -1$; for a coaxial waveguide with a core diameter of 50 nm and a 70-nm-wide Si channel, a mode with $n = -1$ is observed with a FOM=5 at $\omega = 2.61 \times 10^{15}$ rad/s ($\lambda_0 = 720$ nm).

4.5 Effect of Materials and Geometry

Thus far we have studied the influence of the coax geometry on the frequency dispersion of k. Next, we will investigate the effect of changing the type of metal in core

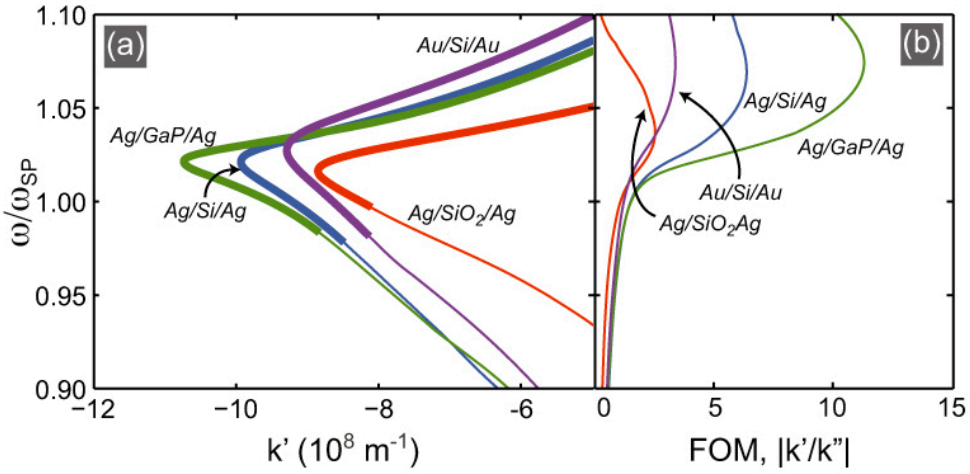

Figure 4.5: Dispersion relations for coaxial waveguides with 75-nm-diameter metal core, 25-nm-wide dielectric channel and infinite metal cladding, (a): $\omega(k')$; (b): FOM k'/k''. The type of metal in the core and cladding, as well as the dielectric material, was varied. The frequency axes are normalized to the corresponding surface plasmon resonance frequency ω_{SP} . Blue curves are for a Si channel surrounded by Ag ($\omega_{SP} = 3.15 \times 10^{15}$ rad/s), green curves for GaP in Ag ($\omega_{SP} = 3.49 \times 10^{15}$ rad/s), red curves for SiO_2 in Ag ($\omega_{SP} = 5.24 \times 10^{15}$ rad/s) and purple curves for Si in Au ($\omega_{SP} = 2.77 \times 10^{15}$ rad/s). Bold curves indicate the spectral range where the negative-index mode is dominant.

and cladding, as well as the dielectric in the cylindrical channel. Figure 4.5 shows the frequency dispersion for a coaxial waveguide with inner metal core diameter of 75 nm and dielectric channel width of 25 nm surrounded by an infinite metal cladding. We compare the results for Si (blue curves), GaP (green curves), and silica (red curves) channels in Ag, and for a Si channel in Au (purple curves). The curves are normalized to the surface plasmon resonance frequency for the corresponding planar metal/dielectric geometry. Interestingly, coaxial plasmon waveguides support dominant negative index modes regardless of the investigated choice of materials. The propagation vector k' is most strongly negative for waveguides filled with GaP and least negative for silica, which indicates that, to obtain a strong effect, the dielectric constant needs to be high ($n_{GaP} = 3.5$ at the GaP/Ag surface plasmon resonance). The figure-of-merit for the modes in Fig. 4.5a is plotted in Fig. 4.5b. Due to the low loss and high index of GaP, the highest figure-of-merit is found in these waveguides. The highest number we found (FOM = 18) was for a 10-nm-wide GaP channel in Ag at $\omega = 4.1 \times 10^{15}$ rad/s ($\lambda_0 = 460$ nm, data not shown). Waveguides composed of Au show a lower FOM than those with Ag, which is attributed to the higher losses in Au.

4.6 Visualizing the Negative Index Mode

Finally, in Fig. 4.6 we present the field distribution in a coaxial waveguide with negative index. Figure 4.6a shows the H_y-field on the outer metal-dielectric interface of a coaxial waveguide with 75-nm-diameter Ag core and 25-nm-wide GaP channel for a frequency $\omega = 3.75 \times 10^{15}$ rad/s ($\lambda_0 = 460$ nm, $\omega/\omega_{SP} = 1.08$ text in Fig. 4.5). Clearly, the phase fronts in the waveguide are not planar. As a result, a non-zero z-component of the electromagnetic field is observed. Figure 4.6b shows the distribution of H_r in the transverse plane. Its magnitude is similar to that of the H_y-field. For completeness, Figs. 4.6c and 4.6d show the H_ϕ and H_z components of the field. Note that these fields are antisymmetric with respect to the center of the dielectric channel and are located mostly inside the metal.

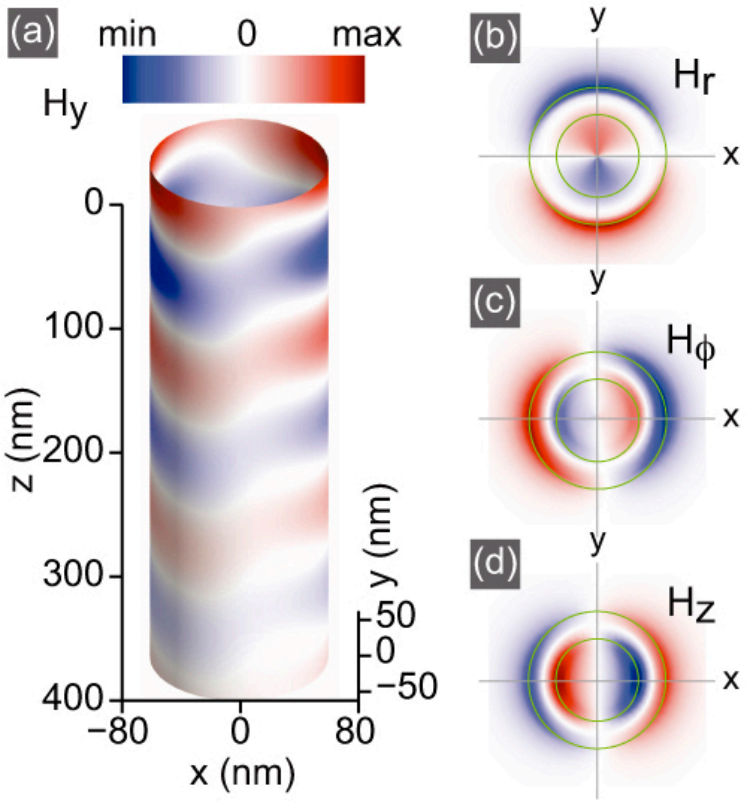

Figure 4.6: Magnetic field images of a coaxial waveguide with 75 nm Ag core diameter, 25-nm-wide GaP-filled ring and infinite Ag cladding at a frequency of 3.75×10^{15} rad/s . In (a) we plot the H_y field distribution on the boundary of the Ag cladding with the dielectric channel. Note that the phase-fronts in the waveguide are in general not perpendicular to the optical axis (z-axis). In (b-d) we plot the polar magnetic field components in the transverse plane. The amplitude of the fields plotted in the figure has the same order of magnitude in all of the four panels.

4.7 Conclusion

We have theoretically demonstrated that coaxial plasmon waveguides sustain modes with negative refractive index at optical frequencies. The negative-index modes have a larger prop- agation length than the positive-index modes over a large spectral range, depending on the dielectric thickness. For a 10-nm-wide GaP dielectric and a 75-nm-wide Ag core, a figure-of-merit $k'/k'' = 18$ is found at $\lambda_0 = 460$ nm. For Ag/Si/Ag coaxial waveguides with increasing Si-channel thickness, the dominant negative-index mode shifts well below the surface plasmon resonance frequency: for a 70-nm Si-channel it is found at $\lambda_0 = 750$ nm. The mode index can be fine-tuned to a value of -1 with a figure-of-merit as high as 5 at $\lambda_0 = 720$ nm. At slightly higher frequencies, the same mode has an effective index $n = 0$ with positive group velocity, and a decay length of 500 nm. Overall, higher tunability and figure-of-merit are found for coaxial waveguides of Ag rather than Au, and filled with a dielectric of highest optical constant. Based on the large degree of dispersion control that can be achieved with coaxial plasmon waveguides, we anticipate that these structures will find use in new designs for nanoscale photonic integrated circuits (waveguides, splitters, multiplexers), in invisibility cloaks, and three-dimensional negative-index metamaterials, as will be discussed in the next chapter.

Chapter 5

A Single-Layer Wide-Angle Negative-Index Metamaterial at Visible Frequencies

Abstract: *In the last two chapters, we have seen how we can measure the dispersion of plasmonic coaxial waveguides and access their negative index modes. In this chapter, we demonstrate how we can couple an array of negative index coaxial waveguides to serve as a single-layer wide-angle negative-index metamaterial at visible frequencies. Metamaterials are materials with artificial electromagnetic properties defined by their sub-wavelength structure rather than their chemical composition. Negative-index materials (NIMs) are a special class of metamaterials characterized by an effective negative index that gives rise to such unusual wave behaviour as backwards phase propagation and negative refraction. These extraordinary properties lead to many interesting functions, such as sub-diffraction imaging [103, 45] and invisibility cloaking [2, 18, 73, 105]. So far, NIMs have been realized through layering of resonant structures, such as split-ring resonators, and have been demonstrated at microwave[101, 117] to infrared [36, 37, 115, 144] frequencies over a narrow range of angles-of-incidence and polarization. However, resonant-element NIM designs suffer from the limitations of not being scalable to operate at visible frequencies because of intrinsic fabrication limitations[38], require multiple functional layers to achieve strong scattering[144, 38], and have refractive indices that are highly dependent on angle of incidence and polarization. Here we report a metamaterial composed of a single layer*

of coupled plasmonic coaxial waveguides that exhibits an effective refractive index of -2 *in the blue spectral region with a figure-of-merit larger than 8. The resulting NIM refractive index is insensitive to both polarization and angle-of-incidence over a* $\pm 50^{\circ}$ *angular range, yielding a wide-angle NIM at visible frequencies.*

5.1 Introduction

Negative-index materials were first predicted theoretically by Veselago [136] in 1968, but it was only in the late 1990s that Pendry [104] defined NIM designs suitable for experimental realization. In these resonant-element based NIMs, the unusual 'left handed' behaviour of light originates from subwavelength resonant elements that behave like 'artificial atoms' with engineered diamagnetic resonances that are the source of the materials' negative-index response. As such, NIMs were first demonstrated experimentally with arrays of millimetre-size copper strips and split-ring resonators operating at microwave frequencies [104, 121]. This discovery sparked a considerable effort to scale down the size of the constituent resonant components to enable operation at higher frequencies. As a result, micrometre-size structures have been successfully fabricated to produce negative refractive indices at terahertz frequencies. More recently, NIMs have been fabricated to operate in the near-infrared spectral region. However, for operation at optical frequencies, the required size of sub wavelength scatterers is very close to practical fabrication limits. So far, the highest reported operational frequency of NIMs has been demonstrated at the deep-red side of the visible spectrum ($\lambda_0 = 780$ nm), using fishnet structures with features as small as 8 nm [38]. Moreover, to achieve strong scattering, the material was built up from a stack of multiple physical layers, thus complicating the fabrication of resonant-element based NIMs for operation at visible frequencies.

Recently, using waveguides, a conceptually different approach was taken to achieve a negative refractive index in the optical spectral range. Investigation of the mode structure of two-dimensional metal/dielectric/metal (MDM) plasmonic slab waveguides [34, 70] reveals that certain MDM waveguide geometries support negative- index

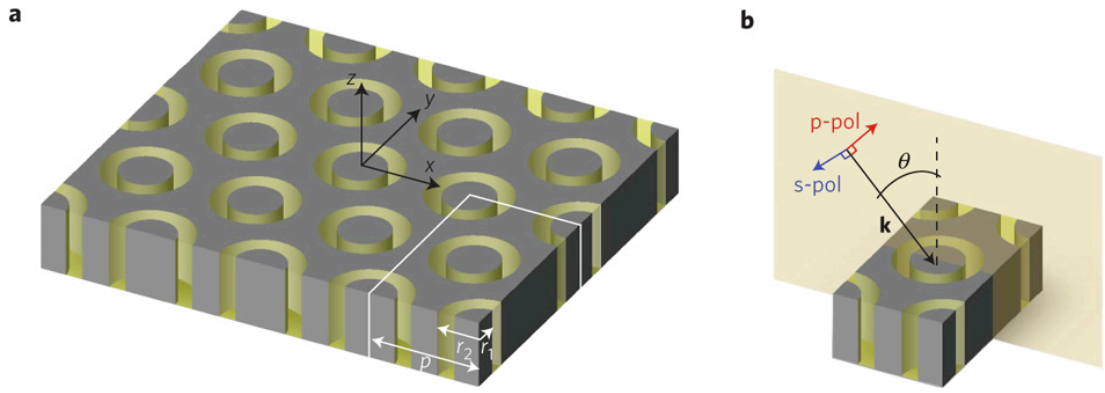

Figure 5.1: Negative-index metamaterial geometry. (a) Single-layer NIM slab consisting of a hexagonal array of subwavelength coaxial waveguide structures. The inner radius r_1, outer radius r_2 and array pitch p are defined in the image. (b) Unit cell of the periodic structure. The angle-of-incidence θ is shown, as well as the in-plane (p-) and out-of-plane (s-) polarization directions associated with the incident wavevector $\mathbf{k}$.

modes at visible frequencies. Arrays of such negative-index MDM slab waveguides can serve as a quasi three-dimensional metamaterial [119]. However, the negative-index mode in MDM waveguides [34] can only be excited from free space with the perpendicular polarization and off-normal angles of incidence because of the polarization and symmetry of the mode, respectively.

These practical limitations of planar MDM geometries can be circumvented in a coaxial MDM geometry in which the planar MDM waveguide is wrapped onto itself (Fig. 5.1). Similar to the modes supported by planar MDM plasmonic waveguides, the coaxial waveguide geometry is found to also support field symmetric and antisymmetric modes that correspond to positive- and negative-index modes, respectively. However, unlike planar MDM waveguides, calculations of individual MDM plasmonic coaxial waveguides show a negative-index mode that, owing to the cylindrical symmetry of the structure, is accessible from free space independent of both incidence angle and polarization. Here, we demonstrate that a two-dimensional array of vertically oriented MDM coaxial waveguides, arranged in a dense hexagonal configuration, functions as a single-layer wide-angle negative index material down to the blue part of the visible spectrum. Through parameter retrieval analysis, we verify the NIM to

have a double-negative [25] index band in the 450 – 500 nm spectral range. Furthermore, we find that the effective refractive index of this geometry is insensitive to both polarization and angle of incidence up to ±50°. Unlike the wire arrays of Liu et al., which exhibit negative refraction but not a negative index [74], the coupled coaxial waveguide array exhibits a true negative refractive index characterized by negative refraction and backwards phase propagation.

Figure 5.1a schematically depicts the NIM, consisting of a hexagonal close-packed array of Ag/GaP/Ag MDM coaxial waveguides composed of 25-nm GaP annular channels with a 75-nm inner diameter set at a pitch of p=165nm in a Ag layer. We study the metamaterial response both by analytic waveguide modal analysis for single coaxial structures, and using finite-difference time-domain (FDTD) simulations for the array of coupled coaxial waveguides.

5.2 Isolated Coaxial Waveguide Dispersion

To estimate the effective refractive index of the material, we first calculate the mode index dispersion of the constituent coaxial elements by solving Maxwells equations in cylindrical coordinates [5, 93] for a single MDM coaxial waveguide of infinite length.

As discussed in §4.2, the dispersion relation of the constituent coaxial elements is calculated by solving Maxwell's equations in cylindrical coordinates for a single MDM coaxial waveguide of infinite length. The azimuthal dependence of the electric and magnetic fields in the waveguide is described by the harmonic function $e^{in\psi}$ of order n. We consider only the modes with $n = 1$, as these are the lowest order linearly polarized modes that most strongly couple to freespace radiation. The radial dependence of the fields in all three domains (metal-dielectric-metal) is described by solutions to the second order Bessel differential equation. We apply a Bessel function of the first kind J_n to the Ag core; a Hankel function of the first kind H_n to the Ag cladding; and a linear combination of both J_n and H_n functions to the dielectric channel. On each domain boundary we formulate four continuity conditions for the tangential components of the electric and magnetic fields. The optical eigenmodes of

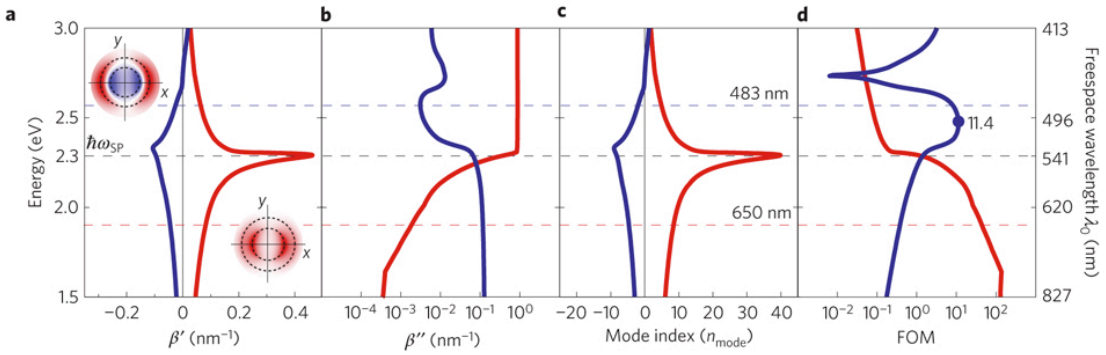

Figure 5.2: Coaxial waveguide dispersion relations. The coaxial waveguide consists of an infinitely long 25-nm GaP annular channel with a 75-nm inner diameter embedded in Ag. Plotted are the two lowest-order linearly polarized modes that most strongly couple to free space radiation. (ac), Energy is plotted versus β' (a), β'' (b), and mode index n_{mode} (c). (d) The figure-of-merit FOM $= |\beta'/\beta''|$. The Ag/GaP planar surface plasmon energy at $\hbar\omega_{SP} = 2.3$ eV ($\lambda_0 = 540$ nm) is indicated by the black dashed horizontal line. All panels show one mode with positive index (red curve) and one mode with a negative index (blue curve) below an energy of 2.7 eV ($\lambda_0 = 460$ nm). The insets in (a) show the Re(H_y) (out-of-page) field distribution in the waveguide at a wavelength of $\lambda_0 = 650$ nm for the positive-index mode and at $\lambda_0 = 483$ nm for the negative-index mode.

the coaxial waveguide are found when the determinant of the resulting homogeneous system of eight equations with eight unknown coefficients vanishes.

The waveguide eigenmodes are characterized by a complex propagation constant along the z axis $\beta(\omega) = \beta' + i\beta''$,where β' and β'' are the real and imaginary parts of the propagation constant, respectively. Complex optical constants for Ag [64] and GaP [97] are taken from tabulated literature data.

Figure 5.2a and b show the calculated dispersion relations $\omega(\beta')$ and $\omega(\beta'')$ of a single Ag/GaP/Ag coaxial waveguide. The mode index $n_{mode} = c\beta'/\omega$ is plotted in Fig. 5.2c. Similar to what is reported for planar MDM structures [34], we find one mode with a positive index over the entire spectral range (red curve), and a second mode with a negative index for energies below 2.7 eV (blue curve). The index of the second mode ranges from $-9 < n_{mode} < 1$ in the energy range of Fig. 5.2. The insets in Fig. 5.2a show the Re(H_y) field profiles corresponding to the positive-index mode at $\lambda_0 = 650$ nm ($n_{mode} = 8.5$) and the negative-index mode at $\lambda_0 = 483$ nm

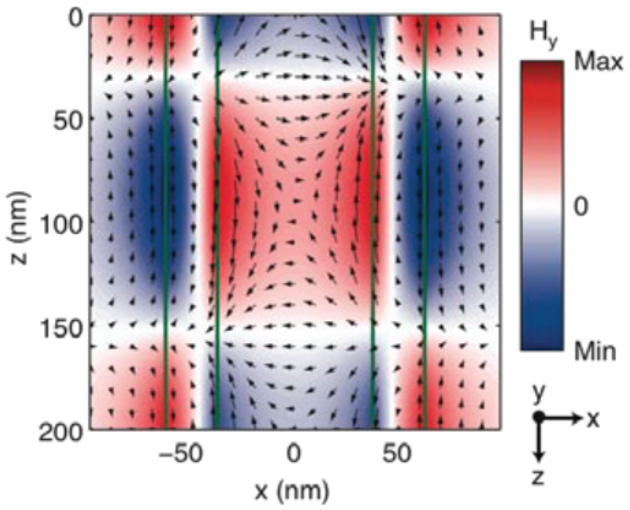

Figure 5.3: Coaxial waveguide negative-index mode. Lateral cross-section of a coaxial waveguide consisting of an infinitely long 25-nm GaP annular channel with a 75-nm inner diameter embedded in Ag. The dielectric channel is schematically indicated. Plotted is the real part of the H-field distribution of the $n = 1$ negative index mode at $\lambda_0 = 483$ nm, where n refers to the azimuthal dependence of the fields. The in-plane $\mathrm{Re}(H_{xz})$ field distribution is depicted with arrows, while the out-of-plane $\mathrm{Re}(H_y)$ fields are plotted using a color scale.

($n_{mode} = -2.0$). A full field map of the negative-index mode can be found in Fig. 5.3. Figure 5.2b shows that for energies below $\hbar\omega_{SP} = 2.3$ eV the positive-index mode (red curve) has the lowest attenuation and will therefore be dominant, whereas for energies above $\hbar\omega_{SP}$ the negative-index mode (blue curve) is dominant. Figure 5.2d shows the figure-of-merit, FOM $= |\beta/\beta''|$, of the two modes. The lowest attenuation constant $\omega(\beta'')$ for the negative-index mode is found at $\lambda_0 = 483$ nm, with a corresponding FOM of 8.3.

5.3 NIM Slab Refraction

Next, we analyze the collective response of the coupled coaxial waveguide array using the FDTD method. For the semi-infinite metamaterial slab calculations, the NIM is modelled in FDTD (Lumerical FDTD Solutions 6.0) as a single unit cell (Fig. 5.1b) embedded in air with Bloch boundary conditions along the in-plane direction. The

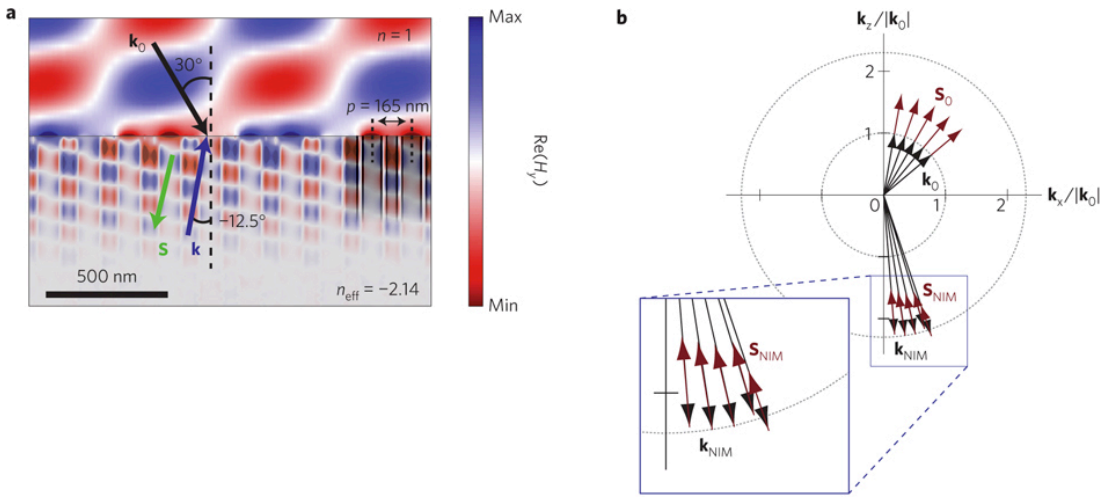

Figure 5.4: Metamaterial index. (a) Light at $\lambda_0 = 483$ nm is incident on a semi-infinite slab of single-layer negative index metamaterial at an angle of 30° from air. Shown is a time-snapshot of the magnetic field distribution $\mathrm{Re}(H_y)$, taken along the polarization plane. Arrows denote the direction of energy flow $\mathbf{S}$ and phase velocity $\mathbf{k}$. The coax center-to-center pitch is schematically indicated. (b) Constant-frequency surface plot at $\lambda_0 = 483$ nm, showing the relation between k_x and k_z for a semi-infinite metamaterial slab over a 50° range of incidence angles. The wavevector $\mathbf{k}$ and Poynting vector $\mathbf{S}$ data are derived from FDTD simulations.

structure is excited with a continuous plane wave source incident at an angle θ. The appropriate electromagnetic fields are recorded to reconstruct the refraction of phase (Fig. 5.4a) along the plane of incidence. The refraction of power is obtained by spatially averaging the steady state Poynting vector components inside the material along the plane of incidence. The steady state electromagnetic fields are obtained by calculating the systems impulse response to a plane wave source with a Gaussian frequency spectrum centred at the frequency of interest.

Figure 5.4a shows a time-snapshot of $\mathrm{Re}(H_y)$ inside a 165-nm-pitch coaxial waveguide array illuminated by a $\lambda_0 = 483$ nm p-polarized plane wave incident at 30°. At this pitch the waveguides are separated by 40 nm, corresponding to twice the radial skin depth ($\delta \sim 20$ nm) of an isolated coaxial waveguide mode into the Ag cladding. Phase fronts are observed to clearly refract in the negative direction, that is, to the same side of the interface normal. By following the phase fronts in time we observe backward phase propagation at an angle of $-12.5°$ with respect to the interface normal, as indicated in Fig. 5.4a by the blue arrow labelled **k**.

Using Snell's law and the wavevector refraction angle inside the material, we find that the metamaterial has an effective refractive index of $n_{eff} = -2.3$, close to the mode index found for an individual coaxial waveguide at this wavelength ($n_{mode} = -2.0$). Furthermore, the direction of energy flow **S** inside the NIM layer, depicted by the green arrow in Fig. 5.4a, is found to be antiparallel to the phase velocity – a signature of a true negative index material. Thus, at a separation of 40 nm, the waveguides are coupled just enough to allow both power and phase to refract negatively across the waveguide structures with antiparallel directions, while only perturbing the metamaterials effective index from that of a single coax by $\Delta_n = -0.3$. From the wavelength in the metamaterial and the exponential energy decay in the waveguides we find a metamaterial FOM of 8, equal to the FOM calculated for isolated coaxial structures.

By repeating this analysis for angles ranging from 10° to 50°, for both s- and p-polarized light at $\lambda_0 = 483$ nm, we find very similar results for the materials response, with n_{eff} varying between –2.1 and –2.4. The data for p-polarized light are

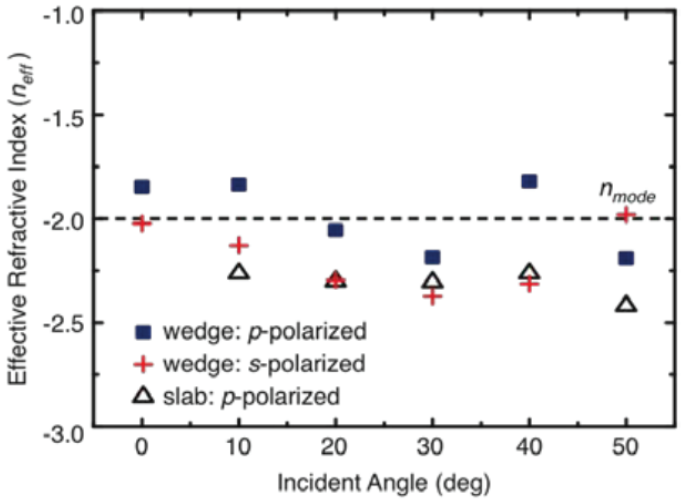

Figure 5.5: Summary of effective refractive index for varying angle of incidence. The metamaterial effective refractive index neff is plotted for $\lambda_0 = 483$ nm s- and p-polarized light incident at angles ranging from $0 - 50°$, derived from slab wave vector angles as in Fig. 5.4a, as well as from refraction angle measurements in wedge-shaped samples as in Fig. 5. The dashed line indicates the calculated mode index of a single coaxial waveguide.

summarized in Fig. 5.5. Such a small dependence of the index on polarization and angle-of-incidence has not been demonstrated in any other NIM reported so far. For example, Valentine et al. investigated only normal incidence excitation for a NIM operational in the near-infrared spectral region [129], whereas the negative-index mode in planar MDM structures can only be excited at off-normal incidence angles and at a specific polarization [34]. We note that simulations as in Fig. 5.4a show the semi-infinite NIM slab to reflect $\sim 35\%$ of the incident light, depending on angle, indicating that a significant fraction of light is coupled into the NIM layer. Notably, for oblique incidence, in addition to exciting the lowest order linearly polarized coaxial waveguide modes ($n = 1$), we also excite a minor contribution from the radially polarized mode ($n = 0$). However, this small modal overlap does not significantly change the material index response, as both modes have similar dispersion relations around the operation wavelength of $\lambda_0 = 483$ nm.

To demonstrate this, we show that in conducting a modal decomposition on a single coaxial waveguide structure excited at the maximum incidence angle of 50° with

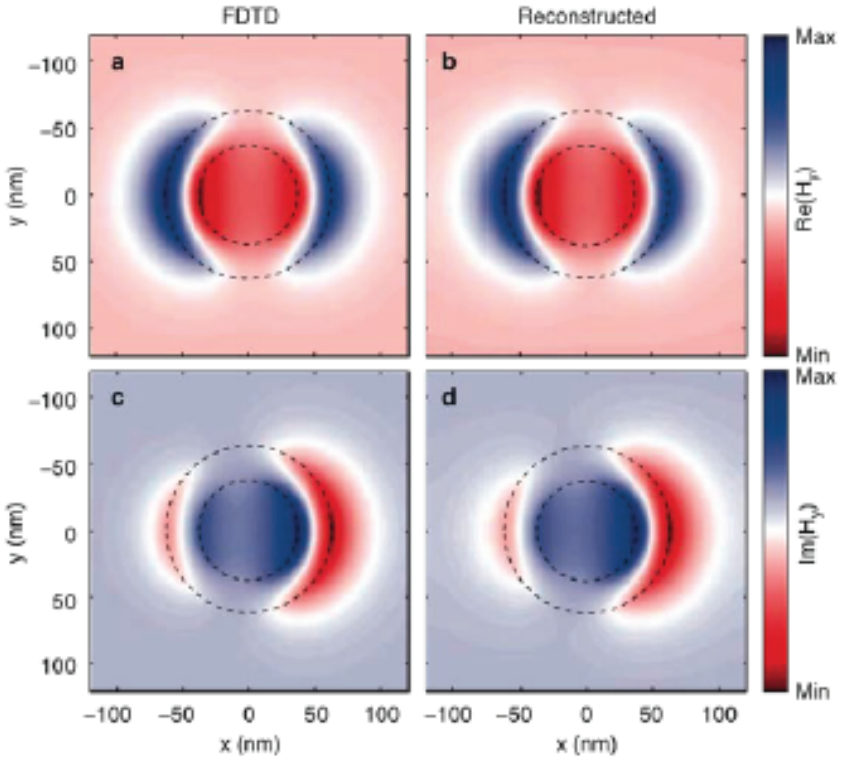

Figure 5.6: Modal reconstruction. A semi-infinite coaxial waveguide consisting of a 25-nm GaP annular channel with a 75-nm inner diameter embedded in Ag is illuminated from air with λ_0= 483 nm light at a 30° angle-of-incidence. Plotted are the real and imaginary parts of H_y. The two panels on the left (a, c) show the mode excited inside the waveguide, and the two right-side panels (b, d) show the mode reconstructed from a superposition of 87% n=1 mode and 13% n=0 mode, where n refers to the azimuthal dependence of the fields.

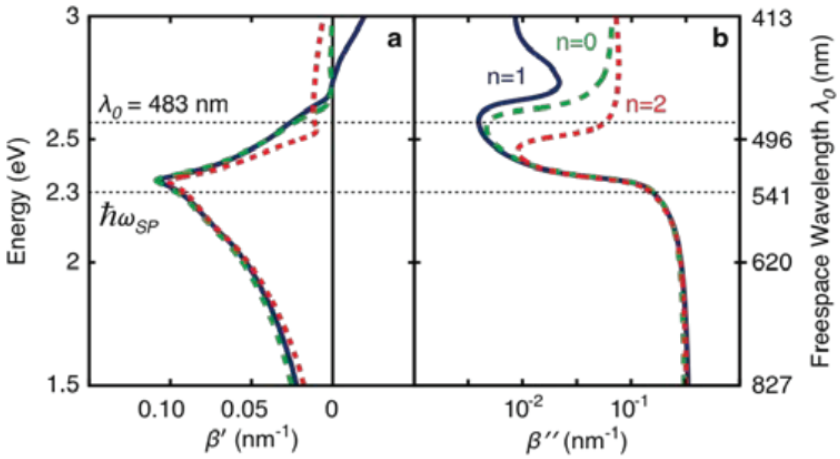

Figure 5.7: Coaxial waveguide mode dispersion relations. The coaxial waveguide consists of an infinitely long 25-nm GaP annular channel with a 75-nm inner diameter embedded in Ag. Plotted are the n = 0, 1, and 2 dispersion relations, where n refers to the azimuthal dependence of the fields in the waveguide, described by the harmonic function $e^{in\psi}$ of order n. Energy is plotted versus β' in (a), β' in (b). The Ag/GaP planar surface plasmon energy at $\hbar\omega_{SP}$= 2.3 eV (λ_0 = 540 nm) and the target negative-index operation wavelength (λ_0 = 483 nm) are indicated by black dashed horizontal lines.

λ_0=483 nm light, we find that the resulting excited waveguide mode is composed of 87% n=1 mode and only 13% n=0 mode, where n refers to the azimuthal dependence of the fields in the waveguide described by the harmonic function $e^{in\psi}$ of order n. The accuracy of the modal decomposition can be seen in Fig. 5.6, where the measured and reconstructed waveguide modes are plotted with 99.97% modal overlap. Furthermore, in looking at the dispersion relations of these two modes, we find that their complex indices are similar around the operation wavelength λ_0 = 483 nm (Fig. 5.7), thus explaining why the minor contribution from the n = 0 mode does not significantly affect the overall functionality of the predominantly n = 1 mode material at off-normal angles of incidence. For reference, H_y field cross-sections of the three lowest order modes (n = 0, 1, 2) are plotted in Fig. 5.8.

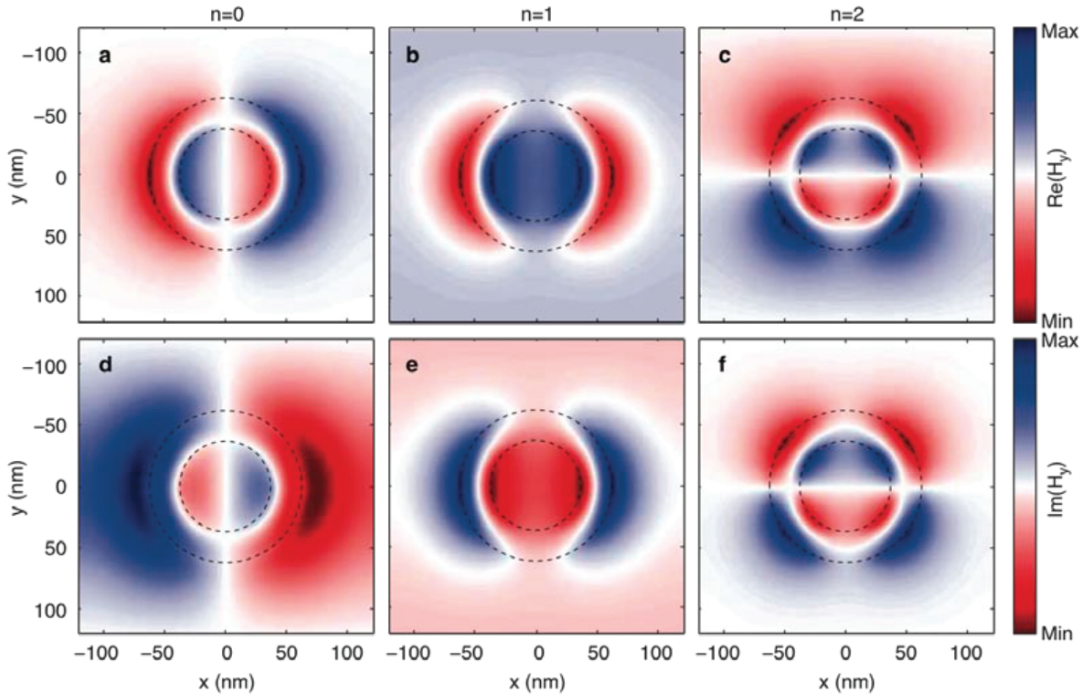

Figure 5.8: Coaxial waveguide eigenmodes. The coaxial waveguide consists of an infinitely long 25-nm GaP annular channel with a 75-nm inner diameter embedded in Ag. Plotted are the real (a, b, c) and imaginary (d, e, f) parts of the H_y field components of the $n = 0$ (a, d), 1 (b, e), and 2 (c, f) modes at $\lambda_0 = 483$ nm, where n refers to the azimuthal dependence of the fields.

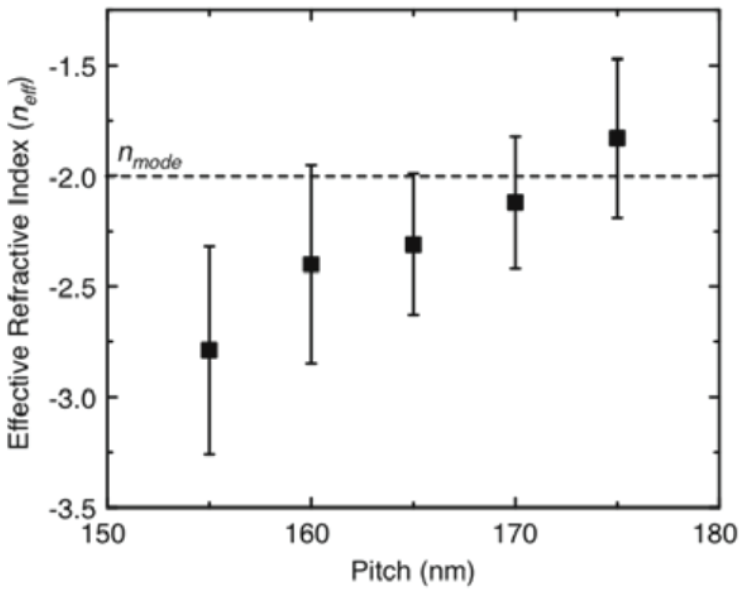

Figure 5.9: Effective refractive index as a function of pitch. The effective refractive index neff derived from wave vector angles is plotted as a function of pitch for λ_0 = 483 nm p-polarized light incident at 30° on a variable pitch waveguide array slab similar to that shown in Fig. 5.4a. The dashed line indicates the calculated mode index of a single coaxial waveguide.

5.4 Pitch Dependence

To further investigate the effect of coupling between coaxial waveguides, we also performed calculations for which the pitch is set to p = 330 nm, corresponding to a waveguide separation of ∼10 skin depths. As expected, we find that for the same excitation conditions of λ_0 = 483 nm light incident at 30°, the waveguides are effectively decoupled, with power flowing straight down the coaxial waveguides. Indeed, by calculating the average Poynting vector inside the layer, we establish that no net horizontal power flow occurs for this configuration. Thus, in the limiting case of completely decoupled waveguides, we obtain a uniaxial anisotropic medium with power flowing straight down the one-dimensional waveguides, irrespective of angle of incidence. In that case, we cannot assign an effective materials index in terms of either power or phase, but rather assign a local effective mode index that is characteristic of an isolated waveguide mode.

However, as the array pitch is decreased, the waveguides begin to couple in such a way that both power and phase are able to propagate across the waveguide array. We find that coupling is easily achieved for the negative-index mode, because its strongly delocalized field distribution, which resides primarily in the metal, allows neighbouring structures to easily couple (see Fig. 5.2a insets and Fig. 5.8). At a waveguide separation of roughly twice the mode skin depth of a single coaxial waveguide mode into the surrounding Ag, we find not only that power and phase are antiparallel, but also that they refract with an effective index close to the mode index of the constituent waveguides (Fig. 5.9). By varying the incidence angle, the array response is found to be isotropic within a $\pm 50^\circ$ angular range (Fig. 5.5).

This level of isotropy can be observed in Fig. 5.4b, which shows the constant-frequency surface formed by the wavevector **k** and Poynting vector **S** data derived from FDTD simulations. The figure clearly illustrates that both phase and power are antiparallel within a $\pm 50^\circ$ range of incidence angles (corresponding to a $\pm 20^\circ$ angular range inside the material).

5.5 Parameter Retrieval

To confirm the validity of assigning an effective index to the coupled coaxial waveguide structure, we used FDTD to perform a parameter retrieval procedure on a 100-nm-thick NIM slab (Fig. 5.1a) over the 400 – 500 nm spectral range.

The parameter retrieval is calculated using FDTD by exciting a 100-nm-thick NIM slab embedded in air with a broadband plane wave source ranging from $\lambda_0 =$ 400 to 500 nm at normal incidence. The steady state field distributions are recorded, and the complex reflection r and transmission t coefficients are calculated by taking the ratios $r = E_r/E_0$ and $t = E_t/E_0$, where E_0 is the electric field amplitude of the incident wave and E_r and E_t are the reflected and transmitted electric field amplitudes, respectively. Standard inverted reflection and transmission parameter equations found in literature[123, 82] are used to relate r and t to the layers effective impedance z_{eff} and index n_{eff}. The effective permittivity ϵ_{eff} and permeability μ_{eff}

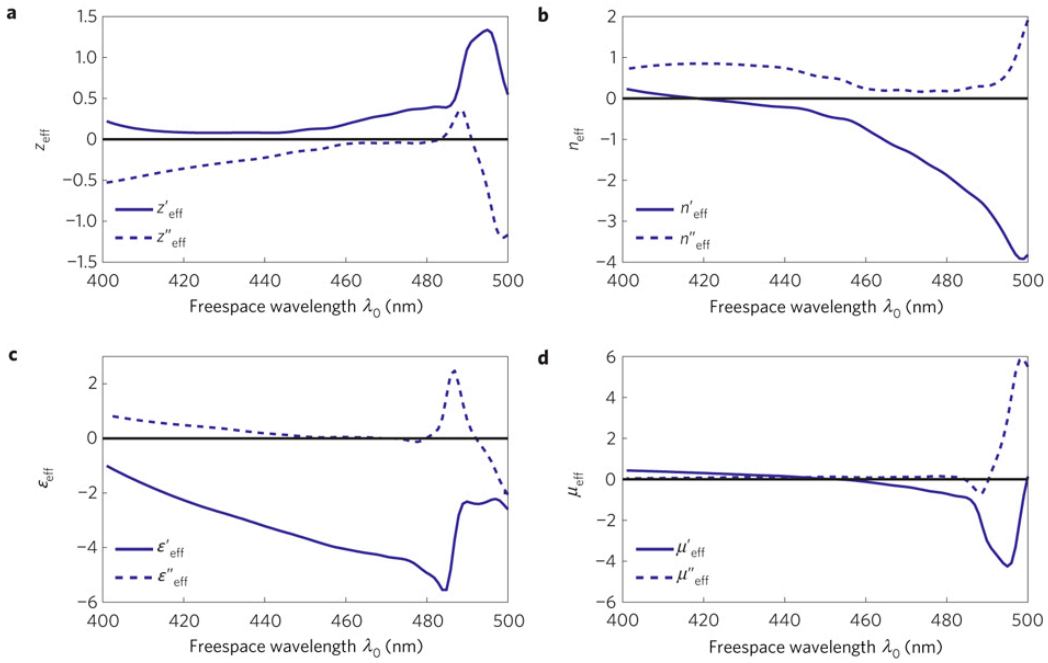

Figure 5.10: NIM effective parameters. Effective parameters are calculated for a 100-nm-thick NIM slab excited at normal incidence over the 400–500 nm spectral range. (ad) The real ($'$) and imaginary ($''$) parts of the retrieved effective relative impedance z_{eff} (a), index n_{eff} (b), relative permittivity ϵ_{eff} (c) and relative permeability μ_{eff} (d).

are calculated through the relations $\epsilon = n/z$ and $\mu = nz$.

Figure 5.10 shows the resulting curves corresponding to the effective relative impedance z_{eff}, index n_{eff}, relative permittivity ϵ_{eff}, and relative permeability μ_{eff} of the coupled coaxial NIM structure, with ($'$) and ($''$) denoting the parameters' real and imaginary parts, respectively. The extracted effective index curve (Fig. 5.10b) is found to closely resemble the mode index dispersion of a single coaxial waveguide structure (Fig. 5.2c) with n'_{eff} going from positive to negative values at $\lambda_0 \sim$420 nm, with increasing wavelength. At $\lambda_0 = 483$ nm, we obtain a retrieved effective index of $n_{eff} = 2.1 + i0.2$, corresponding to a FOM$\sim$10 that is consistent with the single coaxial waveguide FOM$\sim$8. For the retrieved effective relative permittivity ϵ_{eff} (Fig. 5.10c), we observe a material with $\epsilon'_{eff} < 0$ over the entire simulated spectral region, whereas for the effective relative permeability μ_{eff} (Fig. 5.10d), we get a material that is diamagnetic with$\mu'_{eff} < 0$ over the 450–500nm spectral range. Thus,

we confirm that the coupled coaxial waveguide NIM structure has a double-negative index [25] composed of simultaneously negative real parts of the permittivity and permeability over the 450–500nm spectral range.

5.6 Wedge Refraction

To further corroborate our results, we have simulated the Snell-Descartes refraction of a ∼300-nm-thick wedged-shaped metamaterial slab cut at a 3° angle. The NIM wedge is modelled in FDTD as a ∼300-nm-thick metamaterial-slab cut at a 3° angle. The structure is excited with a continuous wave source centered at the desired excitation frequency using a ∼1-μm-wide hollow metallic waveguide oriented perpendicular to the metamaterial's input plane. The appropriate electromagnetic fields are recorded to reconstruct the refraction of phase (Fig. 5.11a) along the plane of incidence. The structure is also excited from free space with a ∼1.5-μm spot size Gaussian beam. Using the steady state field distribution at the output side of the wedge, a near-to-far-field transformation is performed to determine the refracted-beam profile at a distance of 10 μm behind the exit side of the structure.

Figure 5.11a depicts a time snapshot of the steady state Re(H_x) field distribution along the plane of refraction for λ_0=483nm s-polarized light at normal incidence. Figure 5.11a shows that light refracts negatively at the angled side of the prism, exiting the structure at an angle of $-6°$ with respect to the surface normal. Figure 5.11b shows a polar plot of the refracted light projected into the far field. Using Snells law and the observed negative refraction angle, we derive a refractive index for the metamaterial slab of n_{eff}=–1.8, in agreement with the effective index derived from the observed wavevector inside the semi-infinite slab.

To demonstrate the insensitivity of the metamaterial-index to incidence angle, we also simulated the refraction of off-normal incident light through the 3° wedge. Figure 5.11c and d show the simulation results for λ_0=483nm radiation incident at 30°. The green arrows in Fig. 5.11c indicate the direction of the Poynting vector for the incident and refracted beams. In this case the beam is refracted at an angle of

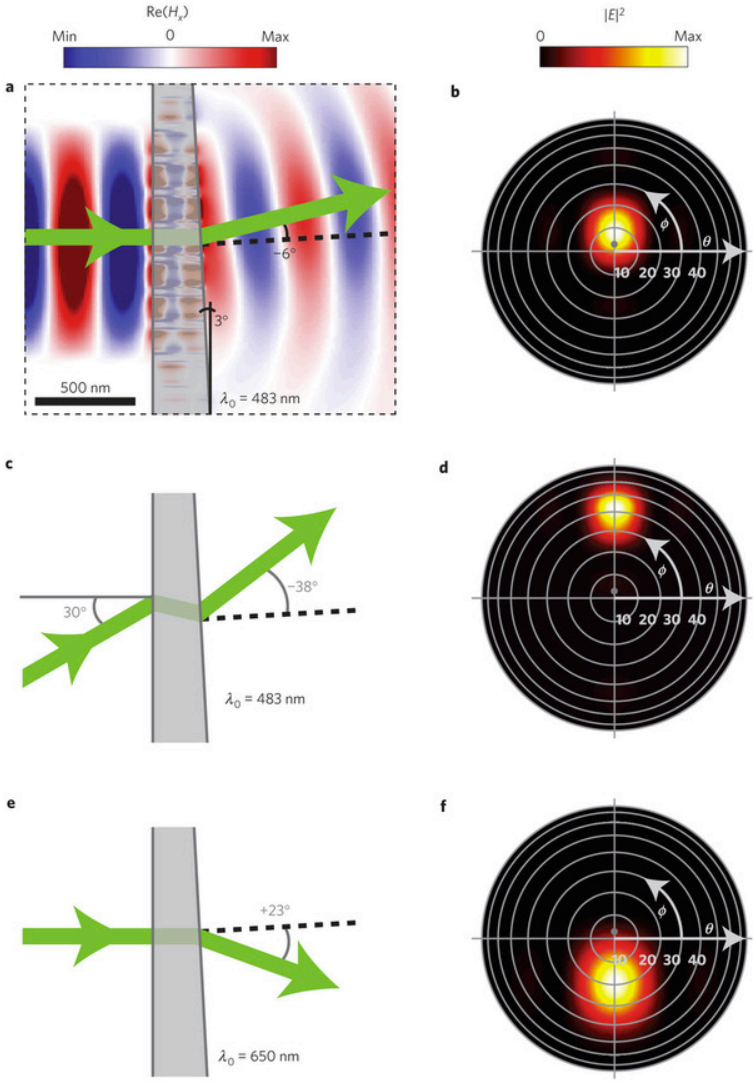

Figure 5.11: Wedge refraction. (af) A ∼300-nm-thick metamaterial slab is illuminated from the left at normal (a,b,e,f) and 30° off-normal incidence (c,d). The right side of the slab is cut at a 3° angle to allow refraction (black dashed line indicates the surface normal). The wavelength of incident light is 483 nm (ad) and 650 nm (e,f). The three panels on the left (a,c,e) depict the calculated power flow (green arrows), and the three corresponding right-side panels (b,d,f) show the steady-state electric field intensity in a polar plot, monitored at a distance of 10 μm behind the exit side of the slab. The output plane surface normal is indicated on the polar plots by a grey dot. In (a) we also plot the Re(H_x) field distribution along the plane of refraction.

$-38°$ with respect to the surface normal, corresponding to an effective index n_{eff}=–2.2, again consistent with the effective index found for the wedge excited at normal incidence. By varying the angle-of-incidence from normal incidence up to 50° for both *s*- and *p*-polarized light, we find consistent refractive indices ranging from –1.8 to –2.4. These data are summarized in Supplementary Fig. 5.5.

To illustrate the metamaterial's tunability with wavelength, we study the refraction of λ_0=650nm radiation, for which the mode index dispersion of a single waveguide element (Fig. 5.2a) shows a positive index (n_{mode}=8.5). Indeed, as Fig. 5.11e and f show, the beam is now refracted to the opposite side of the interface normal, at an angle of 23°, corresponding to a positive effective index of n_{eff}=7.4. We attribute the difference between the metamaterial effective index and isolated waveguide mode index to the possible excitation of higher-order waveguide modes. Thus, by illuminating the structure with frequencies either above or below the Ag/GaP surface plasmon resonance, we can excite both positive and negative refractive indices within the same metamaterial.

5.7 Conclusion

Realization of the metamaterial structure reported here involves the challenge of fabricating high-aspect-ratio nanoscale Ag channels. However, we have shown that 50-nm-wide coaxial apertures with aspect ratios >10 can readily be fabricated using focused ion beam milling [31]. For large-scale fabrication, a more tractable approach would be to use electron beam lithography in combination with high-aspect-ratio reactive ion etching. We also note that observation of the negative-index response requires only a modest total material thickness, that is, thick enough for a single waveguide to support the negative index waveguide mode. This can, for instance, be seen in our wedge simulations (for example, Fig. 5.11a) where the wedge thickness is only ∼300nm, and the material's negative index response is clearly observed. At λ_0=483nm for an index of $n = -2$, a minimum thickness of ∼120nm is required, corresponding to a modest coaxial channel aspect ratio of 4.

Part II

Hole Array Color Filters

Chapter 6

Plasmonic Color Filters for CMOS Image Sensor Applications

Abstract: *Having seen how coaxial plasmonic waveguides can serve as building blocks for metamaterials, in this section we explore how plasmonic hole arrays can serve as efficient color filtering elements for imaging application. This chapter discusses the optical properties of plasmonic hole arrays as they apply to requirements for plasmonic color filters designed for state-of-the-art Si CMOS image sensors. The hole arrays are composed of hexagonally packed subwavelength sized holes on a 150-nm Al film designed to operate at the primary colors of red, green, and blue. Hole array plasmonic filters show peak transmission in the* $40-50\%$ *range for large (*$> 5\times5\mu m^2$*) size filters and maintain their filtering function for pixel sizes as small as* $\sim 1\times1\mu m^2$*, albeit at a cost in transmission efficiency. Hole array filters are found to be robust with respect to spatial crosstalk between pixels within our detection limit, and they preserve their filtering function in arrays containing random defects. Analysis of hole array filter transmittance and crosstalk suggests that nearest neighbor hole-hole interactions rather than long-range interactions play the dominant role in the transmission properties of plasmonic hole array filters. We verify this via a simple nearest neighbor model that correctly predicts the hole array transmission efficiency as a function of the number of holes.*

6.1 Introduction

Metal films with subwavelength-size periodic hole arrays are known to act as optical filters, owing to the interference of surface plasmon polaritons (SPPs) between adjacent holes. Unlike current on-chip organic color filters, plasmonic filters have the advantage of high color-tunability with only a single perforated metal layer and do not suffer from performance degradation after ultraviolet (UV) radiation. However, for successful on-chip implementation, the plasmonic filter must also be compatible with contemporary image sensors featuring small ($\sim 1 \times 1 \mu m^2$) pixel size, and have a large functional array size, spatial color-crosstalk effects, and robustness against random defects.

Extensive studies of enhanced transmission through optically thick metal films perforated with arrays of subwavelength-size holes have been performed by numerous groups [39, 56, 6, 7, 71, 96, 102]. The enhanced transmission observed in hole arrays is explained by excitation of surface plasmon polaritons (SPPs) at the metal surface that are launched at each hole and interfered among adjacent holes. Transmission enhancements are found to occur at central frequencies determined by the physical size of the holes and the thickness of the metal film, as well as the optical properties of metal and dielectric medium [71, 96]. With reported peak transmission efficiencies of more than 30% at visible wavelengths, hole array films have received much attention for their potential to serve as spectral filters for imaging applications [69, 22, 62].

In contemporary image sensor technologies such as CCDs and CMOS image sensors (CISs), color sensitivity is added to photodetective pixels by equipping them with on-chip color filters (OCCFs), typically composed of organic dyes corresponding to the three primary colors. However, organic dye filters are not durable at high temperatures or under long-duration ultraviolet irradiation exposure and cannot be made much thinner than several hundred nanometers, due to the low absorption coefficient of the dye material. Furthermore, fabrication of each of the three organic dye filters for a red/green/blue or cyan/magenta/yellow color scheme requires carefully aligned lithography of each type of color filter over the entire photodiode array, thus mak-

ing impractical the fabrication of multicolor imaging devices with both large array formats and very small pixels.

On the other hand, the transmission properties of plasmonic metal filters composed of periodic hole arrays are mainly defined by their physical structure. This means that by simply changing the hole size, shape, and separation, the transmission spectra of the hole array can easily be controlled with only a single thin metal layer. Owing to this feature, plasmonic color filters are very cost competitive, especially for multicolor imaging applications. Furthermore, plasmonic filters have many other advantages over conventional filters, such as higher reliability under high temperature, humidity, and long-term UV radiation exposure conditions.

More recently, a plasmonic hole array color filter was integrated with a CMOS image sensor, demonstrating filtering functionality in the visible [21, 23]. However, works such as this have mostly focused on the transmission properties of large size filters, with little emphasis given to other important filter performance aspects necessary for state-of-the art image sensor applications, such as the filter transmission dependence on array size, spatial color-crosstalk, and robustness against defects. In this work, we report on such optical properties as they pertain to various configurations of hexagonal arrays of subwavelength holes fabricated in 150-nm-thick Al films suitable for image sensor integration.

6.2 Experimental

In our experiments, hole array filter fabrication was done using a 30 kV, 10 pA focused ion beam (FIB) to mill the desired hole array patterns in a 150-nm-thick Al film evaporated over 1 in. square quartz substrates. In order to characterize hole array transmission as a function of hole diameter and period in the visible wavelength range, we fabricated isolated square filters composed of 16×16 hexagonally aligned holes with period (p) ranging from 220 to 500 nm in 40-nm steps and diameter (d) ranging from 80 to 280 nm in 20-nm steps (see Figure 6.2).

To analyze the transmission dependence on filter size, we designed filters that were

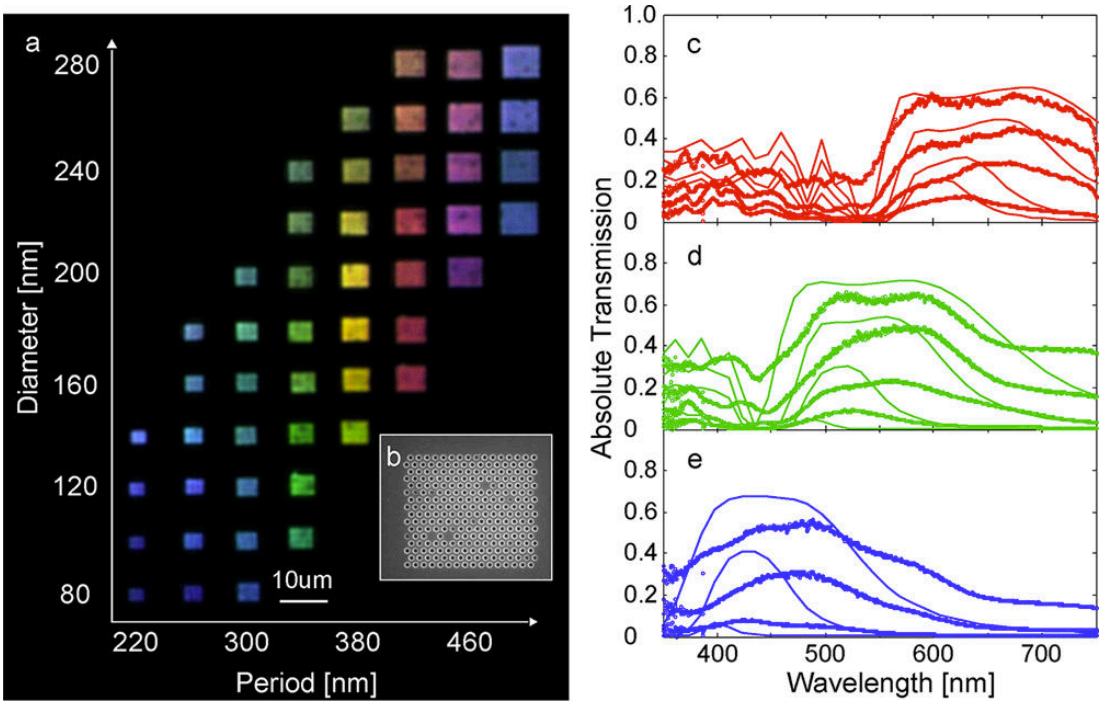

Figure 6.1: (a) Back illuminated microscope images of the fabricated hole array filters. Each filter consists of 16×16 hexagonally packed hole arrays. The vertical axis corresponds to hole diameter, ranging from 80 to 280 nm in 20-nm steps, and the horizontal axis corresponds to hole period, ranging from 220 to 500 nm in 40-nm steps. The white bar on the lower part of the images corresponds to a 10-μm scale. Inset (b) shows a SEM image of a representative hole array filter consisting of hexagonally aligned 16×16 holes with $p = 420$ nm and $d = 240$ nm. Measured hole array spectra for filters optimized to transmit (c) red ($p = 420$ nm, $d = 160280$ nm), (d) green ($p = 340$ nm, $d = 120240$ nm), and (e) blue light ($p = 260$ nm, $d = 100180$ nm) are plotted in dotted lines, and the simulated spectra are plotted in solid lines. Each plot of three color spectra is in steps of 40 nm in hole diameter.

optimized to operate at the three primary colors of (R) red (p = 420 nm, d = 240 nm), (G) green (p = 340 nm, d = 180 nm), and (B) blue (p = 260 nm,d = 140 nm), and fabricated four different hole array filter sizes of each corresponding to 1.2×1.2 μm^2-, 2.4×2.4 μm^2-, 5×5 μm^2-, and 10×10 μm^2-size filters. To measure the effect of spatial color crosstalk between different color filters, we fabricated adjacent color filters adjoined with zero separation, and to determine the effect of random defects we fabricated 10×10 μm^2-size green filters with a density of intentionally designed random defects ranging in area fraction from 1 to 50%.

Open windows with no metal film with the same physical aperture as the square hole array filters were fabricated in order to normalize filter absolute transmission efficiency. After milling the desired hole array configurations, the sample was covered with 200 nm of spin-coated Honeywell 312B spin-on-glass (SOG).

Spectral transmission measurements were performed on a Zeiss Axio Observer inverted microscope coupled to a grating spectrometer and nitrogen-cooled CCD system. The sample was illuminated with a halogen lamp filtered by a temperature conversion filter that gave a sunlike blackbody emission (color temperature of 5500 K) incident light. The microscope field diaphragm and aperture stop were both closed in order to have collimated incident light. All filter spectra were measured with a spectrometer utilizing a 100×1340-pixel liquid nitrogen cooled CCD detector with sensitivity in the 300–800-nm wavelength range. The transmission spectrum of each hole array filter was divided by the spectrum of the corresponding-size open-window in order to measure the absolute transmission of each filter. To check measurement system stability during characterization, the open window spectra were measured every hour.

Figure 6.2a shows a back-illuminated microscope image of the fabricated hole array filters consisting of arrays of 16 × 16 holes for each, with hole period ranging from 220 to 500 nm from left to right and hole diameter ranging from 80 to 280 nm from bottom to top. The smallest 200 nm period filters correspond to ∼3.5×3.0μm^2-size filters, and the largest 500-nm period filters to ∼8.0×6.9μm^2. The inset image (Fig. 6.2b) shows a scanning electron micrograph (SEM) image of a representative

filter with $p = 420$ nm and $d = 240$ nm.

The measured transmission spectra for the hole array periodicities corresponding to red ($p = 420$ nm), green ($p = 340$ nm), and blue ($p = 260$ nm) are plotted in Fig. 6.2c,d, respectively, with each panel illustrating the spectra for different diameters. From the measured spectra, indicated as the color dotted lines, we see that the peak transmission position shifts to longer wavelength with increasing hole period and that the peak transmission efficiency increases with increasing hole diameter. The maximum filter transmission is found to be in the range of 40–50% in the visible spectrum with a spectral full-width half-maximum (FWHM) of ∼150 nm.

6.3 Comparing with FDTD

To validate the measured spectra, we simulated the fabricated filter transmission response using three-dimensional full-field electromagnetic simulations. The simulation model consists of a SiO_2 matrix with an embedded 150-nm-thick Al film perforated with hexagonally aligned holes of the same pitch and diameter as those fabricated. The optical response of the resulting hole array film is excited with a broadband planewave source in the 300–900-nm wavelength range launched at normal incidence. The red solid lines in Fig. 6.2c,d plot the resulting simulated transmission spectra. In general, the simulated profiles show good agreement with the measured spectra, with the only notable differences being that the measured spectra have relatively broader profiles, which can be attributed to fabrication imperfections (e.g., tapered hole profiles) or surface roughness of the Al film.

Although the fabricated color filters reveal vivid colors and have fairly good peak transmission efficiency over the visible spectrum, there is some undesirable transmission in the blue spectral range for the red color filter designs. As evident from Fig. 6.2, the red color filters ($p = 420$ – 500 nm, $d \geq 200$ nm), optimized for transmission in the 600 – 800 nm wavelength range, demonstrate some spectral crosstalk with the blue part of the spectrum ($\lambda_0 < 500$ nm wavelengths). Owing to this undesirable transmission, the red color filters appear slightly pink, magenta, and violet as illus-

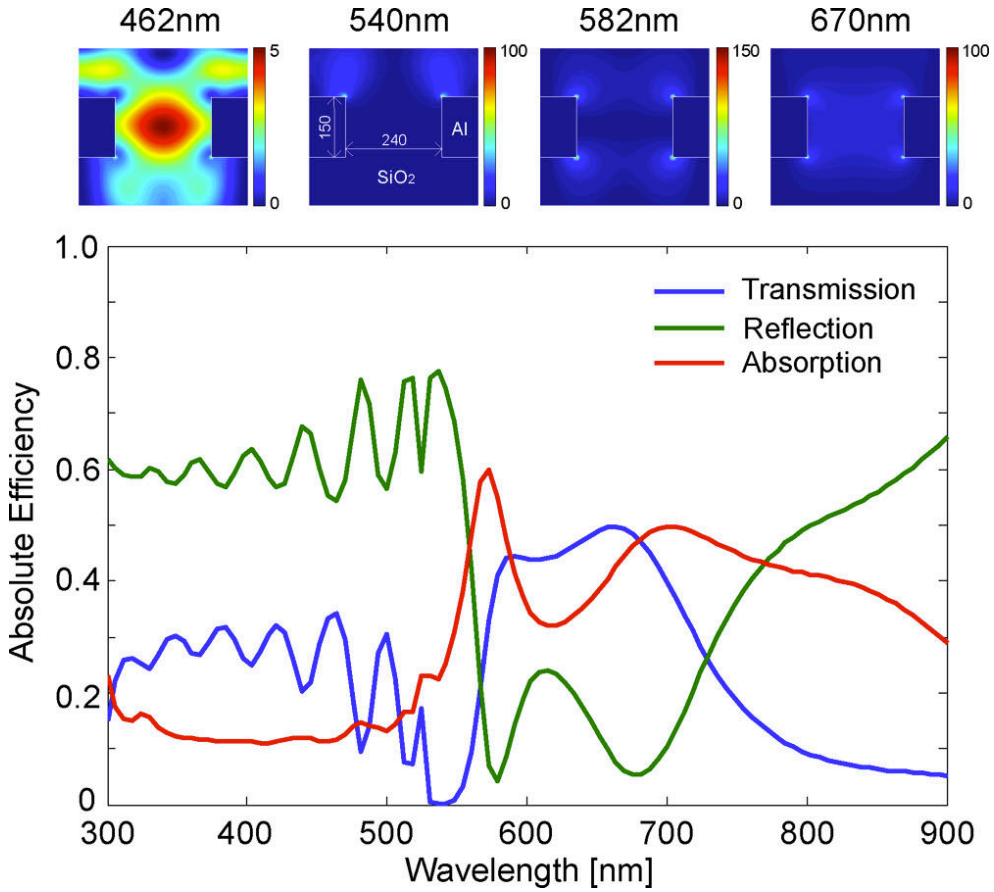

Figure 6.2: The simulated spectra of the hole array filter with p = 420 nm and d = 240 nm, which is optimized to transmit red color. The top four panels plot the electric field distribution at the wavelengths of interest along the diameter of the holes, parallel to the polarization of the plane wave used to excite the structure.

trated in Fig. 6.2a. It is worth noting that although having perfect RGB filters would be most ideal for imaging applications, spectral crosstalk such as this can easily be corrected using signal processing.

Nevertheless, to better understand the origin of the spectral crosstalk, we used full-field simulations to spectrally resolved electric field distribution along the diameter of the holes, parallel to the polarization of the incident planewave. Figure 6.3 shows the simulated transmission profile of the red (R) filter along with the cross-sectional electric field distributions at various wavelengths of interest. Consistent with our measurements, the simulated spectrum shows two broad transmission bands separated by a null at 540 nm that corresponds to the reciprocal lattice vector of the hexagonally

aligned hole array structure [96].

From the electric field intensity maps, we see that the transmission peaks at 582 and 670 nm of the longer wavelength transmission band correspond to strongly localized electric field distributions at the top and bottom of the hole, whereas for the transmission null at 540 nm, the localized electric field exists only at the top of the hole. This is consistent with the interpretation that there is an intrinsic $\pi/2$ phase shift resulting from the SPP emission and recapture process at the exit side of the film, leading to a minimum in the transmission at wavelengths corresponding to the reciprocal lattice vector of the array [96].

On the other hand, whereas the electric field distribution at 582 and 670 nm show strongly localized field distributions at the top and bottom of the holes, the field distribution at 462 nm shows a high electric field intensity distribution inside the hole itself, suggesting that the source of transmission at shorter wavelengths is dominated by the photonic modes supported by the structure. We note that one way to reduce the excess blue transmission for the red filters may be to suppress these photonic modes via the use of coaxial structures rather than holes, formed by adding concentric metallic cylinders inside the hole. However, the absolute transmission efficiency of coaxial structures has been reported to be only a few percent [17, 120].

6.4 Size Dependence

Next, we investigate the effect of filter size on the transmission properties of hole array filters, an important feature in determining the smallest pixel size that can be used for imaging applications. The heavy lines in Fig. 6.4 indicate the transmission spectra of the three primary color (RGB) hole array filters fabricated at four different filter sizes, corresponding to squares of side-lengths equal to approximately 10 μm (Fig. 6.4a), 5 μm (Fig. 6.4b), 2.4 μm (Fig. 6.4c), and 1.2 μm (Fig. 6.4d). It is interesting to note that regardless of size, all the filters maintain their filtering functionality down to the 1 μm-size filters, although at a cost in transmission efficiency. Both the 10-μm and 5-μm-size filters have similar peak transmission efficiencies, with blue peaking at 28%

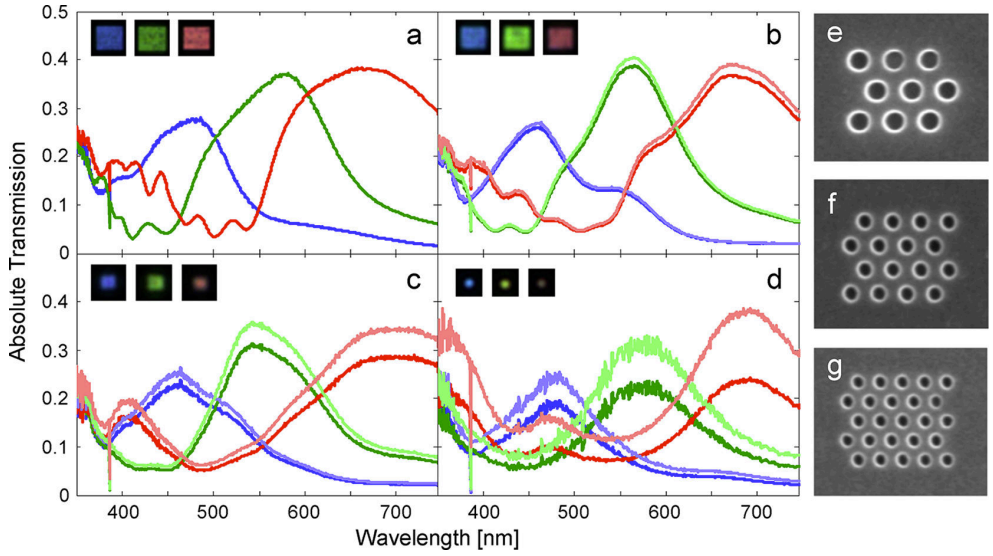

Figure 6.3: Transmission spectra of the hole array filters optimized to red (p = 420 nm, d = 240 nm), green (p = 340 nm, d = 180 nm), and blue (p = 260 nm, d = 140 nm) of different filter sizes of (a) 10 μm-, (b) 5 μm-, (c) 2.4 μm-, and (d) 1.2 μm-squared size filters. The insets of (a-d) panels show the back illuminated microscope images of the filter with the field of views corresponding to 13-μm-, 6.5-μm-, 5.0-μm-, and 4.0-μm-squared. (e)-(f) SEM images are the 1.2-μm-size filters, RGB, respectively.

and green and red both at 38%. Transmission drops by $\sim$ 25% for the 2.4-μm-size filters relative to 10-μm-size filters and by $\sim$ 40% for the 1.2-μm-size filters.

6.5 Spatial Crosstalk

To investigate the effects of spatial crosstalk of colors between adjacent pixels, we measure the spectra of three different sets of color filter pairs with zero separation, consisting of B/R, G/B, and R/G color combinations, with each color filter consisting of a 10 $\times$ 10 μm^2 array. Figure 6.5 a shows a representative SEM image of the boundary between two such hole array filters, and Fig. 6.5b-d show back illuminated images of the filter pairs. Figure 6.5e illustrates the measured sliced spectra for the B/R-filter combination, with each spectrum corresponding to a 1-μm-wide integrated cross-sectional area, taken perpendicular to the filter pair boundary at the positions indicated by the yellow ticks in Fig. 6.5b. Figure 6.5g,i show the corresponding spectra

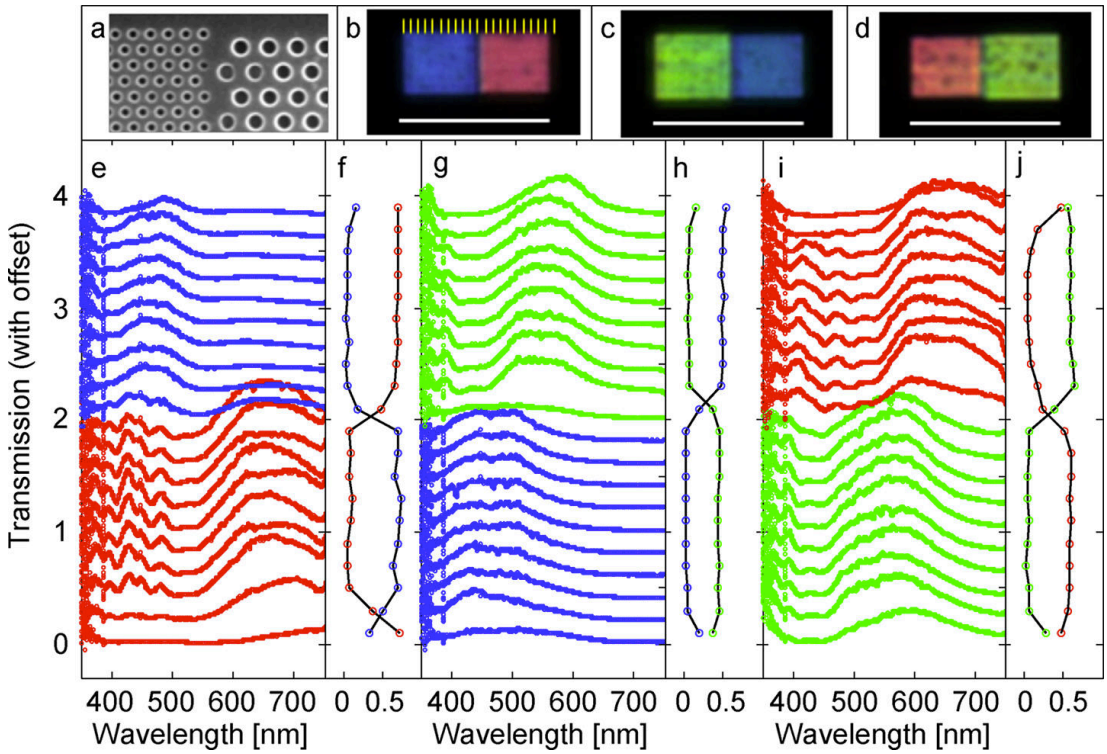

Figure 6.4: Sliced transmission spectra of color filter pairs with zero separation. (a) A representative SEM image of boundary between two such filters. (b-d) Back-illuminated microscope images of the color filter pairs taken with a color CCD camera. The white lines correspond to 20-μm scale bars. The spectra of each color filter pair are taken over 1-μm-wide areas centered at the positions indicated by the yellow ticks in (b). Sliced spectra are shown for (e) blue/red, (g) green/blue, and (i) red/green filter pairs. The panels next to the sliced spectra in (f), (h), and (j) plot the correlation of each measured spectra with respect to the averaged spectrum of colors in the filter pair.

for the other two filter pair color combinations.

The panel next to each sliced spectra, for example, Fig. 6.5f, plots the correlation function Δ_i, which measures the difference between the measured spectrum, $T_i(\lambda)$, where i runs from 1 to 20 over the slice number, and the averaged spectrum of each filter color $\bar{T}_{R,G,B}(\lambda)$, obtained by averaging the middle eight spectra of each color filter. The correlation function is then defined by Eq. 6.1, where α_i is a normalizing constant for each measured spectrum, allowing Δ_i to take on values from 0 to 1, depending on the correlation of the measured spectra, with respect to the averaged spectrum.

$$\Delta_i = \alpha_i \int_{\lambda_{max}=700\text{ nm}}^{\lambda_{min}=400\text{ nm}} (T_i(\lambda) - \bar{T}_{R,G,B}(\lambda))d\lambda \tag{6.1}$$

In Figs. 6.5f,h,j, the correlation functions undergo an inversion in going from one color filter to another. From these plots, we can estimate that the spatial color crosstalk between filters is as small as 1 μm. This length contains not only the contribution of the diffraction limit but also some defocus from the measurement settings, and hence it is possible that the crosstalk between filters is almost comparable to our detection limit. It is worth pointing out that although there is zero separation between the filters, Fig. 6.5b-d clearly show dark lines between filter pairs, evidence of the small spatial color crosstalk between filters.

6.6 Random Defects

Because fabrication imperfections are inevitable, it is important to characterize the sensitivity of filter transmission and spectral shape to random defects. To evaluate the robustness of the hole array filter design, we measured the transmission of 32 $\times$ 32 hole green filters with randomly positioned missing holes at a density of 0, 1, 2, 5, 10, 20, and 50%. The resulting spectra are indicated in Fig. 6.6a, from which we can see that the filter transmission efficiency and shape is unaffected for random defect densities $\leqslant$ 5%, but filter transmission monotonically decreases for random defect densities $\geqslant$ 10%. However, if we normalize each spectrum by its peak transmission, as shown in Fig. 6.6b, we find that all the spectra have nearly identical line shapes, independent of filter defect density, suggesting that the random defects only affect the filter transmission efficiency and not the spectral shape.

To better understand the transmission efficiency degradation with increased defect density, we show the relative peak transmission efficiency versus random defect density in Fig. 6.6c, from which it is clear that the dependence is not simply linear, indicating that it is not simply a geometrical effect. To gain insight into the optical processes that govern this trend, we introduce a simple analytic model to explain hole array

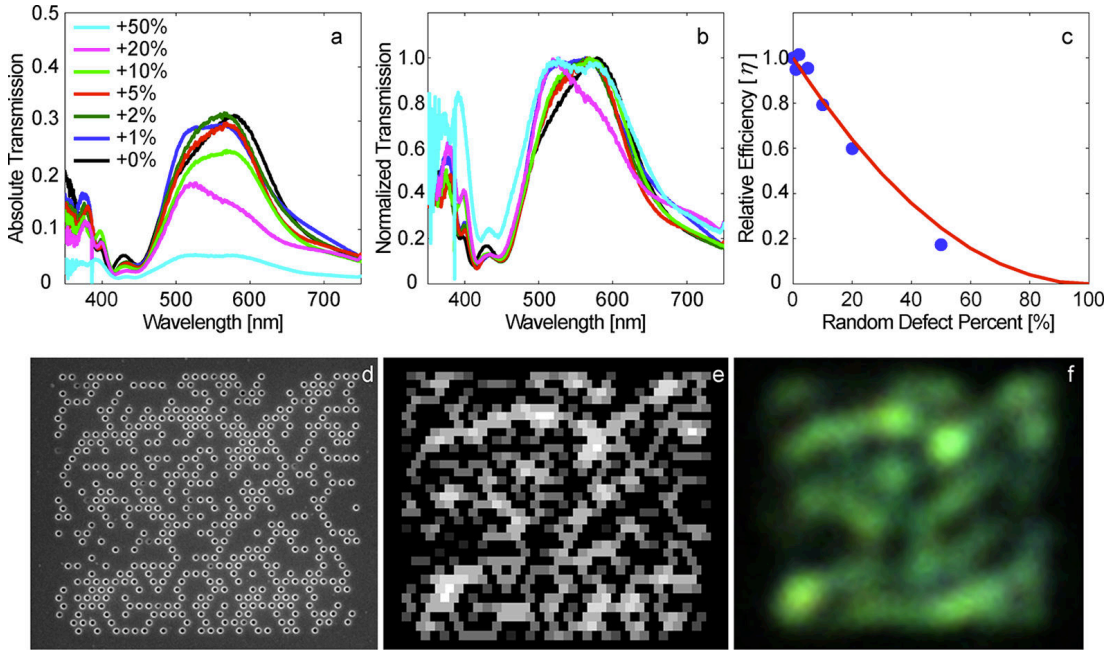

Figure 6.5: (a) Transmission spectra of green hole array filter consisting of 32 $\times$ 32 holes with $p = 340$ nm and $d = 180$ nm for different random defect (missing hole) density. (b) Normalized transmission spectra from (a). (c) Plot of the relative peak efficiency versus defect rate. The data plotted by blue dots corresponds to the transmission efficiency of a green filter with defect density ranging from 0 to 50%, and the red line is the analytically estimated degradation curve. (d) A SEM image of green filter with 50% defect density. (e) An analytically-calculated transmission intensity map of the filter from (d). (f) A back-illuminated microscope image corresponding to the filter from (d).

transmission efficiency based on nearest neighbor interactions.

6.7 Nearest Neighbor Model

Because the hole array layout is three-fold symmetric, the filter transmission efficiency should not depend on the polarization of the incident light [62]. Thus, any given hole in the array, characterized by coordinates $x = i$,$y = j$, will have six equally distanced and thus equally contributing nearest neighbor sites, labeled $A-F$. Using this model, the transmission efficiency $\eta_{i,j}$ of each site in the array can be calculated by simply averaging the contribution from its nearest neighbors, as given by Eq. 6.2, where δ_k represents delta functions which will take on its value only if there is a hole at the nearest neighbor site, k.

$$\eta_{i,j} = \frac{1}{6}\sum_{k=A}^{F}\delta_k \tag{6.2}$$

Using this model, the transmission efficiency of a given hole in the array will vary from 0 to 1, depending on the number of holes surrounding it. The relative transmission efficiency of a given filter, η, can then be calculated by summing over the efficiency of each hole in the array and normalizing it by the efficiency of a defect-free array of the same size, $\eta_0 = 6$ (number of holes in array); see Eq. 6.3.

$$\eta = \frac{\sum_{i,j\in\text{array}}\eta_{i,j}}{6\ (\text{number of holes in array})} \tag{6.3}$$

To check the accuracy of the model, we plot the predicted relative transmission efficiency of a 32 $\times$ 32 hole green filter as a function of random defect density in Fig. 6.6c. From the correlation between the measured data and predicted curve, we see that the nearest-neighbor model correctly captures the degradation in efficiency with the increasing number in random defects, suggesting that nearest neighbors indeed play the most dominant role in the transmission efficiency of hole arrays.

This nearest neighbor transmission model can also be used to reconstruct the spatial transmission distribution of a hole array filter with random defects. Figure

5d shows a SEM image corresponding to 32 × 32 hole green filter with 50% random defects. To predict the spatial transmission efficiency of this filter, we take the SEM image and apply the nearest neighbor transmission model to each site in the array. The resulting modeled transmission images are plotted in Fig. 6.6e, which shows good qualitative agreement with the measured back illuminated image of the filter, Fig. 6.6f.

6.8 Size-Corrected Transmission Efficiencies

Using this model, we can also explain the effect of filter size on the transmission properties of finite-size defect-free hole array filters. For example, for a 3×3 filter (corresponding SEM image shown in Fig. 6.4e), owing to the limited number of holes in the filter, only the center hole has six nearest neighbors and thus the maximum transmission. The other eight holes at the filter edge will have fewer than six neighbors, bringing down the average of the entire filter to 60%, as given by Eq. 6.2. However, for larger $> 24 \times 24$ hole filters, the transmission efficiencies go up to $> 95\%$ because almost all the holes in the array have six nearest neighbors.

Using these relative transmission efficiencies, we can calculate the size-corrected transmission efficiency between two size filters of the same color by simply dividing their relative transmission efficiencies. To check this, we calculate and plot the size-corrected transmission profiles of the measured finite-size filters in Fig. 3. The light lines in Fig. 3b-d show the size-corrected spectrum of the 5-, 2.4-, and 1.2-μm size filters as compared to the 10-μm-size filter. After the correction, we see that all four filters have fairly constant transmission efficiency, suggesting the model is also accurate in explaining finite size effects.

6.9 Conclusion

In conclusion, plasmonic hole array color filters are found to be a great alternative to conventional on-chip dielectric filters due to their tunability across the visible spec-

trum with only a single layer of perforated metal, especially for multicolor imaging applications. In this work, we show that because their scattering dynamic is only determined by nearest neighbor interactions, the transmission properties of hole array filters are extremely robust with respect to array size, random defects, and spatial crosstalk from neighboring filters of different color. The hole array's ability to filter light with only a small number of holes, combined with their small spatial crosstalk, are attractive features for 2D image sensor applications requiring densely packed filtering elements. Furthermore, their robustness at filtering functionality against random defects makes them especially tractable for industrial mass-production. However, for further developments of plasmonic filter technology to industrial application, additional studies, especially an actual filter implementation to a CMOS image sensor, are required to demonstrate their feasibility, reliability, and advantages over conventional technologies.

Chapter 7

Color Imaging via Integrated Plasmonic Color Filters on a CMOS Image Sensor

Abstract: *In Chapter 6 we explored several filter performance aspects necessary for state-of-the art image sensor applications, such as filter transmission dependence on array size, spatial color-crosstalk, and robustness against defects. In this chapter we use these findings to integrate a plasmonic hole array color filter onto a CMOS IS, demonstrating the first realization of high-resolution full-color plasmonic imaging. Plasmonic hole arrays have been the subject of enormous scientific interest over the last 15 years, since the first observation of extraordinary light transmission [39, 56, 6]. Since then, the physics of hole array spectral filtering has been intensely debated [71, 96, 7, 80, 107], motivated by color imaging applications [19, 68]. Recently, advances in plasmonic hole array filter design and performance, as well as CMOS integration, have been described [22, 143, 14, 23, 21], but to date, no functioning camera has been reported. In this chapter, I demonstrate the imaging characteristics of a 360×320 pixel color camera by integrating a plasmonic color filter array with a commercial black and white 1/2.8 inch CMOS image sensor, and taking high resolution full color images with the integrated image sensor. The color filters, consisting of 5.6×5.6-μm^2 size color pixels in a 150-nm Al film, were chosen to correspond to the RGB primary colors and arranged in a Bayer mosaic layout. The color images are taken with C-mount lenses coupled to the image sensor with focal lengths ranging from 6-*

50 mm, all showing good color fidelity with a 6-color-averaged (Red, Green, Blue, Yellow, Magenta, Cyan) CIE ΔE 2000 = 16.6–19.3, after a white balance and color matrix correction is applied to the raw image over the wide range of f-numbers ranging from 1.8 – 16. The integrated peak filter transmission efficiencies are measured to be in the 50% range, with a FWHM of 200 nm for all three RGB filters in good agreement with the spectral response of isolated unmounted color filters [22, 143, 69]. We also investigate light coupling from hole array filters to CMOS pixels using full wave electromagnetic simulations.

7.1 Introduction

In contemporary Si-based image sensor technologies such as charge-couple devices (CCDs) and complementary metal-oxide semiconductor (CMOS) image sensors, color sensitivity is added to photo detective pixels by equipping them with on-chip color filters, composed of organic dye-based absorption filters [88]. However, organic dye filters are not durable at high temperatures or under long exposure to ultraviolet (UV) radiation [61] and cannot be made much thinner than a few hundred nanometers due to the low absorption coefficient of the dye material. Furthermore, on-chip color filter implementation using organic dye filters requires carefully aligned lithography steps for each type of color filter over the entire photodiode array, thus making their fabrication costly and highly impractical for multi-color and hyperspectral imaging devices composed of more than the three primary or complementary colors.

It is well known that plasmonic hole arrays in thin metal films can be engineered as optical band-pass filters, owing to the interference of surface plasmons (SPs) between adjacent holes. Unlike current on-chip organic color filters, plasmonic filters have the advantage of being highly tunable across the visible spectrum and require only a single perforated metal layer to fabricate many colors. Plasmonic hole array color filters have recently been integrated with a CMOS image sensor, demonstrating filter viability in the visible [143], but full color imaging using the plasmonic color filter technology platform has not be reported. In Chapter 6, we investigated several filter

performance aspects necessary for state-of-the art image sensor applications, such as filter transmission dependence on array size, spatial color-crosstalk, and robustness against defects [23, 21].

In this chapter, we investigate the transmission and imaging characteristics of CMOS plasmonic color imaging. A commercial black and white 1/2.8-inch CMOS image sensor is integrated with a 360×320 pixel plasmonic color filter array composed of 5.6×5.6 μm^2-size RGB color filters in a Bayer mosaic layout (Fig. 7.1a). Full color images are taken by coupling the image sensor to C-mount lenses with focal lengths ranging from 6-50 mm, all showing good color fidelity with the 6-color-averaged (Red, Green, Blue, Yellow, Magenta, Cyan) CIE ΔE 2000 = 16.6–19.3 after, a white balance and color matrix correction is applied to the raw image over the wide range of f-numbers ranging from 1.8 – 16.

7.2 Filter Design

Following well-known principles for spectral transmission of hole array filters [22, 143, 62], we used a 150-nm-thick Al film perforated with hexagonally packed holes with period (p) and diameter (d) equal to p=420nm, d=240nm for red (R), p=340nm, d=180nm for green (G) and p=260nm, d=140nm for blue (B). For the color filter layout, we used the Bayer-pattern color filter array layout, which consists of a 2×2 color unit cell with two green filters (Gb, Gr) in the diagonal positions (the lower case letter following the G corresponds to color that is next to the green filter), and blue (B) and red (R) in the off-diagonal positions (Fig. 7.1b). Each individual color filter was designed with the size of 5.6×5.6 μm^2, which is exactly twice the pixel size of the CMOS image sensor, in order to account for alignment errors in the integration (see Fig. 7.3). E-beam lithography and lift-off were used to stitch 180×160 Bayer unit cells onto a quartz substrate (see Fig. 7.2), resulting in a 360×320 pixel plasmonic color filter array of dimensions 2016×1792 μm^2 (Figs. 7.1c-d). Here we see 11.2-μm-width grid lines separating 40×40 filter blocks (corresponding to 224×224 μm^2), which were created during the fabrication to both prevent overexposure of the peripheral region of

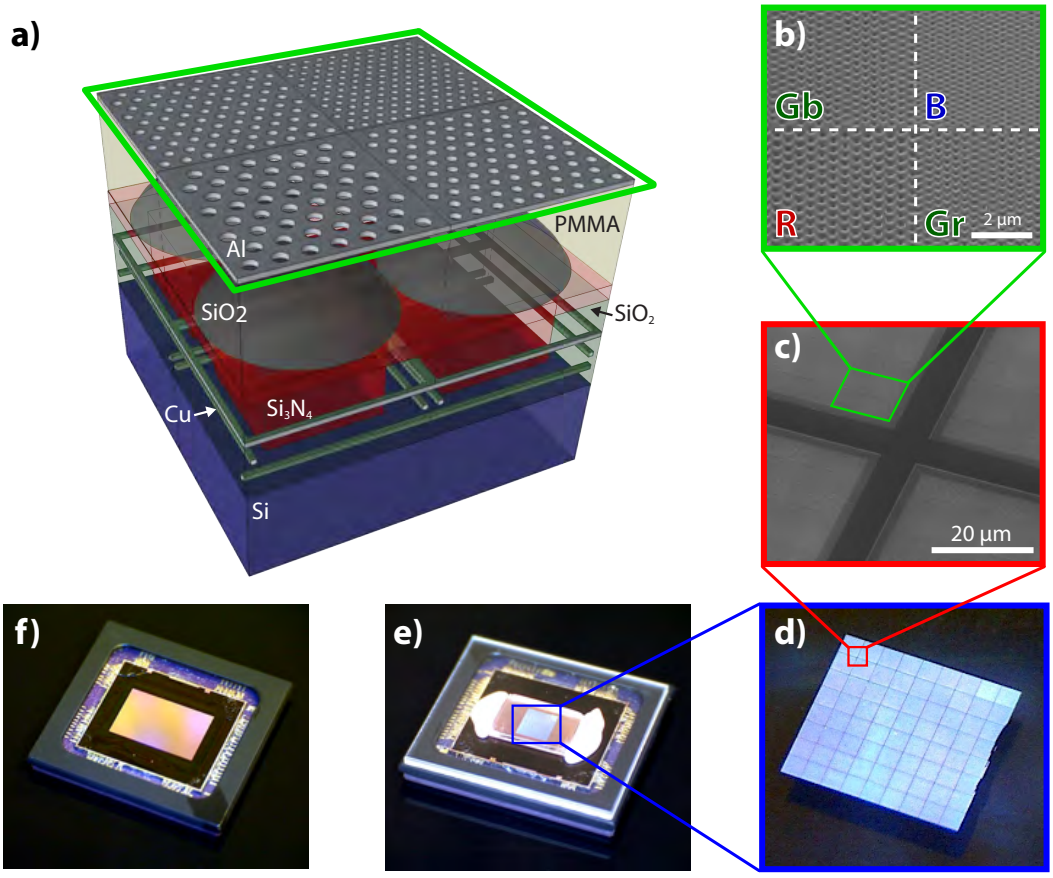

Figure 7.1: Integrated CMOS image sensor with hole array filter. a) Schematic of integrated front-side illumination CMOS image sensor with RGB plasmonic hole array filters in Bayer layout. b) Scanning electron micrograph of RGB hole array filters in Bayer layout. c) Scanning electron micrograph of 11.2μm alignment grid lines separating 40×40 filter blocks. d) Image of full 360×320 pixel (2016×1792 μm^2) plasmonic hole array filter array on quartz. Each square on the image corresponds to a 40×40 filter block (224m×224μm^2) separated by 11.2μm alignment grid lines. e) Image of integrated CMOS image sensor with plasmonic hole array filter. The white on the far edges of the filter corresponds to electronic grade putty used to hold the filter in place after alignment. f) Image of CMOS image sensor before integration.

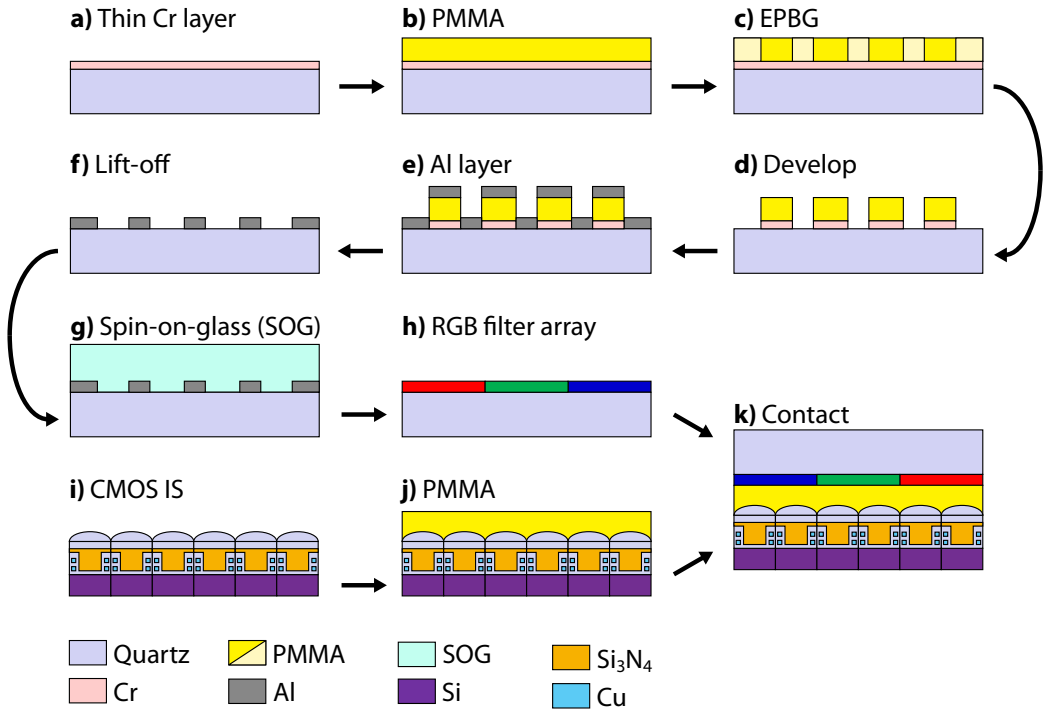

Figure 7.2: Integrated CMOS image sensor with hole array filter. a) Schematic of integrated front-side illumination CMOS image sensor with RGB plasmonic hole array filters in Bayer layout. b) Scanning electron micrograph of RGB hole array filters in Bayer layout. c) Scanning electron micrograph of 11.2μm alignment grid lines separating 40×40 filter blocks. d) Image of full 360×320 pixel (2016×1792 μm^2) plasmonic hole array filter array on quartz. Each square on the image corresponds to a 40×40 filter block (224m×224μm^2) separated by 11.2μm alignment grid lines. e) Image of integrated CMOS image sensor with plasmonic hole array filter. The white on the far edges of the filter corresponds to electronic grade putty used to hold the filter in place after alignment. f) Image of CMOS image sensor before integration.

each block during electron beam lithography and to serve as guide lines for alignment with the CMOS image sensor pixel array.

7.3 Fabrication and Integration

Fabrication of the plasmonic hole array filter was done using electron beam lithography and lift-off (see Fig. 7.2). A thick Cr layer was used to reduce charging of the quartz substrate during patterning (Fig. 7.2a) and a 150 nm Al layer was used for

the final hole array filter metal layer (Fig. 7.2e). After developing, a 300-nm-thick layer of spin-on-glass (SOG) was used to infill the hole array filters (Fig. 7.2g). Once fabricated, the integration was done by directly contacting the color filter array onto the CMOS image sensor (Fig. 7.2k), using PMMA to first planarize the microlenses of the image sensor (Fig. 7.2j).

For the integration, we used a front-side-illumination black and white CMOS image sensor composed of 1920×1200 2.8×2.8 μm^2 size pixels, corresponding to a 5376×3360 μm^2 effective pixel area (Fig. 7.1). The integration was done by directly contacting the color filter array onto the CMOS image sensor (see Fig. 7.2). As shown in Fig. 7.1e, due to the difference in size between the plasmonic color filter and the CMOS chip, only the center 1/3 of the horizontal area and 3/5 of the vertical area of the CMOS image sensor was equipped with plasmonic color filter functionality.

7.4 Alignment

Alignment of the hole array filter array with the CMOS image sensor was done by hand under a microscope. Since each individual color in the 360×320 RGB filter array was designed to be exactly twice the pixel size of the CMOS image sensor (see Fig. 7.3a), small translational misalignments were easily corrected by selecting either the even or odd pixels in each direction of the CMOS image sensor array (see Fig. 7.3b). Note that rotational misalignments (Fig. 7.3c) cannot be corrected using this scheme, since the rotational alignment error is not constant throughout the chip. After aligning the filter array as best as possible, electronic grade putty was used to hold the filter in place.

To check the alignment, an image was taken of a gray wall, and the color uniformity was checked for the different parity set of pixels after demosaicing the image but before applying white balance, i.e., before equalizing the RGB value readouts. Thus, the gray color of the wall will show up as green since the green pixels have a larger signal than the red and blue pixels before they are equalized by the white balance transformation (R,G,B = 1.7, 1.0, 1.3). The images for the different parity set of pixels are show

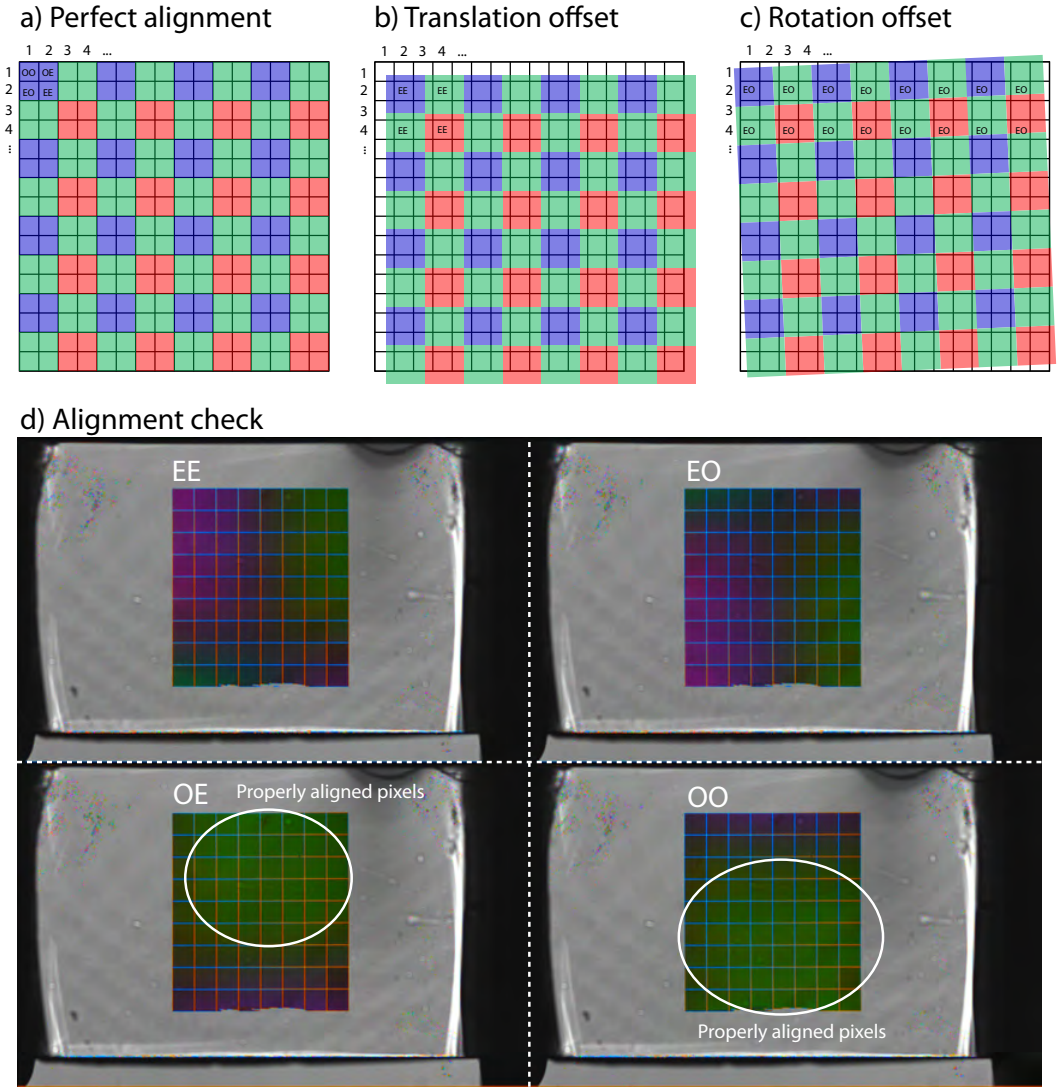

Figure 7.3: Alignment of plasmonic hole array filter with CMOS image sensor. The lined grid represents the pixel array of the CMOS image sensor, and the transparent RGB box grid represents the plasmonic hole array color filter array in Bayer layout. The pixels are labeled using matrix convention (i,j) with i coming from the horizontal number axis and j coming from the vertical number axis, and the double letters inside of the grid refer to the parity of the pixel label, with E for even and O for odd. Pixel and filter array are shown with a) perfect alignment, b) translation offset, and c) rotational offset. d) Images of the difference parity set of pixel readouts, even-even (EE), even-odd (EO), odd-even (OE), and odd-odd (OO), after demosaicing the gray wall image taken with the integrated CMOS image sensor with aligned filter

in Fig. 7.3d, with the even-even (EE), even-odd (EO), odd-even (OE), and odd-odd (OO) pixel readouts showing a spatial color map which varies from green to magenta. The green areas correspond to pixels that are entirely covered by a single color filter in the RGB filter array (see e.g., Fig. 7.3b), and the magenta areas correspond to pixels that must be sitting predominantly at the boundaries between different color filters (see e.g., Fig. 7.3c).

7.5 Transmission Measurements

The optical efficiency of the color filter design was assessed with spectral transmission measurements of isolated 22.4×22.4-μm^2-size RGB plasmonic hole array filters. The spectral transmission measurements of isolated unmounted 22.4×22.4-μm^2-size RGB plasmonic hole array filters were performed on an inverted microscope coupled to a grating spectrometer and liquid nitrogen cooled CCD system. The sample was illuminated with a collimated halogen lamp filtered by a temperature conversion filter that gave a sun-like blackbody emission (color temperature of 5500 K). All filter spectra were measured with a spectrometer utilizing a 100×1340 pixel liquid nitrogen cooled CCD detector with sensitivity in the 300-800 nm wavelength range. The transmission spectrum of each hole array filter was divided by the spectrum of an open window of the corresponding size in order to measure the absolute transmission of each filter.

The resulting spectra, plotted in Fig. 7.4a, show all three RGB filter designs having peak efficiencies in the 50–60% range with FWHM in the 150–200 nm range, consistent with the transmission data extracted from full field electromagnetic simulations using finite-difference time-domain calculations for unmounted plasmonic color filters of corresponding dimensions, embedded in a quartz matrix illuminated at normal incidence (Fig. 2c).

Direct comparison of the transmission efficiencies between the unmounted (Fig. 7.4a) and CMOS integrated (Fig. 7.4b) plasmonic color filters gives a quantitative measurement of how well the plasmonic color filters are integrated onto the CMOS image sen-

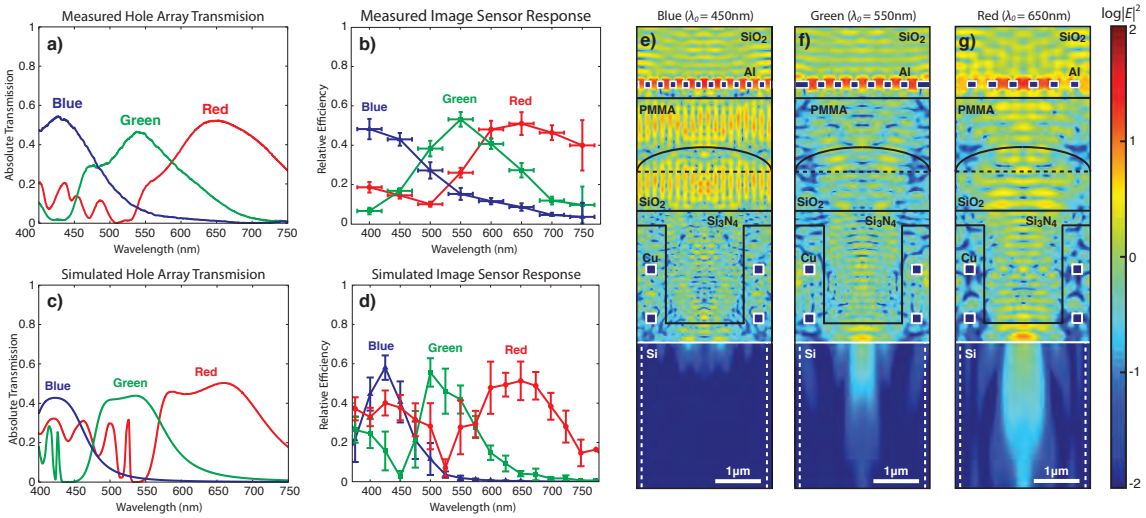

Figure 7.4: Integrated CMOS image sensor response. a) Measured and c) simulated spectral response of unmounted RGB plasmonic hole array filters. b) Measured and d) simulated relative efficiency of integrated CMOS image sensor with RGB plasmonic hole array filters. The horizontal error bars correspond to the spectral width of the band-bass filter used for the measurements, and the vertical error bars correspond to the averaged data. Simulation field map cross-sections taken at the center of the pixel and at the center transmission wavelengths for the e) blue ($\lambda_0 = 450$nm), f) green ($\lambda_0 = 550$nm), and g) red ($\lambda_0 = 650$nm) hole array color filters integrated with the CMOS image sensor.

sor. In comparing these two data sets, we see that the integrated peak transmission efficiencies are in the 50% range, which is only slightly lower than those of the unmounted color filters, indicating that although the direct contact integration scheme is not optimal, it does not degrade the efficiency significantly. Because the color filter was integrated by simply by pressing the filter and image sensor into intimate contact, we expected that there could be a low refractive gap between the bottom of the plasmonic filter and the top surface of the image sensor that could reduce the light coupling efficiency. However we find from full field electromagnetic simulations of the integrated device that the experimentally measured absolute light coupling efficiencies shown in Fig. 7.4c are in the same range as those simulated under perfect light coupling conditions in intimate mechanical contact (Fig. 7.4d), indicating that the integration is nearly ideal.

7.6 Transmission Simulations

The transmission of isolated RGB filters was simulated in FDTD (Lumerical Solutions 7.0) with a single unit cell of the hexagonal Al hole array lattice embedded in quartz with Bloch boundary conditions in the in-plane directions and PML boundary conditions in the excitation direction. Complex optical constants for Al and SiO_2 are taken from tabulated data [97]. For normal incidence simulations, the structure was excited with a broadband planewave source, and the steady-state electromagnetic fields were recorded on the opposite side of the structure. The transmission of the structure was calculated as the time average of the Poynting vector normalized by the source. For angled illumination, it was done similarly to the normal incidence simulations, expect that care was given to the angles imposed by the Bloch boundary condition on all the wavelengths.

The steady state field response of the integrated structure (Fig. 7.1a) was simulated using FDTD. Complex optical constants for Al, SiO2, Si_3N_4, and Si were taken from tabulated data[97], PMMA was modeled as SiO_2, and Cu as a perfect electric conductor (PEC) in order to reduce the simulation time. The structure was illumi-

nated with a broadband planewave, and the steady-state electromagnetic fields were recorded at the center cross-section of the structure (Figs. 7.1e-g) to observe the field distribution response.

The resulting simulated steady state intensity field distributions of the three filters at their center wavelengths are shown in Figs. 7.4e-g, showing that a significant factor in the high light coupling efficiency comes from the nitride waveguide, which directs the light into the active region of the Si image sensor pixel. We note also that, as expected, the simulations indicate that blue light absorption occurs in the Si pixel near-surface region, while green light absorption occurs at a depth of approximately 1μm, and red light absorption occurs at a depth of approximately 3μm below the Si surface. Importantly, the simulations also indicate that the integrated plasmonic filter and image sensor pixel exhibits negligible crosstalk in the form of light scattering into adjacent pixels after light is coupled through the plasmonic filter.

7.7 Color Imaging

Having verified the plasmonic color filter transmission efficiency as integrated on the CMOS image sensor, we demonstrate color camera performance by taking full color images using a 12.5 mm lens and a 5.6 f-number, corresponding to a half-aperture angle of 5°. In Fig. 7.5a, we display a representative raw image taken under these conditions of a 24-color Macbeth chart positioned in a scene. In Fig. 7.5f we plot the signal of the pixels indicated by the dashed yellow line in Fig. 7.5a, which spans across the gray color patches on the Macbeth color chart. At this point, each pixel has 10 bit data, ranging from 0-1023, and we subtract the optical black (OPB) signal from the image, which corresponds to a dark current signal offset, as indicated in Fig. 7.5f.

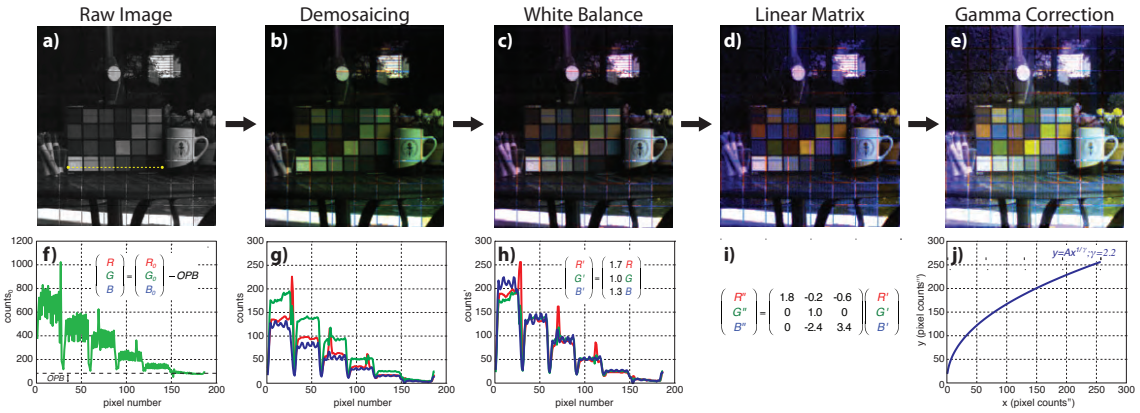

Figure 7.5: Image reconstruction process. a) Raw image of 24-color Macbeth color chart positioned in a scene taken with integrated CMOS image sensor with RGB plasmonic hole array filter. Image after b) demosaicing, c) white balancing, d) linear matrix correcting, and e) gamma correcting the image. The yellow dashed line in a) shows the pixel signal that is being plotted in f-h), corresponding to the images above them. i) Linear matrix used on image after applying white balance to remove color cross talk. j) Gamma transformation used to convert the image sensors linear response to brightness to the logarithmic response of the human eye.

7.8 Image Reconstruction

Since the active pixels on the CMOS image sensor are filtered by a Bayer color filter array, each pixel only has intensity information of one of the three primary colors. To reconstruct the full-color image, a bilinear demosaicing algorithm is used to interpolate the set RGB values for each pixel from its neighbors. For example, the red value of a non-red pixel is computed as the average of the two or four adjacent red pixels, and similarly for blue and green. The resulting bitmap image after demosaicing is shown in Fig. 7.5b, with corresponding RGB signal levels (ranging from 0-255) shown in Fig. 7.5g.

After demosaicing, the image is white balanced by equalizing the RGB signal levels of the gray patches on the Macbeth color chart (Fig. 7.5c,h). Next, we apply a linear matrix correction to correct for the filter's spectral color crosstalk (Fig. 7.5d,i). Here we see that the Red pixels are applied a transformation that subtracts Green and Blue values from it, $R'' = 1.8R' - 0.2G' - 0.6B'$, as expected, since the Red

pixels experience the most color crosstalk as seen from the spectra plotted in Fig. 2. Similarly, the Blue pixels are subtracted a nearly equal amount of the Green spectra from itself, $B'' = -2.4G' + 3.4B'$, in order to shift the original Blue filter's spectral response further into the blue. However, we leave the Green filter spectra untouched, $G'' = 1.0G'$, since subtracting any amount of Red or Blue from the Green would significantly reduce its counts due to their large spectral overlaps (see Fig. 2). In order to realize a pure Green spectra with a much narrower FWHM and smaller linear matrix cross-terms, we would need to incorporate slightly smaller filter hole diameters or apply novel filtering structures having higher transmission efficiency with narrower FWHM than those of hole array filters[120].

After applying the linear matrix pixel transformation, a gamma correction (Fig. 7.5j) is applied to convert the image sensor's linear response to brightness into the logarithmic response of the human eye. The result is the natural color image shown in Fig. 7.5e. Here we see the 11.2-μm alignment grid lines, which contain 40 color pixels in between them along the two normal directions.

7.9 Measuring the Color Quality

The color quality of the image can be measured using the CIE ΔE 2000 metric [116], which measures the color difference between the reference color on a Macbeth color chart and what the actual color is in the signal-processed image (Fig. 7.5e). Via this metric, the higher the ΔE, the more noticeable the color difference is to the human eye, and $\Delta E = 1$ is regarded as the just noticeable difference. Using established color code standards [116], the measured CIE ΔE of the integrated CMOS image sensor increases from 3.8 for Blue, to 10.2 for Green, and 28.6 for Red, reflecting the fact that the hole array filter design is efficient at filtering short (blue) wavelengths, but has increasing color crosstalk from the shorter wavelengths as the hole array pitch and diameter is increased to filter the longer Green and Red wavelengths [143]. Note that the ΔE (color difference) being measured here is after signal processing, meaning that filter's original spectral response (see Fig. 7.4d) has already been modified, in

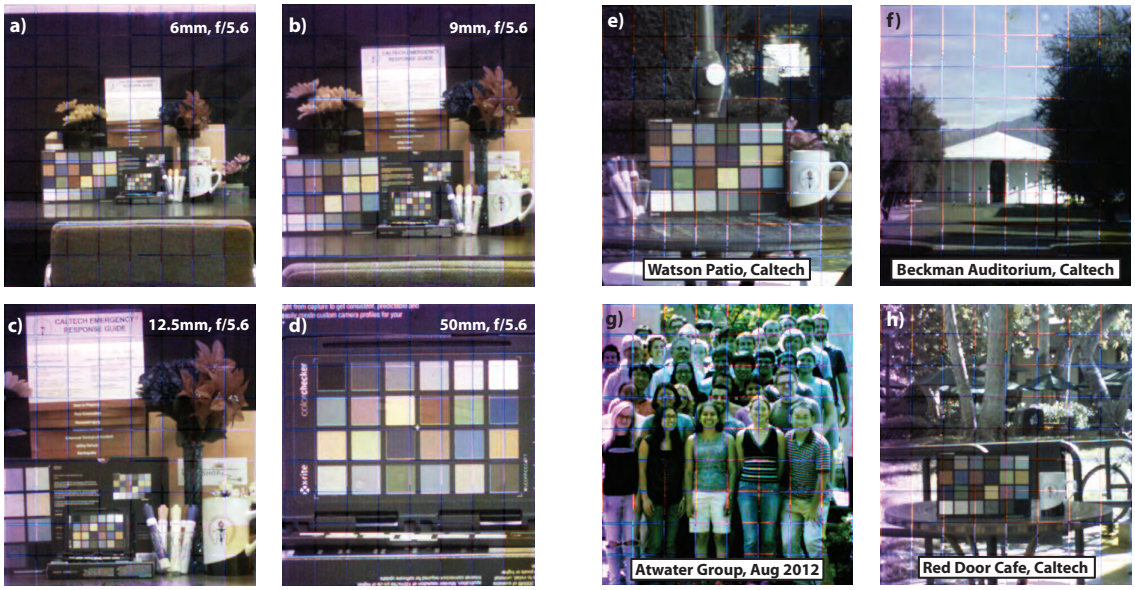

Figure 7.6: Focal length dependence and outdoor lighting conditions. Images of 24-color Macbeth chart positioned in a scene taken with integrated CMOS image sensor with RGB plasmonic hole array filter with a 5.6 f-number and a a) 6mm, b) 9mm, c) 12.5mm, and d) 50mm lens. Images taken with outdoor lighting conditions of e) Watson Patio, Caltech, f) Beckman Auditorium, Caltech, g) Atwater Group, Aug 2012, Caltech, and h) Red Door Cafe, Caltech.

particular with the linear matrix correction (see Fig. 7.5d), which corrects for the filter's original color crosstalk.

Similarly, for the complementary colors, which can be considered as linear superpositions of the primary colors, the measured ΔE is 5.7 for Yellow (Green + Red), 24.7 for Magenta (Red + Blue), and 33.3 for Cyan (Blue + Green), which is consistent with the ΔEs of the primary colors that compose them. Averaging the ΔE values of the 3 primary and 3 complementary colors, we get an averaged ΔE of 17.7 for the integrated CMOS image sensor, a value which, although not ideal, is capable of capturing vivid full color images as that shown in Fig. 7.5e. Following this image reconstruction process, we show in Fig. 7.6 several additional images taken with the integrated CMOS image sensor, other demonstrations of the technology's versatility with respect to focal length and outdoor lighting conditions.

7.10 Angle Dependence

These representative images are taken with a 5.6 f-number, corresponding to a nearly normal incident half-aperture angle of 5°; however, for proper filter performance, it is important to check that the RGB hole array filters retain their designed filter functionality for larger aperture angles. To investigate this, we simulated the transmission of the unmounted plasmonic color filter arrays for incidence angles ranging from 0-30°. The resulting spectra for the green color filter is plotted in Figs. 7.7a and b. As can be seen from these figures, the filter does have an angular dependence [56, 96, 87]; however, in order to see if this deviation will play a significant role in the filter functionality, we need to consider what range of incidence angles we are collecting for a given f-number (F). From the definition of f-number, which is the ratio of focal length (f) to aperture diameter (D), the half-aperture angle for a given f-number is equal to $\theta_{1/2} = atan(1/2F)$. This means that for an f-number of f/16, the maximum half-aperture collection angle will be 1.8°, meaning that the image sensor is collecting nearly collimated incident light. As a result, the filter function should be consistent with the normal incidence filter design for images taken with large f-numbers.

However, for f/1.8, the half-aperture angle is 15.5°, which, referring to Figs. 7.7a,b, should have some effect on the image color quality. The extent to which the image will be affected by off-normal incident light is determined by pixel signal integrated over all the incidence angles accepted by its f-number. Thus, we need to consider the transmission through a given filter color averaged over incidence angle (within its aperture angle) and polarization (to account for unpolarized light). For the green filter operating at f/1.8, we estimate the filter spectral response by averaging the filter angular transmission response for incident angles within its 15 degree acceptance angle and over both TE and TM polarizations. The resulting averaged spectrum is plotted in Fig. 7.7c, from which we see that it is similar to the normal incidence spectrum. Thus, we should expect to see admissible difference in the color of images taken with large f-number (corresponding to a small acceptance angle) and a small f-number (corresponding to relatively large acceptance angles).

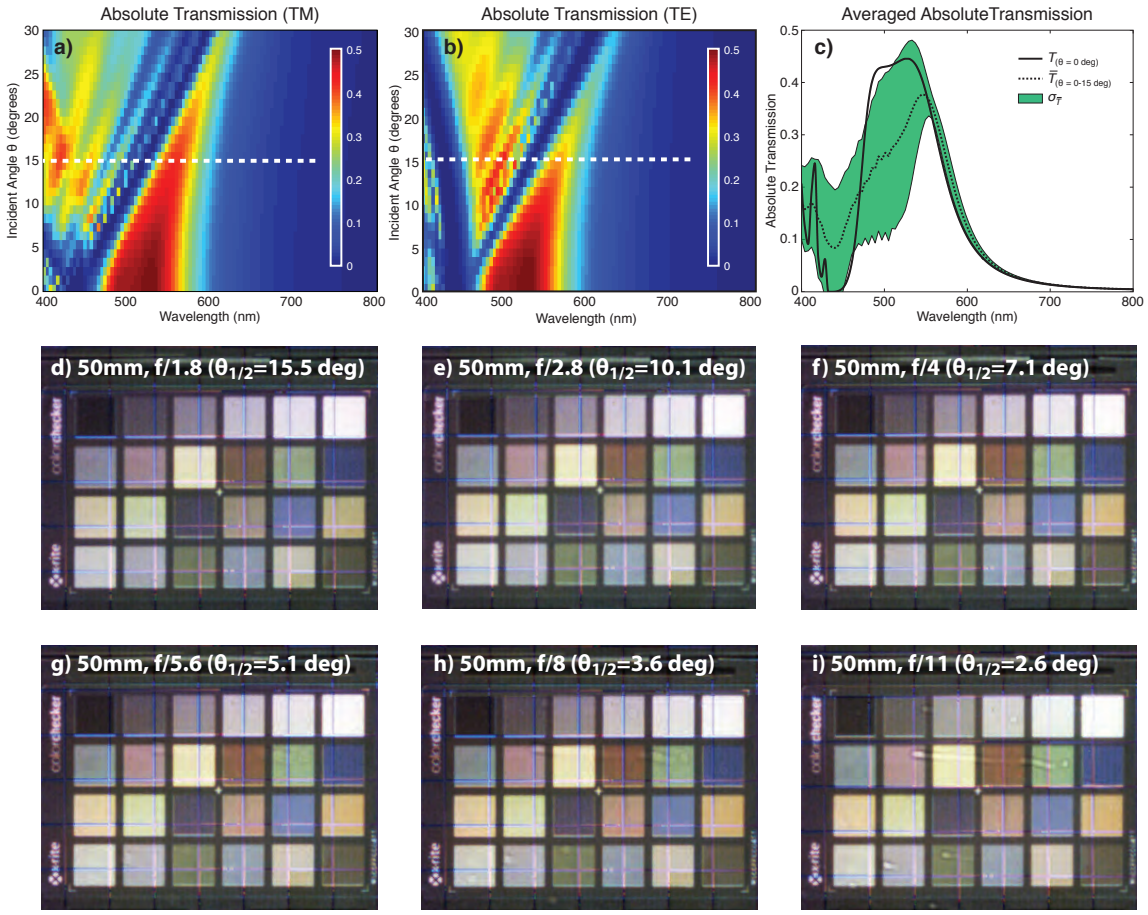

Figure 7.7: Green filter angular response and integrated CMOS IS f-number dependence. Simulated spectral transmission response of green hole array filter as a function of incident angle for a) TM and b) TE polarizations. c) Simulated spectral response of green filter operating with a maximum half-angle aperture of 15 degrees, corresponding to an f/number of about 1.8, obtained by averaging the spectral response for incident angles ranging from 0-15 degrees over both polarizations. Images of 24-color Macbeth chart taken with the integrated CMOS image sensor with RGB plasmonic hole array filter with a 50mm lens and with an f-number (maximum half-aperture angle) of d) 1.8 (15.5 degrees), e) 2.8 (10.1 degrees), f) 4 (7.1 degrees), g) 5.6 (5.1 degrees), h) 8 (3.6 degrees), and i) 11 (2.6 degrees).

Table 7.1: F-numbers and their respective ΔE values

F-number	1.8	2.8	4.0	5.6	8.0	11	16
$\theta_{1/2}$ (degs)	15.5	10.1	7.1	5.1	3.6	2.6	1.8
Blue	4.0	5.8	2.9	3.8	3.7	7.0	3.7
Green	15.1	14.5	11.0	10.2	10.7	8.3	10.1
Red	34.4	31.3	32.1	28.6	25.0	21.6	27.5
Yellow	5.9	5.5	7.0	5.7	5.1	5.6	5.8
Magenta	34.6	27.5	31.7	24.7	23.9	23.7	24.6
Cyan	20.7	31.3	30.1	33.3	31.3	33.6	32.6
6-color ave.	19.1	19.3	19.1	17.7	16.6	16.6	17.4

To confirm the f-number dependence, we took several images of a 24-color Macbeth chart using a 50 mm lens and changing the f-number from 1.8-16 (see Figs. 7.7d-i). As expected, the color looks fairly constant among all the f-number images, showing slightly dimmer color for smaller f-numbers due to the larger acceptance angles. The color is analyzed using the standard color error index, CIE ΔE 200021, which, when averaged over the 3 primary (Red, Green, Blue) and 3 complementary (Yellow, Magenta, Cyan) colors, shows a small variation of only 2.8 in going from f/16 to f/1.8 (see Table 7.1). For the primary colors, note that the CIE ΔE 2000 values for Blue are smaller than those of Green and Red across all f-numbers, demonstrating that, independent of incident angle, the plasmonic color filter design retains its good color fidelity for shorter wavelengths owing, to the suppression of the photonic modes, which remain accessible for the longer wavelength filter hole diameters [143]. Further improvement of the color fidelity between Red and Blue filters is an important direction for future research into imaging device applications of plasmonic color filters [120, 17, 78].

7.11 Conclusion

In this chapter I have demonstrated the imaging characteristics of a CMOS image sensor with an integrated primary color RGB plasmonic filter that is competitive with conventional dye-filter technology in terms of transmission and insensitivity to

f-number (incident angle), all with a single lithographic step. The ability to add color sensitivity to an image with a single perforated metal layer not only reduces the complexity and cost of fabricating tri-color filters, but also allows for new technology, such as hyperspectral imaging devices for sensing that consist of any number of color arrays. In this work the integration was done by directly contacting the plasmonic color filter array onto the CMOS image sensor, which already showed almost optimal integrated transmission efficiencies; however, future filter-chip integration will require the fabrication of the plasmonic color filter directly on the CMOS image sensor. Although the hole array filter dimensions are subwavelength, with the smallest inter-hole spacing being only 120nm for the blue (B) color filter, these dimensions are compatible with current patterning methods using conventional deep ultraviolet lithography an attractive feature for large scale manufacturing.

Chapter 8

Scattering-Absorption Nearest-Neighbor Model Description of Hole Arrays

Abstract: *Having seen in the last two chapters how we can use finite size hole array filters in a closed packed configuration for imaging applications with little to no spatial crosstalk, it is interesting to investigate the transmission properties of finite-size hole arrays as a function of nearest neighbor contributions. The analysis is similar to what was done in Chapter 6, except that here we use a fully analytic model, in which we account for the scattering, absorption, and transmission contributions of the holes in the array. We can, of course, account for the scattering contributions of all the sites in the hole array lattice, but given our findings in the last two chapters, there is an indication that only nearest neighbors play a dominant role in setting the transmission properties of hole arrays, especially for large finite-size filters. Following this analysis method, we demonstrate that the transmission spectra of hole array filters can be accurately described by second nearest neighbor scattering-absorption interactions of hole pairs, thus explaining our observations in the last two chapters and making hole arrays especially appealing for close-packed hole array filters for imaging applications. Furthermore, using this model, we find that the peak transmission efficiency of a square-shaped triangular-lattice hole array reaches* $\sim 90\%$ *of that of an infinite array at* $\sim 6 \times 6\ \mu m^2$*; the smallest size array showing near-infinite array transmission properties, making them compatible with the current size of CMOS image sensor*

technology.

8.1 Nearest Neighbor Scattering-Absorption Interactions

By investigating the scattering-absorption efficiencies of surface plasmons between hole pairs in a thin-film hole-array, we find that we can reconstruct the transmission efficiencies of large-size hole arrays using only second nearest neighbor interactions, which can, in general, be described as a superposition of scattering and absorbing events within the array [96, 109]. This model is based on considering each hole as a dipole scatterer, launching cylindrical surface plasmons with efficiency β and a Lambert's cosine law spatial distribution when illuminated, and absorbing surface plasmons that are incident upon it with efficiency β', and subsequently re-emitting them with efficiency β back into the array (Fig. 8.1). This interaction is modeled as occurring on goth sides of the thin metal film, coupled by the transmission, t, of light from the illumination-side to the transmission-side of the array.

Thus, the amount of field intensity at the mouth a given hole, at position m in the array, will be that of the incident field, H_0, plus the scattering contributions from the holes surrounding it, located at positions $j \neq m$. The fields scattered from these sites have amplitudes $H_0 \times \beta_{jm}$, where β_{jm} is the efficiency with which the holes scatter the incident light into circular surface plasmons. These plasmons spread with a cosine squared circular distribution along the direction of the incident polarization, and a $1/\sqrt{r}$ radial dependence decay to ensure constant integrated power as the wave spreads. As usual, these plasmons also decay and accumulate phase according to the propagation wavevector of the 'regular' linear SP, $\exp[ik_{spp}r]$.

In general, the m^{th} site has scattering contributions from all sites in the lattice, at positions j, such that $j \neq m$; however, here we separate the contributions in a more suggestive way by separating them into contributions coming from the first, second,

etc. nearest neighbors in the array relative to the m^{th} site of interest (Eq.8.1),

$$\begin{aligned} h_{m,top} &= \frac{H_{m,top}}{H_0} \\ &= 1 + \sum_{j \neq m} \beta_{jm} \frac{\cos^2(\theta_{jm} - \theta_p)}{\sqrt{a_{jm}}} \exp[i(k_{spp} a_{jm})] \\ &= 1 + \left(\sum_{j \in 1^{st} n.n.} + \sum_{j \in 2^{nd} n.n.} + ... \right) \beta_{jm} \frac{\cos^2(\theta_{jm} - \theta_p)}{\sqrt{a_{jm}}} \exp[i(k_{spp} a_{jm})] \end{aligned} \tag{8.1}$$

where θ_p is the polarization direction, θ_{jm} and a_{jm} are the angle and distance from site j to m, respectively, and k_{spp} is the surface plasmon propagation wavevector.

Once these interactions occur at the top side of the array, they are transmitted across the thin film metal layer with transmission t, where the whole scattering-absorption process takes place all over again. The field from the m^{th} site is simply transmitted and is contributed to by the fields transmitted and scattered by the holes surrounding it (Eq. 8.2),

$$\begin{aligned} h_{m,bot} &= \frac{H_{m,bot}}{t} \\ &= h_{m,top} + \sum_{j \neq m} h_{j,top} \ \beta_{jm} \frac{\cos^2(\theta_{jm} - \theta_p)}{\sqrt{a_{jm}}} \exp[i(k_{spp} a_{jm})] \\ &= h_{m,top} + \left(\sum_{j \in 1^{st} n.n.} + \sum_{j \in 2^{nd} n.n.} + ... \right) h_{j,top} \ \beta_{jm} \frac{\cos^2(\theta_{jm} - \theta_p)}{\sqrt{a_{jm}}} \exp[i(k_{spp} a_{jm})] \end{aligned} \tag{8.2}$$

These field amplitudes then radiate through spherical waves emanating from the exit side of the array, summing in the far-field to form the transmission spectra of the array. The efficiency of the array can then be defined as the field amplitude squared of the sum of all the scattering contributions from the holes at the exit side of the array, normalized to the amplitude squared of N times a single hole, tH_0 (Eq. 8.3),

$$\eta_N = \frac{\left| \sum_{m=1}^{N} h_{m,bot} \right|^2}{N^2} \tag{8.3}$$

In this set of equations, Eq. 8.1–8.3,for a given wavelength, k_{spp} is set by the

materials used, θ_p by the illumination polarization, θ_{jm} and a_{jm} by the array configuration, and t divides out in Eq. 8.3, thus leaving only β_{jm}, the scattering-absorption efficiency, as the only unknown variable.

8.2 Extracting the Hole-Pair Scattering-Absorption Coefficients

The scattering-absorption efficiencies are found by fitting finite-difference time-domain (FDTD) transmission data to a scattering-absorption model described in Eq. 8.1–8.3, essentially consisting of a truncated Fraby-Perot resonance between hole pairs [96, 109]. The fit is done using FDTD to simulate the transmission spectra of a symmetric triangular lattice unit cell consisting of a 4-hole diamond-shaped configuration (Fig. 8.2a) as a function of pitch and wavelength. The holes are modeled as 180-nm-diameter SiO_2 cylinders in a 150-nm Al film cladded form top and bottom by SiO_2, illuminated with visible frequency pulse polarized along the 1-3 hole orientation (Fig. 8.2a). Since the scattering-absorption efficiencies are expected to be wavelength dependent, we fit the spectra by fixing the wavelength and fitting the hole-pair scattering-absorption model as a function of pitch [96]. Note that this configuration only consists of first nearest neighbor contributions, and thus, we account for all the contributions of the array for the model fit.

The FDTD data, along with the fitted curve, are shown in Fig. 8.2b for $\lambda_0 =$ 400 nm, from which we can see excellent agreement between the simulation and model results. We note that although subwavelength holes are known to scatter both spherically expanding SPs [96, 54] as well as regular linear SPs [110], in this model we only account for the scattering contribution of spherical SPs, which we find dominate the transmission spectra of the array. Thus, fitting to the spherical surface plasmon alone yields fits that are almost in perfect agreement with the FDTD data, but perfect agreement is obtained only by including the linear SP contributions, thus highlighting their lower weight in determining the overall hole array transmission spectra. By

varying the wavelength and repeating the fitting procedure, we extract the spectrally resolved complex-valued scattering-absorption parameters for the 180-nm-diameter hole (Fig. 8.2b).

By spectrally resolving this scattering-absorbing coefficient, we find that it has a amplitude maximum at a surface plasmon wavelength that is roughly twice the diameter of the hole (see Fig. 8.2c), i.e., $d \sim \lambda_{SP}/2$ [28]. Since the transmission of the array is expected to be dominated by the amplitude of the scattering-absorption efficiency coefficient, in selecting the best suited hole diameter for filtering a given color, we need only to look for the maximum of this curve. Thus, in looking at Fig. 8.2c, we see that a 180-nm hole is best suited for filtering ∼550 nm (green) light. By following a similar fitting process for different size holes, we find that the best suited holes for filtering red (∼650 nm) and blue (∼450 nm) wavelengths are $d = 240$ nm and $d = 140$ nm, respectively, in agreement with known values [143].

8.3 Number of Contributing Nearest Neighbors

Given the combined scattering-absorption efficiencies, in order to build a nearest neighbor model, we need to determine the spatial extent to which these efficiencies play a role in setting the transmission spectra of finite-size hole arrays. Since we are treating the transmission of a hole array as a superposition of scattering-absorption events between hole pairs, in considering the contributing scattering events surrounding a given hole site, it is sensible to only consider those scattering events that occur at hole positions that are in the line-of-sight of that hole of interest. Thus, to first order, we approximate the transmission of an array by only considering second nearest neighbor interactions, since scattering events occurring at positions farther than this are screened by the first and second nearest neighbors of a hole site (see Fig. 8.1a). To validate the accuracy of the second nearest-neighbor scattering model, we compare the transmission spectra of several large-size hole array configurations obtained by both FDTD (Fig. 8.3) and the model (Fig. 8.1b), with both spectra in good agreement of each other. We note that the second nearest neighbor approximation is only valid

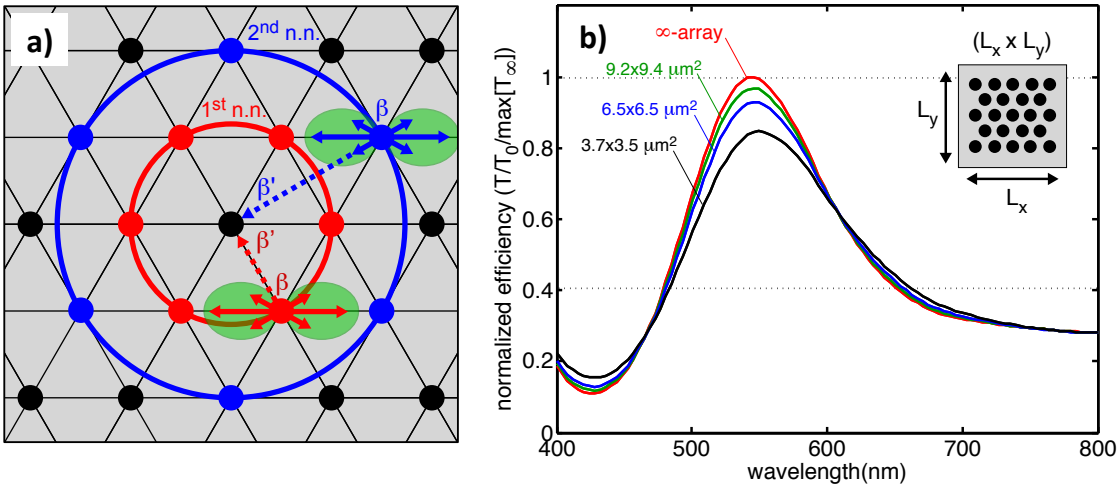

Figure 8.1: (a) Schematic of the second nearest-neighbor (n.n.) scattering-absorption model used to reconstruct the transmission spectra of a square-shaped triangular-lattice hole array (b). The black circles represent holes in a triangular lattice, connected by black lines for reference. The first and second nearest neighbors surrounding the central lattice point are shown in red and blue, respectively. The scattering intensity of a contributing lattice site is depicted by green ovals, with the enclosed arrows corresponding to the spatial scattering efficiency amplitudes (β). The absorption efficiencies (β') of the central lattice are depicted by dashed arrows. (b) Transmission efficiency curves extracted from the scattering model (a) as a function of array size for the square-shaped triangular-lattice hole array shown on the inset, consisting of 180-nm-diameter holes set at a pitch of 430 nm in a 150-nm-thick Al film embedded in SiO_2. The red curve corresponds to a 40×40 μm array, which we call '∞-array', due to its asymptotic behavior. We normalize to the peak transmission efficiency of this curve for reference. The other curves correspond to normalized transmission efficiencies for different size hole arrays ranging from $\sim 4\times4$ – 10×10 μm^2 in size. The horizontal dashed curve at 0.4 corresponds to the normalized transmission efficiency of a single isolated hole.

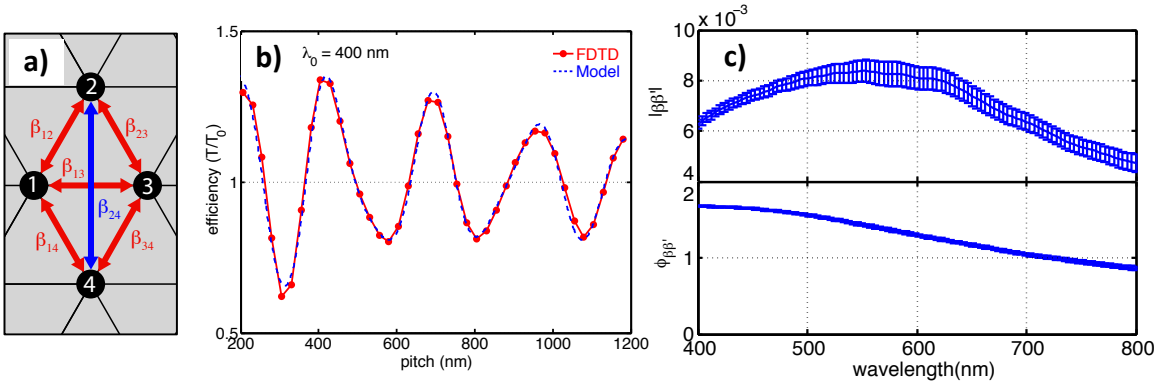

Figure 8.2: (b) Transmission efficiency as a function of pitch for a symmetric 4-hole triangular-lattice unit cell (a), consisting of 180-nm-diameter holes set at a pitch of 430 nm in a 150-nm-thick Al film embedded in SiO_2. The red dotted spectrum is extracted from FDTD simulations, and the blue dashed spectrum corresponds to the fitted scattering-absorption model. The horizontal dashed curve at 1 corresponds to the normalized transmission efficiency of a single isolated hole. (c) Spectrally resolved scattering-absorption parameters obtained by varying the wavelength from 400 – 800 nm and fitting as done in (b).

for hole arrays in which the array extent is much larger than the second nearest neighbor distance, with smaller arrays requiring third and higher order nearest neighbor contributions to properly set the in-plane phase that determines their transmission (see Fig. 8.4).

8.4 Setting the Periodicity of the Array

Given a hole array configuration, say, composed of 29×17 180nm-diameter holes, we note that the position of the transmission peak can be tuned by varying the period of the array (see Fig 8.5). However, the amplitude of the transmission peak is maximum for periodicities that set the transmission peak to have maximum overlap with the amplitude of the SP scattering-absorption coefficient (see Figs. 8.2c and 8.5). Thus, we find that the best suited pitch for filtering ∼550 nm (green) light with 180-nm-diameter holes is $p \sim 340$ nm. By following a similar period variation for the 240-nm- and 140-nm-diameter holes, we find that their optimal pitch for filtering red (∼650 nm) and blue (∼450 nm) light are 420 nm and 260 nm, respectively. These (p, d)

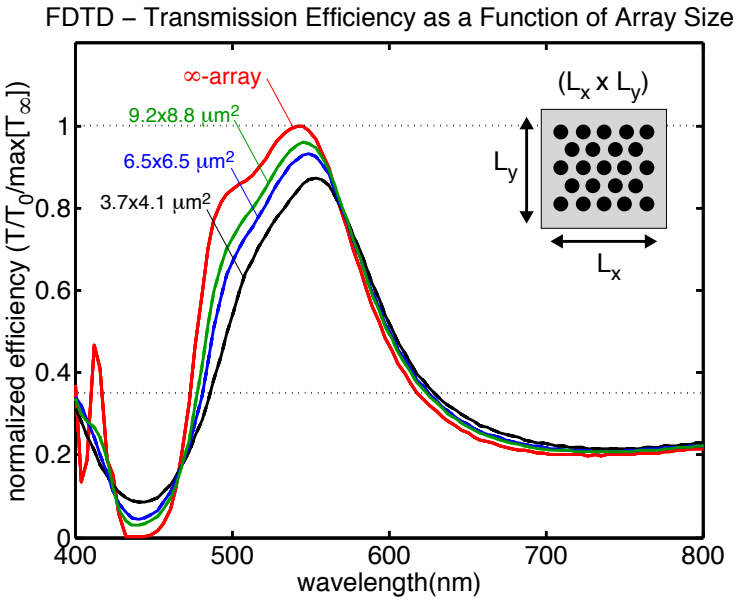

Figure 8.3: Normalized transmission efficiency curves extracted from FDTD as a function of array size for the square-shaped triangular-lattice hole array shown on the inset, consisting of 180-nm-diameter holes set at a pitch of 430 nm in a 150-nm-thick Al film embedded in SiO_2. The red curve corresponds to an infinite array, to which we normalize for reference. The other curves correspond to normalized transmission efficiencies for different size hole arrays ranging from $\sim 4\times4-10\times10$ μm^2 in size. The horizontal dashed curve at 0.35 corresponds to the normalized transmission efficiency of a single isolated hole.

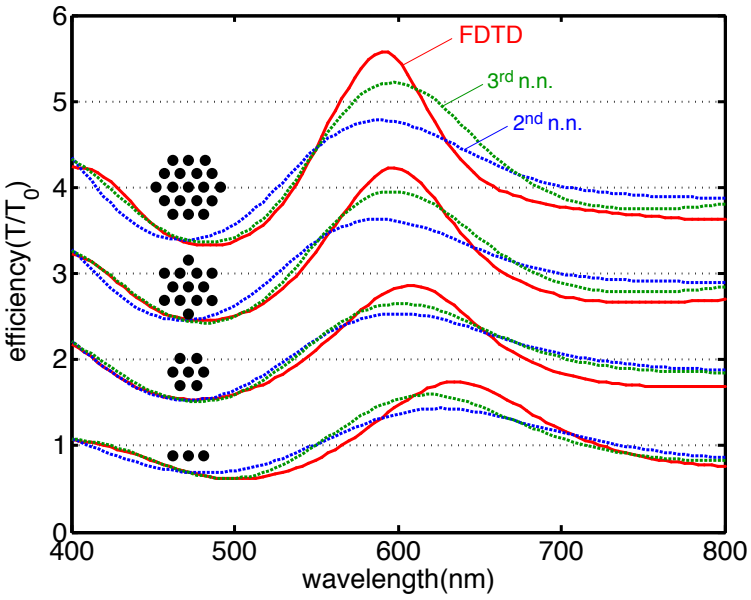

Figure 8.4: Transmission efficiency for different hole array configurations as a function of number of contributing nearest neighbors (n.n.). Data is shown for spectra calculated with FDTD, as well as with the nearest neighbor scattering model with second and third n.n. contributions. The hole array configurations (see insets) consist of 180-nm-diameter holes set at a pitch of 430 nm in a 150-nm-thick Al film embedded in SiO_2.

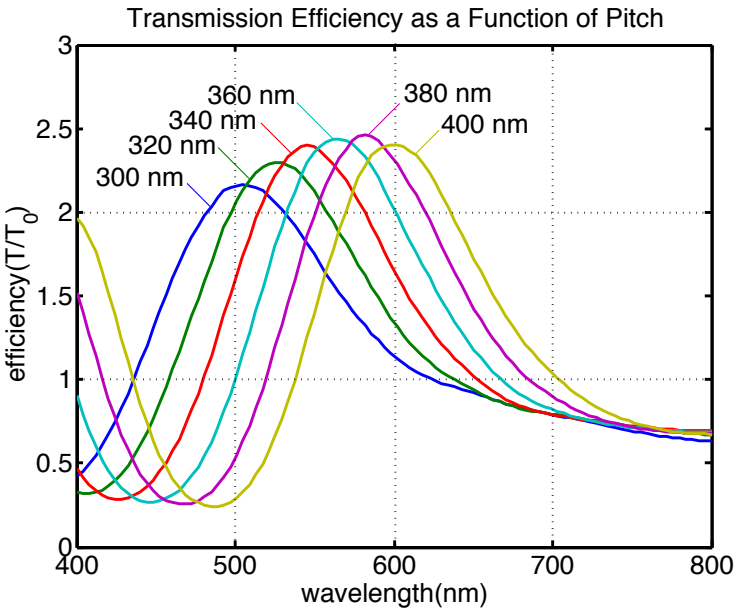

Figure 8.5: Absolute transmission efficiency curves extracted from the scattering model as a function of array pitch for a $\sim 10 \times 10$ μm^2 square-shaped triangular-lattice hole array, consisting of 180-nm-diameter holes set at a pitch of 430 nm in a 150-nm-thick Al film embedded in SiO_2.

values for filtering RGB light are verified with FDTD by doing small variations around the predicted values.

Having found the optimal (p,d) values for filtering RGB light, we use the model to determine the transmission properties of finite-size hole arrays as they pertain to imaging applications. More specifically, we are looking for the smallest size hole arrays showing near-infinite transmission properties. To do this, we calculate the transmission spectra of a square-shaped triangular-lattice array as a function of array size (Fig. 8.1b). Starting with a $\sim 3 \times 3$-μm^2 array, which is on the order of a CMOS IS pixel size, we systematically add rows and columns to the array and monitor the evolution of the transmission efficiency spectra, normalizing to an 'infinite' 40×40-μm^2 array for reference. In looking at the asymptotic behavior of the spectra, we find that the finite array spectra is already at $\sim 80\%$ the peak efficiency with respect to the infinite array for sizes as small as $\sim 4 \times 4$ μm^2, consisting of only $\sim 10 \times 6 = 60$ holes. This value increases to $\sim 90\%$ for array sizes $\sim 6 \times 6$ μm^2, with minimal incremental

increase after $\sim 10 \times 10$ μm^2. Thus, we find that $\sim 6 \times 6$ μm^2 is the smallest array showing near-infinite array transmission properties, with any additional increase in size only bringing marginal benefit in transmission. These findings are substantiated by our findings in Chapter 6, where we found a spatial crosstalk of only $\sim$1 μm between different color hole filters, and $\sim 5 \times 5$ and $\sim 10 \times 10$ μm^2 filters showing similar peak transmissions in the $80 - 90\%$ range.

8.5 Conclusion

In this chapter, we have seen how the transmission of hole arrays, once believed to be dominated by the long range grating vector condition, are actually dominated by nearest neighbor scattering contributions. Furthermore, we have shown that the scattering-absorption inefficiencies of hole pairs peak at a plasmon wavelength that is roughly twice the size of the hole diameter, i.e., $d \sim \lambda_{SP}/2$, allowing us to easily select the best suited hole for filtering a given wavelength of light. Similarly, as previously reported by other groups, we find that the transmission peak position of a hole array is tunable with the hole array pitch, but here we show that the transmission peak amplitude is maximum when we select a pitch that has maximum overlap with the hole-pair scattering-absorption efficiency. Then, by analyzing the contributions of nearest neighbors, we find that second contributions are sufficient to describe the transmission properties of large finite size hole arrays, but requiring third contributions for smaller-size configurations. In this manner, we have shown that the peak transmission efficiency of a hole array reaches $\sim 90\%$ that of an infinite array at $\sim 6 \times 6$ μm^2, thus demonstrating their potential for full scale CMOS IS integration, as demonstrated in Chapter 7. But the ability to add color sensitivity to an image with a single perforated metal layer dominated by nearest neighbor interactions not only reduces the complexity and cost of fabricating tri-color filters, it also allows for new technology such as hyperspectral imaging devices for sensing that consist of any number of color arrays.

Part III

Resonant Guided Wave Networks

Chapter 9

Resonant Guided Wave Networks

Abstract: *In the last two sections, we have seen how plasmonic coaxial and hole arrays can serve as efficient platforms for designing negative index metamaterials and color filters for imaging applications. However, as mentioned in Chapter 1, one of the most appealing aspects of plasmonics is its subwavelength confinement, which serves as the ideal platform for designing photonic circuitry. In this section, we investigate the properties of another new type of artificial photonic material called Resonant Guided Wave Networks (RGWNs), in which isolated waveguides are assembled in a network layout to form closed loop resonances, with which we can engineer material dispersion and circuit functionality. Furthermore, we present an experimental realization of this concept, in which we integrate it with conventional Si technology, bringing plasmonic circuitry closer toward chip implementation.*

9.1 Introduction

In the last two decades, the development of new photonic material design paradigms has opened up new avenues for designing photonic properties based on different underlying physics. For example, photonic crystals are based on dispersive Bloch wave modes that arise in periodic index structures. Different in operation than photonic crystals, metamaterials [122, 114] are based on subwavelength resonant elements (or 'meta-atoms') that interact with incident radiation to give rise to complex refractive indices. In this chapter, we introduce a new approach to optical dispersion control

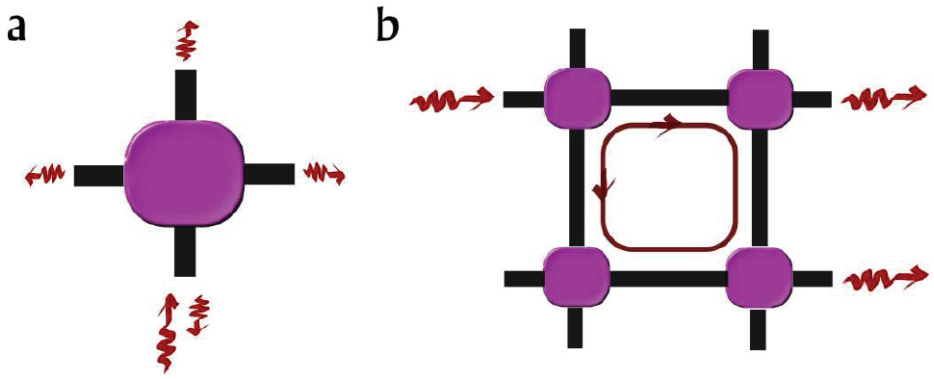

Figure 9.1: Schematic illustration of (a) a 4-terminal equal power-splitting element and (b) a local resonance in a 2x2 RGWN.

based on resonant guided wave networks (RGWNs) in which power-splitting elements are arranged in two- and three-dimensional waveguide networks.

A possible framework for comparing and classifying photonic design paradigms is according to their basic resonating elements, with which light interacts to give the desired artificial dispersion. Under this classification scheme, we can think of materials that operate based on the local interaction of waves with sub-wavelength resonating elements (i.e. metamaterials), structures based on the nonlocal interference of Bragg periodic waves (i.e. photonic crystals), and arrays of coupled resonator optical waveguides (CROWs), where adjacent resonators are evanescently coupled [142]. Different from these existing concepts, the dispersion that arises in RGWNs is a result of the multiple closed-path loops that localized guided waves form as they propagate through a network of waveguides connected by wave-splitting elements. The resulting multiple resonances within the network give rise to wave dispersion that is tunable according to the network layout. These distinctive properties, which will be described here, allow us to formulate a new method for designing photonic components and artificial photonic materials.

A RGWN is comprised of power-splitting elements connected by isolated waveguides. The function of the splitting element is to distribute a wave entering any of its terminals between all of its terminals, as illustrated in Fig. 9.1a. The waves are then propagated in isolated waveguides between the splitting elements, where

the local waves from different waveguides are coupled together. For example, four splitting elements arranged in a rectangular network layout form a 2×2 RGWN (see Fig. 9.1b). When one of the terminals is excited, the multiple splitting occurrences of the incident wave within the network form closed path resonances that reshape the dispersion of the emerging waves according to the network layout and is different from the dispersion of the individual waveguides. Properly designing this network layout reshapes the interference pattern and the optical function of the RGWN, as will be exemplified later in this chapter. The 2×2 RGWN consists of one closed loop resonance; however, larger two- or three-dimensional networks can support multiple resonances, which give rise to more design possibilities.

Although the concept of RGWNs is quite general, we will first illustrate the underlying physics of this paradigm using plasmonics, since it allows for a simple topological implementation. After introducing this implementation, in the following sections we will demonstrate how the local wave interference can be designed to engineer small (2×2) energy storage RGWN resonators, and also how we can program the optical transmission function of inhomogeneous RGWNs using transfer matrix formalism. We will also address how the same design principles can be utilized to control the optical dispersion properties of infinitely large RGWNs that behave like artificial optical materials. After addressing other possible implementation and practical issues, we will conclude with possible future directions and a more detailed comparison to other optical design paradigms.

9.2 Plasmonic RGWN Components

The operation of RGWNs is based on two basic components: power-splitting elements and isolated waveguides. While the waveguides could easily be implemented using dielectric waveguides [47], the power-splitting elements at the intersection of two such waveguides could not be achieved using dielectrics alone. Nevertheless, this splitting operation, which is the key enabler of this technology, is native to the intersection of two plasmonic waveguides. Consequently, a possible implementation of a RGWN

is by using plasmonics via a mesh of intersecting sub-wavelength air gaps in a metal matrix.

Surface plasmon polaritons (referred here to as plasmons for brevity) are slow surface waves that propagate at metal-dielectric interfaces. Adding another metal-dielectric interface to this system results in a metal-dielectric-metal (MDM) waveguide, which supports a highly confined plasmon wave (the lowest order transverse magnetic mode - TM_0) that does not get structural cut-off as the dielectric gap between the metal layers becomes vanishingly small. The existence of this lowest-order plasmonic mode in MDM waveguides allows for such plasmonic components as power splitters [51] and high transmission sharp waveguide bends (for a review of MDM waveguides and their possible applications, see [50]). However, the existence of metal in the MDM waveguide configuration does add a source of a modal attenuation to the system as a result of the usual loss mechanisms present in any real metal-containing system. This results in a trade-off between the compression of the modal cross-section and the modal attenuation as the air gap size is decreased. Since the loss in metals is strongly frequency- and material-dependent, the focus here will be on RGWNs composed of Au-air-Au MDM waveguides operating at telecommunication frequencies, where the modal propagation lengths are on the order of tens of microns, which are substantially larger than the propagation lengths at visible frequencies. The optical properties of the materials throughout this chapter are based on tabulated data [97].

In this implementation, the intersection of two sub-wavelength MDM waveguides forms an X-junction that functions as the power-splitting elements in the network [51], and the MDM segments between the intersections serve as the isolated waveguides connecting the X-junctions. Through this implementation, X-junctions can be tuned to split power equally at infrared wavelengths both for continuous waves and for short pulse waves consisting of only a few optical cycles while conserving the shape of the input signal. The observed equal-power split is a result of the subwavelength modal cross-section of the input plasmonic waveguide that excites the junction with a broad spectrum of plane waves. As such, equal four-way optical power-splitting is enabled for transmission lines (e.g., MDM and coaxial configurations), but cannot be

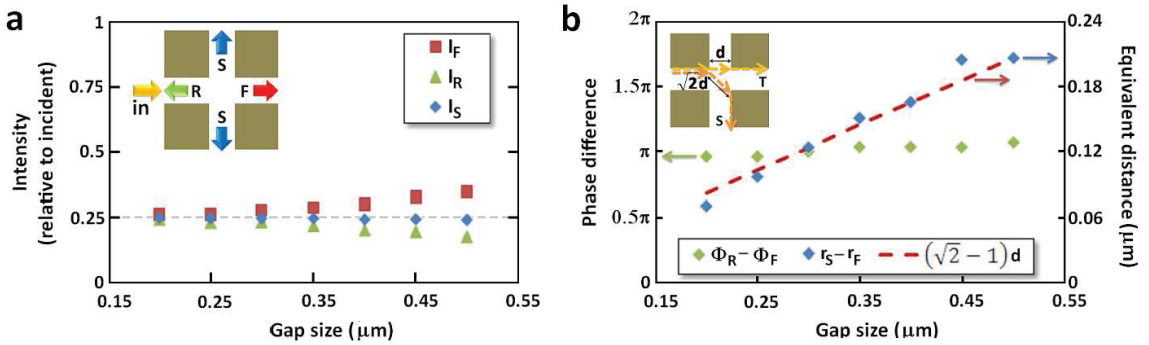

Figure 9.2: Power-splitting properties of the emerging pulses in an X-junction: (a) intensity relative to the exciting pulse, and (b) phase difference at λ_0=1.5 μm [48].

easily achieved using purely dielectric waveguides, due to their half-wavelength modal cross-section limit. Thus, through a plasmonic implementation, the strong coupling to all four neighboring X-junctions gives the plasmonic RGWN structure an optical response different from a cross-coupled network of purely dielectric waveguides, where most of the power would be transmitted in the forward direction, with only weak coupling to perpendicular waveguides.

As the MDM waveguide air gap thickness is varied, the power-split between the X-junction terminals can be tuned both in terms of amplitude and phase [48]. This, in addition to determining the phase accumulation in the waveguide segments, sets independent controls in designing the interference pattern that governs the operation of a RGWN. The power-splitting in the Au/air X-junction was investigated using the 2D finite-difference time-domain (FDTD) method with short pulse excitation and two equal-thickness intersecting MDM waveguides. Through this study, it was found that for small (0.25-μm) MDM gaps, these plasmonic X-junctions exhibit equal power-splitting with the reflected pulse being out-of-phase (i.e., approximately π-phase shifted) with respect to the sideways and forward transmitted pulses. As illustrated in Fig. 9.2a, as the MDM gap size is increased, the optical power flow deviates from equal power-splitting between the terminals toward dominant power transmission directly across the X-junction, which resembles the wavelength-scale photonic mode limit. Furthermore, in these calculations, the phase shift between the

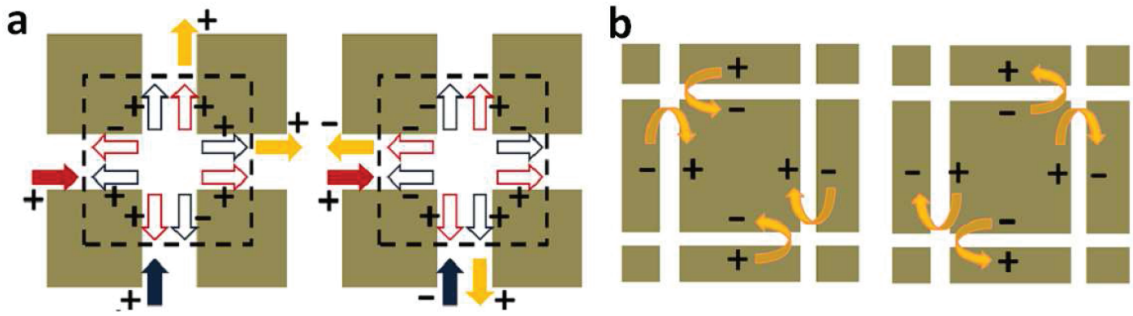

Figure 9.3: Resonance build-up in a 2×2 RGWN. (a) Two in/out-of phase input pulses result in destructive/constructive interference inside the network. (b) Steady-state of waves resonating in a 2×2 network where each pair of pulses excites the X-junctions out of phase [48].

sideways (S) and the forward (F) transmitted pulses is consistent with the geometrical difference in their pulse propagation trajectories (see Fig. 9.2b).

9.3 Resonators

After characterizing the properties of the RGWN building blocks, we illustrate the working principles of RGWNs by investigating the dynamics of a compact 2×2 RGWN resonator. In order to form a resonance, the network is designed such that when an X-junction is excited from the internal ports, the exciting waves are out-of-phase, resulting in constructive interference inside the network, as illustrated in Fig. 9.3. For such out-of-phase excitation the fields in the external terminals interfere destructively, and the power is coupled back into the resonator, enhancing the energy storage quality factor (Q-factor).

When the 2×2 RGWN is excited from the lower-left arm (see Fig. 9.4), after a transient that includes the first five splitting events, the resonant state is reached as pairs of pulses resonate between junctions 1 and 3 (exemplified by snapshot t_6) and junctions 2 and 4 (exemplified by snapshot t_7). However, before this steady state is reached, it is instructive to follow the dynamics that lead up to this resonance. Starting with the third power-split, this event occurs as junctions 1 and 3 are both

simultaneously excited by two waveguides. The incoming pulses arrive at both junctions in-phase, which would result in destructive interference inside the network if the R and S split components of each pulse were exactly π-phase shifted. However, the interference is not completely destructive, due to the finite size of the waveguides, which causes the phase difference to deviate from a perfect π-phase shift (in accordance with Fig. 9.2). This power-splitting event determines how much power couples into the network. For all future power-splitting events after the third one, the two pulses arriving simultaneously at each junction are out-of-phase and therefore interfere constructively inside the resonator. The trade-off between coupling power into the resonator and maintaining it inside suggests that MDM gap sizes that are subwavelength, but not arbitrarily small, will maximize the network resonance. To interpret the FDTD observations and arrive at the conclusion described above, a simplified analytical description of pulse propagation in the network is derived, in which only a few parameters are tracked: phase, amplitude, position and direction. The pulses are assumed to travel in the waveguides and split into four new pulses upon arrival at an X-junction. This model also illustrates the compactness of the possible mathematical representation of RGWNs, and the importance of this advantage becomes more substantial when considering the dynamics of larger 2D and 3D network topologies.

Calculating the Q-factor of such 2×2 RGWN resonators (Fig. 9.5) illustrates the role of interference in generating a strong network resonance, which causes the network Q-factor to be an order of magnitude larger than what would be expected if optical power-splitting in the X-junctions operated incoherently, i.e., we lost half the power in each splitting event. Increasing the MDM gap size causes the phase of the interfering waves to deviate from being π-phase shifted, resulting in a degradation of the constructive interference inside the resonator and a decrease in the overall network Q-factor. On the other hand, as the gap size is decreased, the plasmonic mode attenuation increases, due to metallic losses in the waveguides. Between these two competing effects, the maximal Q-factor value is obtained for a gap size of 250 nm. These RGWN Q-factor values are considerable for plasmonic resonators and

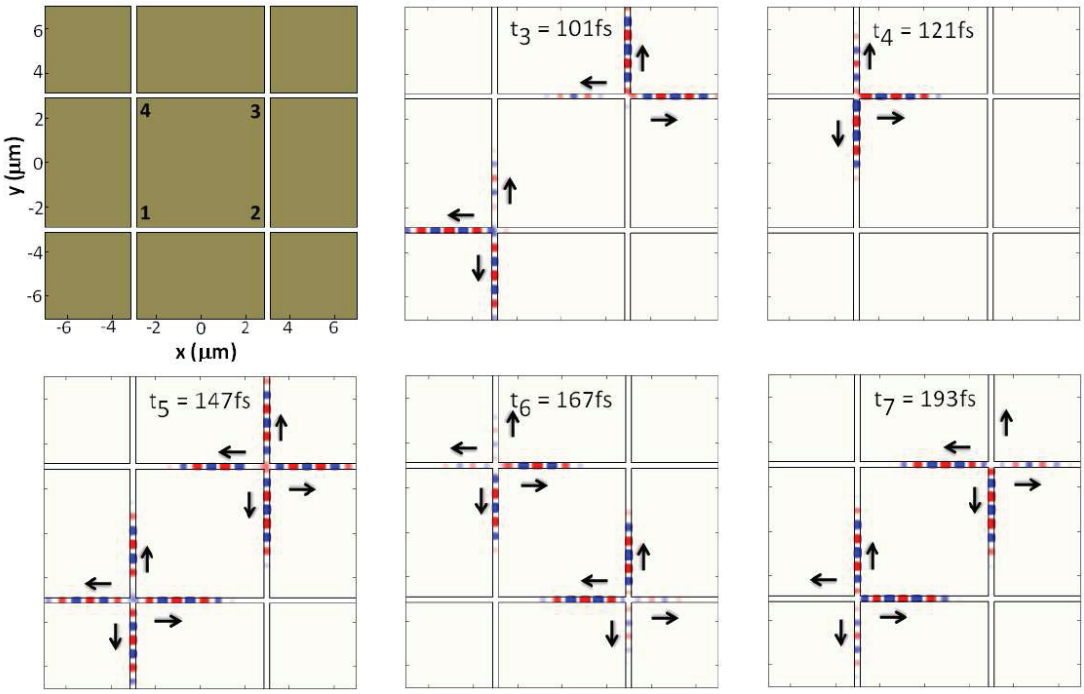

Figure 9.4: Time snapshots of H_z (normalized to the instantaneous maximum value) in a 2×2 plasmonic RGWN recorded at the third to the seventh power-splitting events for a 2D-FDTD simulation. The MDM waveguides are 0.25 μm thick and 6 μm long [48].

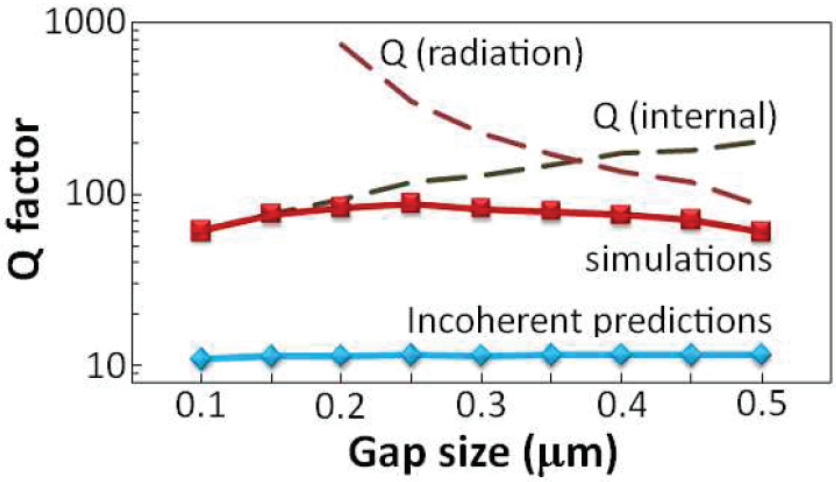

Figure 9.5: Q-factor of 22 RGWN resonator from simulation results compared with those resulting from incoherent power-splitting [48].

even comparable to typical values of wavelength-size dielectric resonators that are dominated by radiation loss (e.g., a cylindrical dielectric cavity of radius 1.3λ with a purely real refractive index of $n = 2.5$ surrounded with air has a Q 100). If we were to artificially decrease the Au loss at 1.5 μm (or alternatively go to longer wavelengths), the Q-factor of the resonator would increase appreciably (e.g., Q $\sim$ 750 for a 200 nm gap width), indicating that the resonator Q-factor is primarily limited by the material loss.

9.4 Tailoring the Optical Properties of Artificial Materials

After studying the resonance effects in a small RGWN, we now investigate the dispersion characteristics of infinitely large 2D periodic RGWNs by modelling the structure unit cell in FDTD with Bloch boundary conditions. Through this analysis, we find that RGWNs exhibit wave dispersion and photonic bandgaps due to interference effects, and that their band structure can be controlled by modifying the network structural parameters. Two different length-scales control the network dispersion:

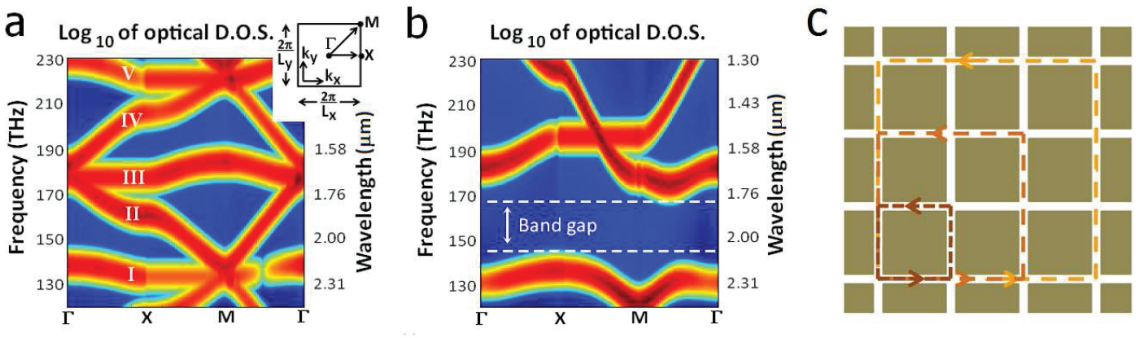

Figure 9.6: Photonic band structure of infinitely large periodic RGWNs [48].

the subwavelength width of the MDM gaps determines the phase shift at each X-junction, and the wavelength-order distance between the nodes, along with network topology, determine the interference scheme.

The same interference dynamics that govern the energy storage in finite-size 2×2 RGWN resonators also control the optical properties of artificially-designed RGWN materials of infinite size. If the network parameters are chosen such that a planewave excitation at a given incidence angle results in a resonance effect similar to the one demonstrated for the 2×2 network, then this would correspond to a forbidden state of propagation in the photonic band diagram. Examining the optical density of states (DOS) for different wave vectors over frequencies in the near infrared range, where the material (Au in this case) dispersion is small, we observe a photonic band structure, which is only due to dispersion resulting from the network topology, as shown in Fig. 9.6a. The functionality of the infinitely large RGWN is not hindered by loss, since its dispersion depends on the waveguide decay length being much larger than the size of the largest resonant feedback loop that has dominant contribution to the RGWN dispersion. Further possibilities for achieving band dispersion control are illustrated in Fig. 9.6b, showing a flat band over a wide range of wavevectors at 130 and 170 THz, as well as the formation of a photonic bandgap between 140–160 THz, for appropriately chosen network parameters.

The infinitely large RGWN is illustrated in Fig. 9.6c, along with a few schematic resonance orders that represent the resonances that could arise within the network.

The operating mechanism of the RGWN is very different from that of photonic crystals composed of metal/dielectric alternating materials. Although the schematic layout might look similar, the difference between the two classes of artificially designed optical materials becomes clear when considering the difference in the length scales of their composite elements. Whereas photonic crystals operate based on non-local interaction of Bloch waves with the entire array, RGWNs rely on the interference of local waves. Therefore, RGWNs are not sensitive to the actual topology of waveguides between junctions but only to its trajectory length, whereas the properties of photonic crystals would greatly depend on the shape of the periodic metallic islands. Additionally, RGWNs do not necessarily have to be periodic to operate as resonant guided wave networks, and, for the same reason, planting a defect in a RGWN would not have the same effect as it would in a photonic crystal.

9.5 Programming the Optical Properties of a Network

Because the underlying physics of RGWNs is based on the interference of local waves, it allows for layouts that are inhomogeneous and non-periodic across the network. Unlike photonic crystals, which are restricted to Bragg wave effects in periodic structures, the flexibility of RGWNs opens up design possibilities, where the wave properties are varied across the structure. With respect to metamaterials, which could inherently be nonhomogeneous due to the local nature of the interaction between light and the meta-atoms, RGWNs have the advantage of having interference effects within the network, which allows for frequency spectrum reshaping designs through these effects.

An additional unique feature of RGWNs relates to the constraints on wave propagation within the structure. Unlike other photonic designs, RGWNs have a limited number of modes that are allowed to propagate within the structure (e.g., only the TM_0 mode for the case of the plasmonic implementation described previously). Furthermore, the waves can propagate only inside the waveguides connecting the splitting

elements. The different waveguides are coupled only by X-junctions, which each have only a limited number of terminals. This level of control is beneficial for several reasons. First, the interference pattern in the network can be controlled more directly. Second, it allows for a comprehensive mathematical representation of the RGWN by scattering matrix (S-matrix) formalism that greatly reduces the computational complexity of programming the network. Third, since the waveguides are isolated from each other, their only contribution to the network is to serve as phase retardation elements between the splitting elements. As a result, the waveguide length is the only effective parameter in its contour, as long as the bending is not too severe. This waveguide feature allows for the network to maintain its engineered function even when distorted. Additionally, the ability to utilize curved or bent waveguides to accommodate long contours is useful when designing the interference pattern of RGWNs.

These distinctive RGWN characteristics open up new opportunities for designing photonic devices by programming the entire network rather than by assembling interconnected discrete components with traceable functions. The usual way of designing photonic devices is to target the desired subsystem functions, map them logically into sub-functions, and then assembling components that carry out these sub-functions in the desired system. For example, a wavelength router could be designed using add/drop ports where the input and output waveguides are coupled by wavelength sensitive ring resonators [72] or by defects in a photonic crystal [43]. Similarly, in free space optics, this function could be achieved through the use of collinear beam splitters, each designed to deflect a desired wavelength band. In these schemes, the couplers and waveguides are discrete components that are associated with a specific function, and are combined in a logical way to carry out the overall system function. An alternative approach is to use a network of components that carries out the desired function but, unlike traditional designs, there is no specific logical sub-function associated with any individual component. While the inner connectivity of the device will be less intuitive, it has the potential to result in more efficient designs of complex and compact devices.

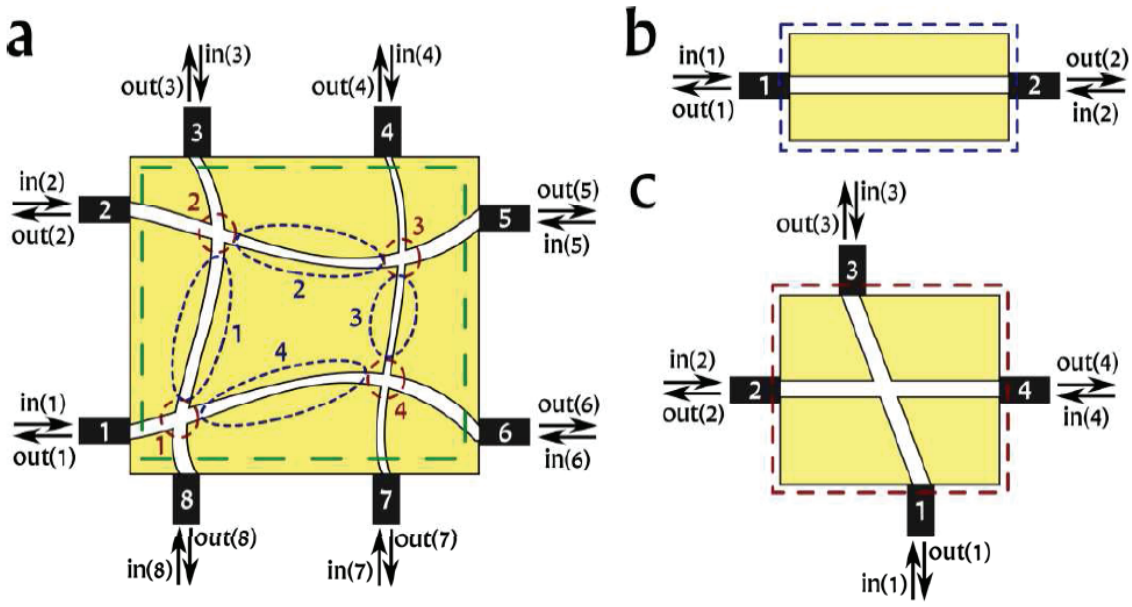

Figure 9.7: Mathematical representation scheme of (a) a 2×2 RGWN system and its components, (b) a waveguide component, and (c) an X-junction component [49].

One possible way of representing a system function in a RGWN is through the use of a scattering operator that maps the set of local waves entering the device terminals to the set of the waves exiting from the same terminals [49]. Since a RGWN is composed of a discrete set of components (waveguides and X-junctions) and terminals, the system function is represented by a scattering matrix (S-matrix) connecting the vectors of the waves entering and emerging from the RGWN via the external ports (see Fig. 9.7). Designing the system function of the RGWN is then mathematically equivalent to designing the S-matrix to yield a desired output, given a set of inputs.

Programming an optical function onto a network, according to the design principle described above, will first be demonstrated for a plasmonic 2×2 RGWN, in which the constituent MDM waveguides are allowed to differ in width, length, and contour. The device has eight terminals, numbered from 1 to 8, as illustrated in Fig. 9.7a. The input vector lists the complex amplitudes of the magnetic fields (H-fields) entering the network in the eight terminals, and, similarly, the output vector describes the

complex H-field amplitudes of the waves exiting the network through these same terminals.

The network S-matrix is assembled from the mathematical representation of its components according to the network layout. As a first step, a function library of mathematical representations is generated for all the possible network components (i.e., waveguides and X-junctions) using finite difference time domain (FDTD) full-wave electromagnetic simulations. Once this library is established, the RGWN S-matrix can be assembled according to the network layout. It is worth pointing out that the S-matrix calculation scheme is almost always found to be much faster than resolving the RGWN behavior from full-wave electromagnetic simulations, yet reproduces the same information about the network. This becomes significant for optimization tasks and especially as the network size increases.

To carry out this formalism, the two basic RGWN components (waveguides and X-junctions) need to first be represented mathematically. The waveguides are mathematically represented by their complex phase retardation, determined by the complex propagation constant of the wave and the waveguide length. The propagation constants are extracted from FDTD simulations for waveguides with various widths at different frequencies. The X-junctions, which are comprised of two intersecting waveguides with four terminals, are mathematically represented by a (4×4) S-matrix. For a given set of waveguide widths, the complex transmission coefficients of the X-junction ports are extracted from FDTD simulations by measuring the amplitude and phase of the wave transmitted to the different ports when excited from one of the terminals at a given wavelength.

The S-matrix of the 2×2 RGWN is then assembled from the mathematical representation of its constituent components according to the network layout [49]. When validating the field amplitude predictions of the S-matrix representation with FDTD simulations, less than 5% difference is found for various test cases. The two major contributions to this small deviation result from the interpolation between the parameter space points, where the library components were calculated, and from the error added when the waveguides are bent. For cases where no interpolation or waveguide

bending occurs, the FDTD results differ by only 1% from the S-matrix predictions. The ability to accurately predict the RGWN interference using S-matrix representation reduces the complicated task of programming a desired optical function of a RGWN into an efficient optimization of its S-matrix.

For example, the RGWN can be programmed by minimizing the difference between the actual network output and the desired one (for a given input), as the network parameter space is swept across the various waveguide widths and lengths. The optimization process then results in a set of network parameters that can be translated to a network layout and then validated with FDTD simulations.

9.6 Multi-Chroic Filters using RGWNs

The S-matrix programming method can be exemplified by designing a 2×2 RGWN to function as a dichroic router (Fig. 9.8a). Although simple in concept, the exercise of setting a passive device to have different functions at different wavelengths is quite instructive. Explicitly, the required function is to route two different wavelengths (λ_1 and λ_2) to a different set of ports (1 and 6 for λ_1 and 2 and 5 for λ_2) when the two bottom ports (7 and 8) are simultaneously excited with equal power. Mathematically, we can represent the device as an 8×8 S-matrix $\mathbf{S}(\lambda_1, \lambda_1)$ connecting the input and the output vectors. For both wavelengths, the input vector is nonzero for the bottom ports (i.e. **In**=(0,0,0,0,0,0,1,1)) and the desired output vectors would be **Out**(λ_1)=(1,0,0,0,0,1,0,0) for λ_1 and **Out**(λ_2)=(0,1,0,0,1,0,0,0) for λ_2. Because we do not have enough degrees of freedom in this small 2×2 network to exactly attain the desired outputs, we instead optimize the ratio of power going to the two sets of ports at the different wavelengths.

The optimization procedure is implemented in Matlab using the pre-calculated mathematical representation data set of the RGWN components obtained from full-field electromagnetic FDTD simulations excited with continuous wave sources (see illustration in Fig. 9).

The dichroic router network is defined by eight parameters: the length and width

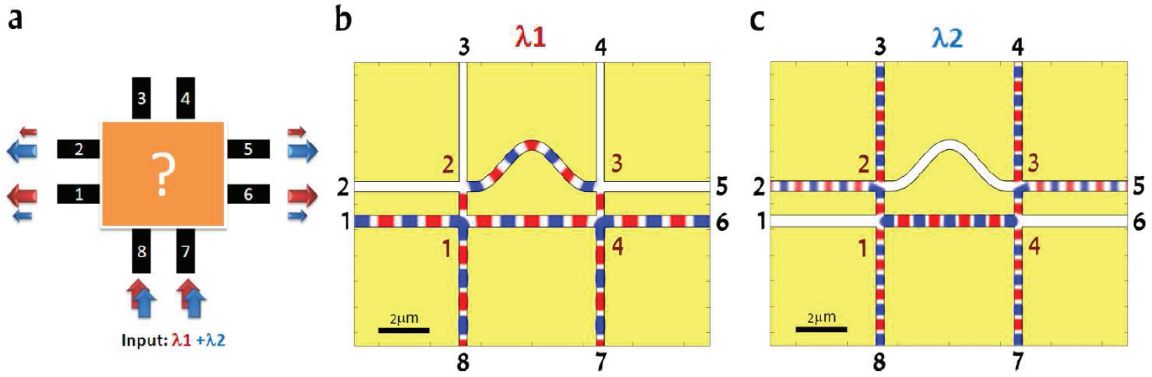

Figure 9.8: 2×2 RGWN programmed to function as a dichroic router: (a) schematic drawing, and (b,c) time snapshots of the H-field at the two operation frequencies [49].

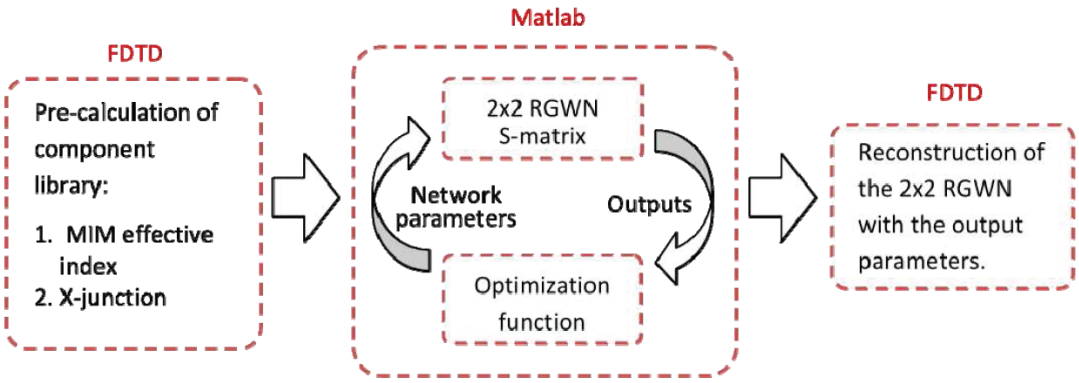

Figure 9.9: Flow chart of the RGWN S-matrix optimization procedure [49].

Waveguides	Width (μm)	Length (μm)
Lower	0.47	5.40
Side	0.31	1.34
Upper	0.38	6.60

Table 9.1: Set of optimized parameters for 2×2 RGWN dichroic router operating at λ_1=2 μm and λ_2=1.26 μm.

of the upper, lower, and side waveguides and the two wavelengths. The waveguide widths determine the effective index in the waveguides as well as the transmission coefficients of the X-junctions. The optimization procedure is conducted in Matlab by optimizing the ratio of power of the top and bottom set of sideways port for the two different wavelengths.

After defining the optimization function, we constrain the parameter space based on practical considerations. The parameter space includes the width and length of the upper, lower, and side waveguides, as well as the two wavelengths of operation (λ_1 and λ_2). We decrease the number of parameters to optimize by restricting the device to have left-right symmetry based on the desired operation. We restrain the design to operate in the infrared frequency range (λ_0 = 1.2–2.0 μm), where the material dispersion and loss are less pronounced than in the visible. Furthermore, the waveguide thickness is constrained to be small enough to only support the lowest order plasmonic mode (air gap widths 100-500 nm).

The optimization procedure yields the network parameters given in Table 9.1, which reveal that the required RGWN for color routing is distributed inhomogeneously.

When translating the optimized network parameters into the network layout, we learn that the upper waveguide is longer than the lower one, and therefore needs to be bent. Importing the resulting layout into FDTD, we obtain the steady state H-field distribution shown in Fig. 9.8b and c, which show time snap shots at the two operation wavelengths. The FDTD simulation results validate the S-matrix design, with λ_1 and λ_2 clearly routed to a different set of sideways ports as illustrated in Fig. 9.8b and c, respectively. From these FDTD results, it is also possible to observe

the build-up of local resonance inside the network, which results in the filtering out of the desired output ports. We note that the transmission ('3' and '4') and reflection ('7' and '8') ports from the device are not identically zero, since the device does not have enough degrees of freedom and were therefore not included in the optimization function.

The matrix representation can also be used to understand the interference conditions through which the RGWN accomplishes its desired function. From the known input vector and the network S-matrix, the wave complex amplitudes can be identified at any point in the network. For each wavelength, we resolve the excitation conditions of the X-junctions that have the ports that are to be filtered out. For example, for λ_1 to be filtered out from terminals '2' and '5', we examine the excitation conditions in X-junction '3', which has four terminals. Two of the terminals are external device ports ('4' and '5') and the other two are internal network terminals. There is no input signal incident on the two external ports, so it is the excitation conditions of the remaining two junction terminals that null the output in terminal '5'. Indeed, the excitation amplitudes of junction '3' obtained from the S-matrix representation are $0.23e^{-i0.21\pi}$ and $0.34e^{i0.64\pi}$, which are close in amplitude and $\sim \pi$ phase-shifted. This is consistent with the results from section 3, which show that when an X-junction is simultaneously excited π phase-shifted from two adjacent terminals, the two other terminals will be filtered out (Fig. 9.3a). The fact that the excitations are not exactly the same in amplitude and π phase-shifted is attributed to the additional constraints the design has on the other wavelength as well as the limitations imposed on the parameter space.

Similarly, the excitation conditions necessary for filtering out terminals '1' and '6' at λ_2 (Fig. 9.8b) are examined by focusing on the S-matrix amplitudes of X-junction '4'. In this case, there are three terminals being excited: the lower terminal of the X-junction (port '7') is given by the network excitation, so the excitation of the other two internal ports will determine the filtering out of port '6'. Intuitively, the condition to filter out terminal '6' will be simply a π phase-shifted excitation of the upper and lower terminals of junction '4', with zero excitation from the side port. From the case

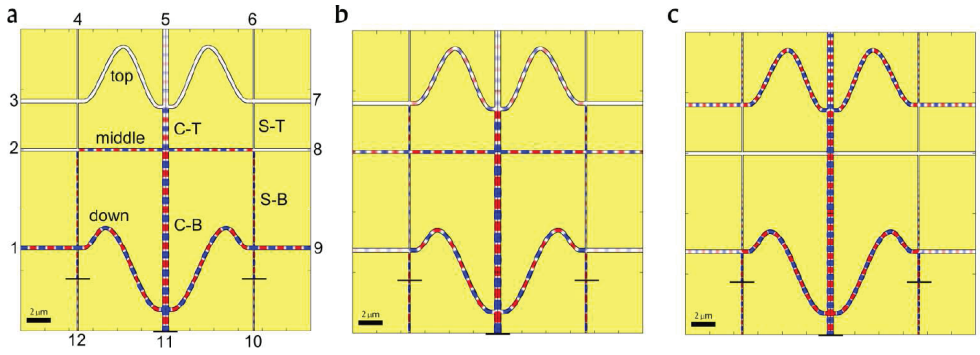

Figure 9.10: 3×3 RGWN programmed to function as a trichroic router. Time snapshots of the steady state H-field at the three operation frequencies [49]: a) λ_1, b)λ_2, c) λ_3.

of λ_1, we also know that additional constraints might cause a residual wave emerging from terminal '6', which could be compensated by a small amplitude excitation at the other side terminal of junction '4'. Indeed, the excitation amplitudes of junction '4' in the S-matrix representation are 1 in the lower terminal, $0.9e^{i0.82\pi}$ in the upper terminal, and $0.3e^{-i0.32\pi}$ in the side terminal.

To further exemplify the programmability of RGWNs via S-matrix formalism, we consider a 3×3 RGWN programmed to function as a trichroic router. In order to implement the more complex task of routing three wavelengths, we allow for more degrees of freedom in the network by increasing the number of components, effectively increasing the amount of data contained. The function is defined as an extension of the dichroic router, but here when the three bottom terminals are simultaneously excited at three different frequencies, the frequencies are filtered out to three different sets of side terminals, as illustrated in Fig. 9.10. The analysis results in the optimal RGWN parameters shown in Table 9.2.

It is interesting to note that the wavelengths are not mapped monotonically to the output terminals (i.e. from bottom/top ports as the wavelength increases/decreases), which would be the usual case for devices relying on material dispersion, such as a glass prism.

Waveguides		Width (μm)	Length (μm)
Vertical	center-bottom	0.45	13.25
	Side-Bottom	0.10	8.15
	Center-Top	0.45	3.55
	Side-Top	0.10	4.00
Horizontal	Top	0.29	12.80
	Middle	0.26	7.30
	Bottom	0.30	11.95

Table 9.2: Set of optimized parameters for 3×3 RGWN trichroic router operating at λ_1=1.59 μmm, λ_2=1.97 μm, and λ_3=1.23 μm.

9.7 Possible Implementations

The underlying physics and the working principles of the RGWNs were demonstrated in the previous sections with an idealized 2D implementation using MDM waveguides. However, for the same 2D network topology, as shown in Fig. 9.4, but implemented with 3D high aspect ratio Au-air channel plasmon waveguides [13], the observed wave dynamics are found to closely resemble that of the 2D MDM waveguide network, as studied with 3D full-field simulations. If the aspect ratio of the channel plasmon waveguide is high enough, the propagating mode within the channels strongly resembles the MDM gap plasmonic mode. This can, for instance, be seen in the measured quality factors of RGWNs comprised of channel plasmon waveguides (3D simulations) and MDM slot waveguides (2D simulations), which have Q-factor values of 82 and 83, respectively, at a wavelength of 1.5 μm. Furthermore, the two power splitting events that define the RGWN resonant state are similar for both the channel and MDM waveguides (Fig. 9.4).

The dispersion design in a volume can be addressed by 3D-RGWN topologies, for example, constructing an array of orthogonally intersecting 3D networks of coaxial Au-air waveguides aligned in a Cartesian grid (Fig. 9.11a). In this case, the four-arm X-junction element of the 2D network is replaced by a six-arm 3D junction element. Using 3D FDTD, we have verified that six-way equal power splitting occurs for pulsed excitation in a coaxial Au-air waveguide junction. Like for the 2D-RGWN, the dispersion of the infinitely large periodic 3D-RGWN is predominantly determined by

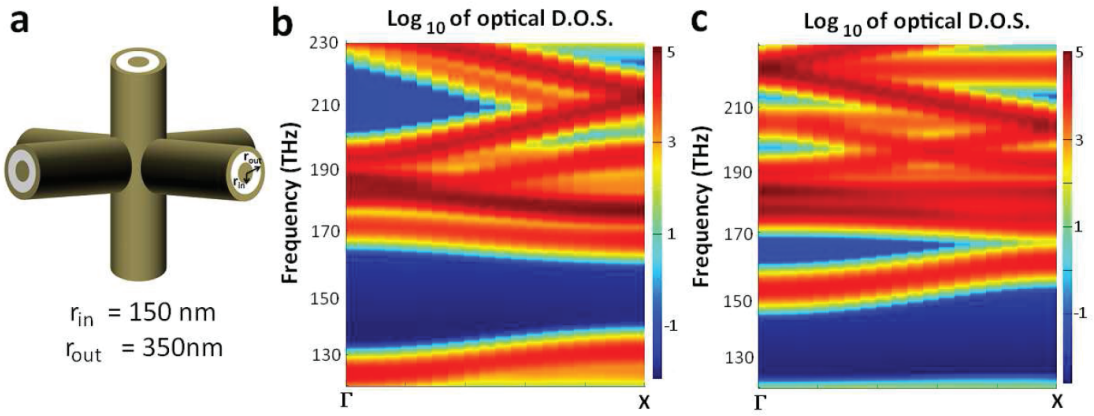

Figure 9.11: 3D RGWN: (a) rendering of a 3D RGWN building block (6-arm junction). (b, c) Optical DOS of an infinite 3D network spaced periodically with cubic periodic unit cell with different spacing [48].

the network parameters rather than the waveguide dispersion. This is demonstrated by the noticeable difference in the band diagrams (Fig. 9.5b and c) obtained for two networks comprised of the same waveguides but with different inter-node spacing.

9.8 Conclusions and Directions

RGWNs offer a different approach for designing dispersive photonic materials. Whereas photonic crystals rely on the formation of Bloch wave states by interference of waves diffracted from an array of periodic elements, a truly non-local phenomenon, RGWNs rely on the coherent superposition of power flowing along isolated waveguides and splitting at X-junctions. Furthermore, in photonic crystals, the interference pattern of the diffracted waves depends on the non-local periodic spatial arrangement of the diffracting elements, and in RGWNs it is the local network topology that determines the dispersion and resonance features. For example, in a RGWN, the coherent wave propagation through the network is determined only by the total path length along the waveguide and the phase shift added at a power splitting event, having no restriction on whether the waveguides are straight or curved. Metamaterials also feature a design approach based on the attributes of localized resonances, but their

dispersive properties do not depend on any length scale between resonant elements, thus differing substantially from RGWNs. Arrays of coupled resonator optical waveguides (CROWs) feature discrete identifiable resonators that act as the energy storage elements, and dispersion occurs as modes of adjacent resonators are evanescently coupled. By contrast, in RGWNs energy is not stored resonantly in discrete resonators, but rather in the network of waveguides that are designed to exhibit a collective resonant behavior.

The operation of RGWNs was demonstrated in this chapter using plasmonics, which allowed for a simple layout and broadband range of operation; however, this implementation also brought about substantial attenuation due to the fundamental loss of plasmonic modes. As indicated above, the plasmonic MDM modes used here have typical propagation lengths of about 50 microns due to metal loss. Since the RGWN scope is broader than the field of plasmonics, it calls for an all-dielectric implementation to mitigate the losses brought on by plasmonics. Implementing RGWNs using photonic circuitry would also address the coupling loss associated with the difference in the modal overlaps between the plasmonic modes in the RGWN and the interfacing dielectric optics.

This new design paradigm is based on different underlying physics and thus opens up new directions for the design of artificial optical materials and devices. Since the RGWN design relies on the interference of local waves, we can use these accessible design parameters to program optical functions directly onto the network. Furthermore, the constraints on the propagation and coupling of the local waves in RGWNs allow for the device operation to reduce to a simple mathematical representation using S-matrix formalism. This allows for the network programming to take the form of an optimization procedure over a relatively small parameter space. The RGWN S-matrix representation was demonstrated here where the inputs were given and the S-matrix of the device was designed to give a desired output (e.g., routing, mode converting). However, this formalism could be extended to different type of functions, such as sensing, in which the inputs are given and the output changes are monitored. In this chapter, dichroic and trichroic RGWN color routing was demonstrated as

a proof of concept; however, incorporating more components into the RGWN, and therefore increasing the possible degrees of freedom, could allow for more complex devices or, alternatively, for devices with enhanced performance. Furthermore, we exemplified the RGWN design paradigm using plasmonics, nesting a split element simply by intersecting waveguides; still the concept is broad, and implementing the concept using a photonic component could open new opportunities in the design of photonic circuitry devices.

Chapter 10

Silicon Coupled Plasmonic Nanocircuits: 4-way Power-Splitters and Resonant Networks

Abstract: *One of the most compelling aspects of plasmonics is the ability to confine electromagnetic radiation in subwavelength modes at metal/dielectric interfaces [108, 6] – a promising characteristic for miniaturizing photonic communications technology at the scale and density of electronics. However, in order to simultaneously achieve low waveguide propagation loss and high mode confinement, we require chip-based hybrid photonic/plasmonic circuits [67, 124] that feature (1) low-loss silicon photonic waveguides, (2) high-confinement plasmonic waveguide building blocks [10, 11, 50, 84, 57], and (3) methods for efficient mode coupling between them [134, 42, 50]. The v-groove waveguide configuration supports and confines channel slot plasmon polaritons (CPP) [84, 92, 50, 10] in a highly confined channel (similar to the TM metal/dielectric/metal plasmonic mode) [50, 33], which have been experimentally investigated by several groups [13, 12, 137, 138, 139]. However, care must be given to properly distinguish between CPP and the presence of the longer propagation length corner-bound surface plasmon polariton (SPP) mode that is also supported by the structure. In this work, we use near field scanning optical measurements (NSOM) to demonstrate that $\lambda_0 = 1520$ nm light can be coupled from conventional silicon-on-insulator ridge waveguides to subwavelength channel plasmon polariton waveguides*

with an efficiency of 10%*, consistent with FDTD calculations. By proper control of mode polarization in the silicon-on-insulator waveguide [15], we demonstrate that parasitic excitation of surface plasmon polaritons (SPPs) on the metal surface is suppressed, only exciting the desired CPP mode of the v-groove structure – serving as the perfect platform for designing truly subwavelength plasmonic nano-circuit devices such, as resonant guided wave networks (RGWNs) [48, 49]. RGWNs, through the use of isolated waveguides to accumulate phase and waveguide crossings (x-junction) to split power [51, 133], have been theoretically demonstrated to be programmable to serve as plasmonic resonators [48] and color routers [49]; however, they still remain to be experimentally demonstrated. In this work, using the Si-ridge coupled CPP waveguides as a platform, we also demonstrate that a 90-degree CPP waveguide crossing serves as an ultra-compact 4-way power-splitter. Furthermore, we demonstrate how the layout of these two elements, subwavelength isolated CPP waveguides and their crossings, can be designed to operate as a compact optical logic device [27, 53, 99] operating at telecommunication wavelengths. The work presented here not only demonstrates the integration of Si-photonics with truly subwavelength plasmonic waveguides [140] [15, 85, 118, 125], but also illustrates how the crossing of these plasmonic waveguides serve as ultra-compact 4-way power-splitters for plasmonic networks – forming the platform for next-generation truly subwavelength integrated plasmonic circuits.*

10.1 Introduction

With the size of transistors approaching the sub-nanometer scale and Si-based photonics pinned at the micrometer scale, due to the diffraction limit of light, we are unable to easily integrate the high transfer speeds of this comparably bulky technology with the increasingly smaller architecture of state-of-the-art chip technology. However, we find that we can bridge the gap between these two technologies by directly coupling electrons to photons through the use of dispersive metals in plasmonics [108, 6]. Doing so allows us to access surface electromagnetic wave excitations at metal/dielectric interfaces, a feature which both confines and enhances light in

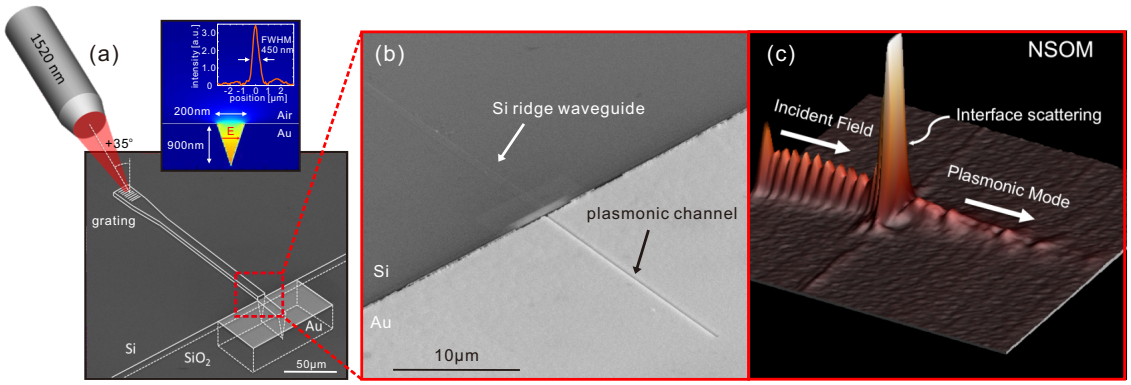

Figure 10.1: **Schematic of Si-photonic/v-groove plasmonic hybrid device and experiment.** (a) Scanning electron micrograph of hybrid device overlaid with schematic of fabricated device. Dashed lines represent geometry underneath the sample surface. Illumination condition used is schematically drawn in addition to the definition of positive and negative excitation angles for the grating coupler. Inset shows CPP mode profile calculated with an eigenmode solver (Lumerical FDTD v8.0) along with an experimental NSOM scan of the modal cross-section obtained at $\lambda_0 = 1520$ nm. (b) Close-up of Si-ridge/v-groove hybrid device fabricated with electron beam lithography and focused ion beam milling. (c) Resulting experimental NSOM scan of hybrid structure shown on (b) taken at $\lambda_0 = 1520$ nm.

subwavelength dimensions – two promising characteristics for the development of integrated chip technology. However, the confinement of light in plasmonics comes at the cost of loss in the metal, thus making plasmonics appealing for use as optical nanocircuits, but impractical for propagating light across long distances. Thus, we turn to hybrid photonic/plasmonic systems [67, 124] as a way of achieving both low loss propagation for inter-chip communication and high mode confinement for chip-size compatible processing. However, this configuration also requires efficient coupling between the silicon-based photonic and the metal-based plasmonic waveguides [134, 42, 50]. The photonic waveguide of choice is the Si-ridge waveguide, due to its lossless propagation lengths at telecommunication wavelengths, while that of the plasmonic waveguide is the v-groove configuration due to its supported plasmonic modes [84, 92, 50, 10].

In this work we bridge the gap between these two technologies by demonstrat-

ing efficient end-coupling of the diffraction limited Si-ridge waveguide platform with the subwavelength architecture of plasmonic v-groove waveguides at telecommunication frequencies (Fig. 10.1). The CPP mode of the v-groove waveguide is selectively coupled by proper control of the mode polarization of the silicon-on-insulator waveguide, suppressing the SPP mode that is also supported by the v-groove structure, with efficiencies upwards of $\sim 40\%$ for well optimized v-groove taper couplers. Furthermore, we demonstrate how a 90-degree CPP waveguide crossing operates as an ultra-compact equal-power-splitting element for developing truly subwavelength plasmonic nano-circuit devices [48]. Having these two basic plasmonic network elements, waveguides and splitters, we demonstrate the possible type of useful circuitries that subwavelength waveguides and splitters can be applied towards by studying a plasmonic network composed of four v-groove waveguides in an evenly spaced 2×2 configuration, which is shown to function as a compact optical logic device [27, 53, 99] at telecommunication wavelengths, routing different wavelengths in different on/off combinations to the same set of transmission ports.

10.2 Plasmonic Modes of the V-Groove Configuration

The v-groove channel plasmon waveguide configuration [84, 92, 50, 10] supports two fundamental plasmonic modes, the confined slot plasmon polariton (CPP) (Fig. 10.2a), residing in between the v-groove sidewalls, and the surface plasmon mode (SPP), which is a delocalized surface wave weakly bound at the top of the v-groove geometry by its corners (Fig. 10.2b). As evident from Figs. 10.2a,b, the CPP mode is characterized by E-field perpendicular to the v-groove sidewalls (similar to the TM metal/dielectric/metal plasmonic mode), while the SPP mode is characterized by E-field perpendicular to the top of the v-groove surface (similar to that of a regular SPP mode). Thus, we get that in addition to the difference in modal volume and confinement between these two modes, they are also characterized by orthogonal po-

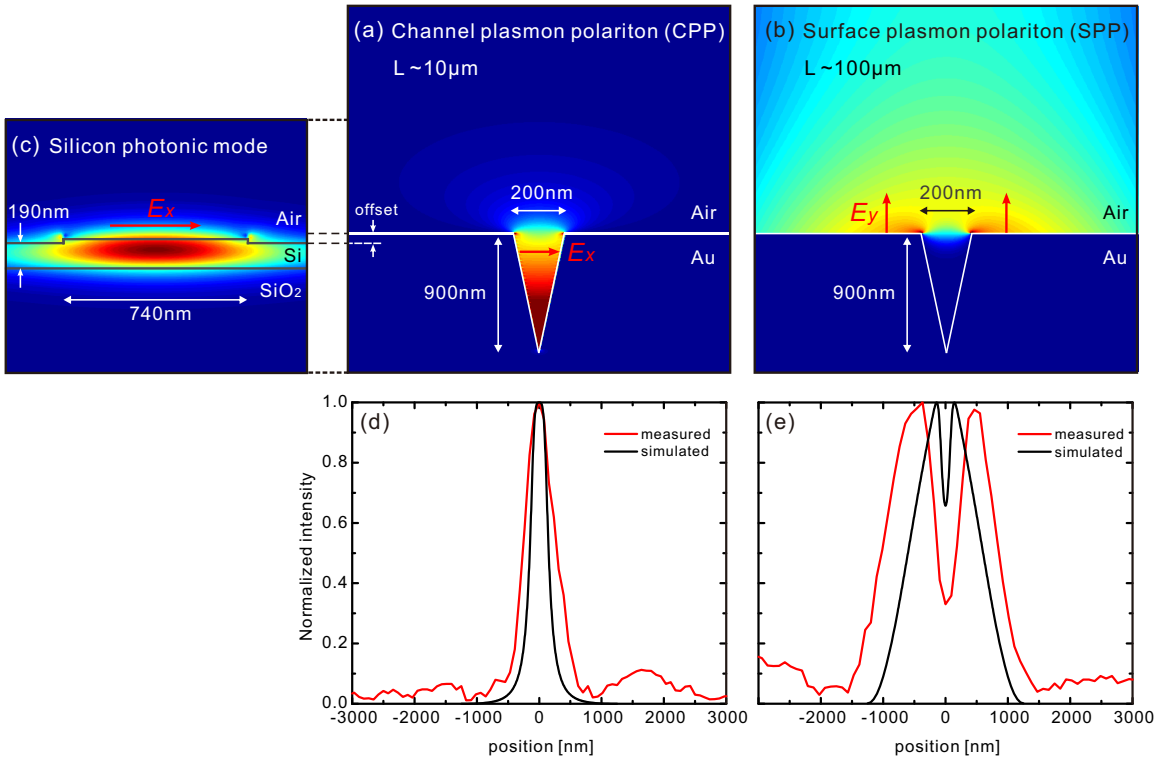

Figure 10.2: **Field distributions and near-field profiles of v-groove waveguide modes.** (a,b) Dominant field distributions obtained from eigenmode solver (Lumerical v8.0) calculations of CPP (E_x) and SPP (E_y) modes supported inside and near the surface of the v-groove configuration. (d,e) Corresponding field intensity distributions of CPP (d) and SPP (e) modes taken at a distance of 75 nm above the surface of the v-groove structure. Black line scans correspond to FDTD calculations, red line scans correspond to NSOM measurements. (c) Field distribution obtained from eigenmode solver calculations of TE mode in Si-ridge waveguide used to excite the CPP mode of the v-groove structure.

larizations, making for a convenient polarization-based selection rule between the two modes.

However, the confinement also manifests itself in the propagation length of the two modes, with the CPP mode having a propagation length of $L \sim 10\mu$m, an order of magnitude shorter than that of the SPP with $L > 100\mu$m. This propagation length difference means that if we were to simply try to end-couple to the v-groove waveguide configuration from freespace and measure the output down the v-groove waveguide past the scattering-dominated area, we would only be able detect the SPP mode, since it alone would have a propagation length long enough to survive past

the scattering dominated area. Thus, an alternative coupling scheme is required for selectively coupling into the CPP mode, preferably one which takes advantage of the polarization difference of the two supported v-groove modes and is compatible with current Si-photonics.

10.3 Mode Selectivity

To address this, we fabricated a hybrid Si-photonic/v-groove plasmonic chip consisting of 300-μm-long Si-ridge waveguides end-coupled to v-groove channel waveguides of variable length and layout (see Figs. 10.1a,b). The hybrid device was fabricated on an SOI chip with a 220 nm Si device layer on a 2 μm buried oxide (BOX) layer, using aligned-write electron beam lithography, reactive ion etching, electron beam evaporation, and focused ion beam milling. Arrays of 100×100-μm^2-size Au pads were defined by electron-beam lithography using PMMA resist (MicroChem), where the polymer was used both as a mask for SF_6-based plasma etching of the top Si layer and as a liftoff layer for metallization. To define the required metal depth for the v-groove waveguide configuration, the chips were successively etched using buffered hydrofluoric acid to remove approximately 1 μm of SiO_2 from the BOX layer prior to metallization. A 900-nm Au layer was deposited into the etched regions by electron-beam evaporation. The SOI waveguides were patterned with a ridge width of 740 nm using negative-tone electron-beam resist (Micro Resist Technology ma-N 2403), and the exposed Si was partially etched to a depth of 30 nm with a C_4F_8/O_2 plasma etching process. The v-groove channel waveguides were fabricated using multi-pass focused ion beam (FIB) milling on the Au pads at positions corresponding to that of the ridge waveguide (Fig. 10.1). An interface FIB 'cleaning' step was finally used to ensure maximum coupling from the Si-ridge waveguide to the v-groove waveguide, although this also added more separation between the waveguides. The resulting integrated structure then consisted of Si-ridge waveguide end-coupled to the v-groove Au waveguide with a waveguide separation of ∼500 nm, depending on the device, and a vertical offset of ∼ -50 nm.

Telecommunication wavelength light from a tunable diode laser was coupled into the Si-ridge waveguide through a grating coupler fabricated at the distal end from the Si-ridge/v-groove interface (see Fig. 10.1a,b), thus separating the incoupling scattering event from the excitation of the v-groove mode. With this configuration, we were able to access the either TE (E-field parallel to the substrate, see Fig. 10.2c) or TM (E-field perpendicular to the substrate) modes of the Si-ridge waveguide simply by controlling the angle of excitation, due to the different phase velocities of these two modes. By illuminating with $\lambda_0 = 1520$ nm light at an incident angle of $+35°$ (see Fig. 10.1a) and adjusting the polarization of the incident light, we were able to access the Si-ridge TE mode, which matches the dominant E-field distribution of the CPP mode (see Fig. 10.2c). The optical response of the system was measured using a Nanonics MV2000 NSOM, where a near field optical probe was scanned over the area of interest, collecting the near-field intensity information at the surface of the structure, and sending it to an InGaAs APD to be recorded.

A representative NSOM measurement of a Si-ridge waveguide coupled to a v-groove waveguide at 1520 nm is shown in Fig. 10.1c, demonstrating a very clear coupling intensity profile in going from the Si-ridge TE waveguide mode to the v-groove waveguide mode. The ridge waveguide shows a standing wave pattern due to the reflection, which happens at its facet end. Also, there is a clear scattering intensity field profile in the intermediate region between the waveguides. However, this scattering is predominantly out of plane, not affecting the field intensity of the mode excited in the v-groove waveguide.

10.4 CPP Waveguide Mode Properties

To determine the nature of the light coupled into the v-groove waveguide, we calculate its modal properties, namely its propagation length, effective index, and intensity full-width half-max (FWHM). The propagation length was calculated by coupling the Si-ridge waveguides into 30-μm-long v-groove waveguides and measuring the field decay of the light down their length (see Fig 10.3a). By fitting a decaying exponential

to the measured intensity decay, we measured a propagation length of $L \sim 10$ μm for $\lambda_0 = 1520$ nm, consistent with the FDTD calculated propagation length of the CPP mode (see Figs. 10.2a,b). The resulting data as as a function of wavelength is plotted in Fig. 10.3c, demonstrating good agreement with the calculated CPP eigenmode of the v-groove sructure.

Having found a coupled light propagation length of $L \sim 10$ μm for the v-groove waveguide, we proceeded to measure the effective mode index of the structure by observing the standing wave pattern of short 10-μm-long waveguides, which are on the order length of the propagation length (see Fig. 10.3a). The resulting interference patterns for different excitation wavelengths were fitted to a sinusoid, which results in the structure due to the reflection at the waveguide end. From this fit, we extract an effective index of $n = 1.05$ at 1520 nm, consistent with the index of a bound mode. The resulting data as a function of wavelength is plotted in Fig. 10.3d, demonstrating good agreement with the eigenmode of the CPP mode dispersion.

Furthermore, in addition to the differences in propagation lengths, the SPP and CPP modes also differ in their modal cross-sections, with the CPP having a single peak FWHM of only 300 nm, and the SPP having a double peak with a total FWHM of > 1 μm (see Figs. 10.2a,b). Thus, to definitively determine that we have selectively coupled into the CPP mode of the v-groove channel, we also measured the FWHM of the NSOM intensity obtained at cross-sections of the v-groove waveguide excited with TE polarized light from the Si waveguide. A typical line scan at 1520 nm is shown in Fig 10.2d (red curve), showing a single peak FWHM of $\sim$400nm, in agreement with the CPP mode of the structure.

Lastly, we demonstrate that we can also access the SPP mode of the structure by changing the excitation angle on the Si-ridge grating. By rotating the excitation angle to -35° (see Fig. 10.1a), we were able to access the TM mode of the Si-ridge waveguide, which matches the E-field profile of the SPP mode of the v-groove waveguide (Fig. 10.2b). By coupling in this manner, and measuring the resulting near field distribution along the v-groove waveguide structure, we obtain the line scan shown in Fig 10.2b, demonstrating that the measured mode is indeed double-peaked with a

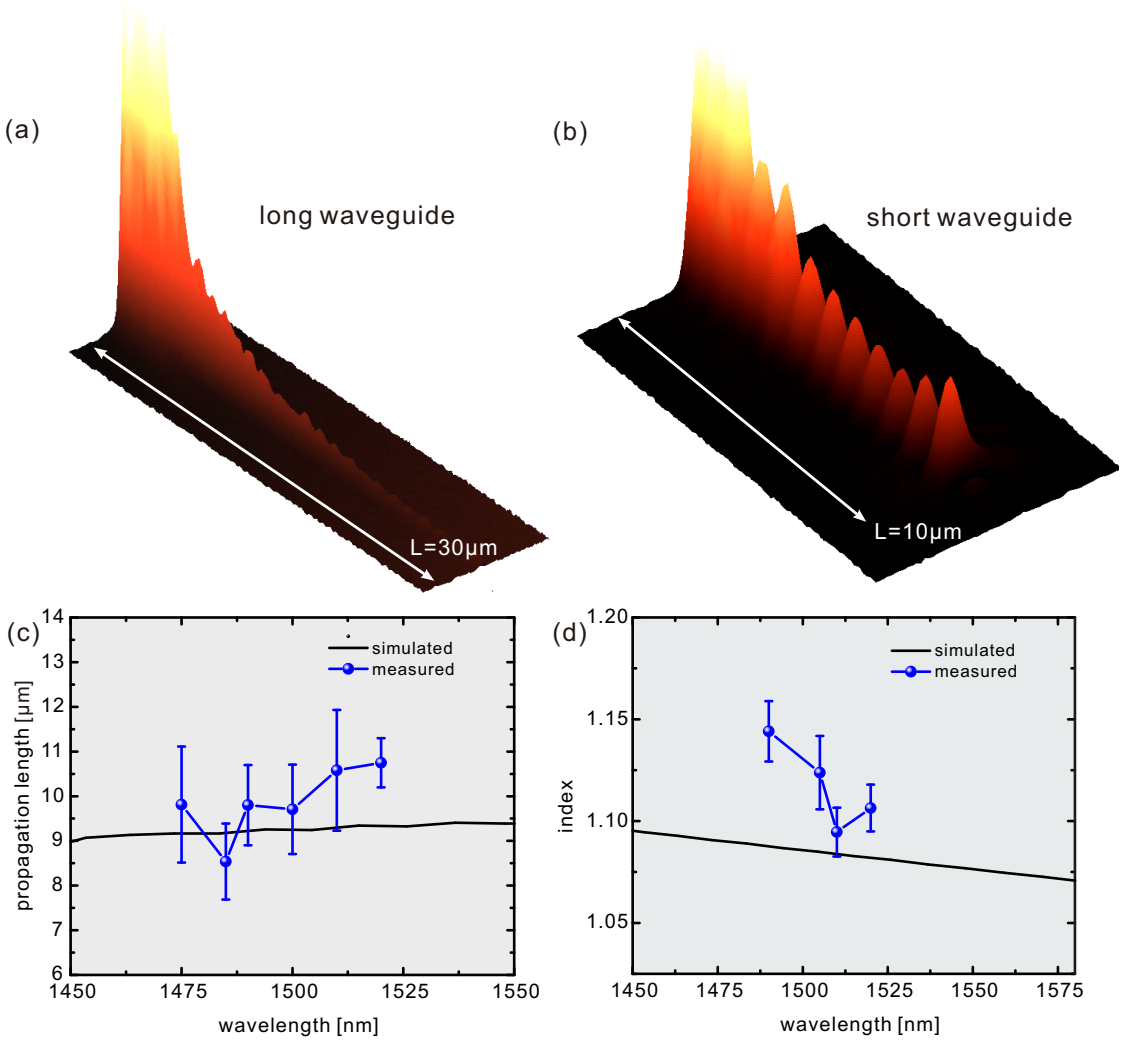

Figure 10.3: **NSOM images of CPP v-groove waveguide mode.** Experimental NSOM image taken at $\lambda_0 = 1520$ nm of (a) 30 μm and (d) 10 μm long v-groove waveguides. (c) Propagation length of v-groove waveguide mode obtained by FEM calculations (black line) and by fitting the decaying NSOM intensity of long v-groove waveguides (blue dotted data). (d) Effective index of v-grove waveguide mode extracted from eigenmode solver (Lumerical v8.0) calculations (black line) and the standing wave pattern observed in NSOM measurements of short v-groove waveguides (blue dotted points).

FWHM > 1 μm, consistent with the simulated field distribution of the SPP mode.

Thus, we have demonstrated that by proper control of the polarization in the Si-ridge structure, we can access either the CPP or SPP mode of the v-groove structure; however, only the CPP mode is truly subwavelength, lending itself as the perfect infrastructure for designing confined plasmonic circuitry such as ultra-compact resonant guided wave networks (RGWNs) [48, 51].

10.5 Ultracompact 4-Way Power-Splitters

Having verified that we can selectively couple into the subwavelength CPP mode of the v-groove structure, we use the v-groove platform to demonstrate their functionality as power splitting elements. Deriving from the concept of RGWNs, a power-splitting element in plasmonic representation can be engineered by the crossing of two subwavelength mode waveguides, termed x-junctions. In Fig. 10.4a, we show a scanning electron micrograph of such a structure, consisting of two 15-μm-long v-groove waveguides crossed at their centers at a 90° angle. The x-junction is excited from one of its ports with the $\lambda_0 = 1520$ nm TE mode of the Si waveguide, thus coupling into the CPP mode as demonstrated from the single waveguide measurements.

The resulting NSOM image of the x-junction is shown in Fig. 10.4b, from which we can clearly see that power is split amongst the four ports of the x-junction. In addition, we also observe a standing wave pattern in each of the x-junction arms, with that of the forward and sideways ports (relative to the excitation port) arising from the waveguide-end reflections, and that of the excitation port coming from the reflection at the x-junction. To extract the amount of power coupled into each port, we fit the intensity amplitudes of each arm at the onset of the x-junction, getting approximately equal power-splitting into each port at $\lambda_0 = 1520$ nm (see Fig. 10.4c). We note that although the x-junction scattering coefficients are complex in nature, we are only able to extract their amplitudes from intensity measurements, due to the non-interferometric nature of our measurements. Nevertheless, we determine the dispersion of the splitting coefficient amplitudes by varying the incident wavelength

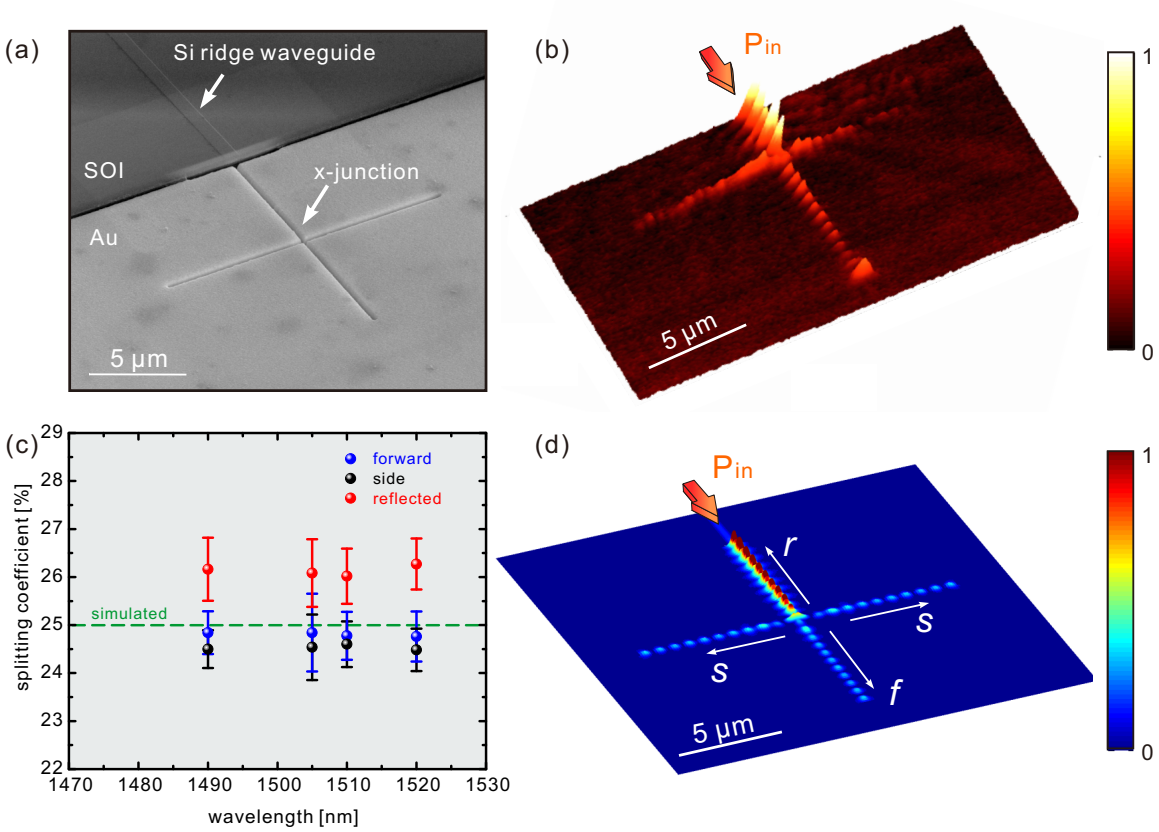

Figure 10.4: **Equal power-splitting x-junction plasmonic structure.** (a) Scanning electron micrograph of two v-groove waveguides crossed at 90°, forming an x-junction coupled from one of its ports by a Si-ridge waveguide. (b) NSOM image taken at $\lambda_0 = 1520$ nm of x-junction shown in (a). (c) Splitting parameters extracted from fitting the intensity pattern of the NSOM image shown in (b). (d) Simulated optical response of v-groove waveguide crossing excited through one of its ports with the CPP mode at $\lambda_0 = 1520$ nm.

and repeating the amplitude fitting routine described above. The resulting data as a function of wavelength is plotted in Fig. 10.4c, demonstrating that the splitting amplitude is fairly insensitive to wavelength over the wavelength range of 60 nm.

To substantiate our findings, we investigate the expected splitting amplitudes using FDTD, superimposed onto the measured data in Fig. 10.4c, with both sets in good agreement with each other. For visual comparison, in Fig. 10.4d, we also plot the simulated field intensity profile of a 200×900nm v-groove waveguide x-junction. A CPP mode is launched from one of the x-junction arms and the resulting steady state field is recorded at the surface of the structure. We observe from from Figs. 10.4b,d that both near field spectra are in good agreement of each other.

10.6 2×2 Plasmonic Logical Device

As a demonstration of the possible type of useful circuitries that subwavelength waveguides and splitters can be applied towards, we fabricated a plasmonic network composed of four 15-μm v-groove waveguides in a 2×2 configuration (see Fig. 10.5a), which is shown to operate as a compact optical logic device at telecommunication wavelengths, routing different wavelengths in different on/off combinations to the same set of transmission ports.

First, we investigate the device properties using FDTD, where we excite the bottom left port with a broadband CPP mode and monitor the output at the two top ports of the structure. From Figs. 10.6a-c, we see that 1670 nm light selectively routs to the left port (on/off configuration), 1570 nm routes to both ports (on/on configuration), and 1470 nm routes to neither (off/off configuration) – forming a wavelength selection logical device. The optical response of the ports of interest at the operation wavelengths is shown in Fig. 10.6d. The observed behavior is similar to that described in our previous work [49] where we design 2×2 and 3×3 resonators to function as color routers based on the complex scattering coefficients of the junctions and the phase accumulated by the isolated waveguides. There we found that the network parameters can be engineered to have a different set of resonances within the network for

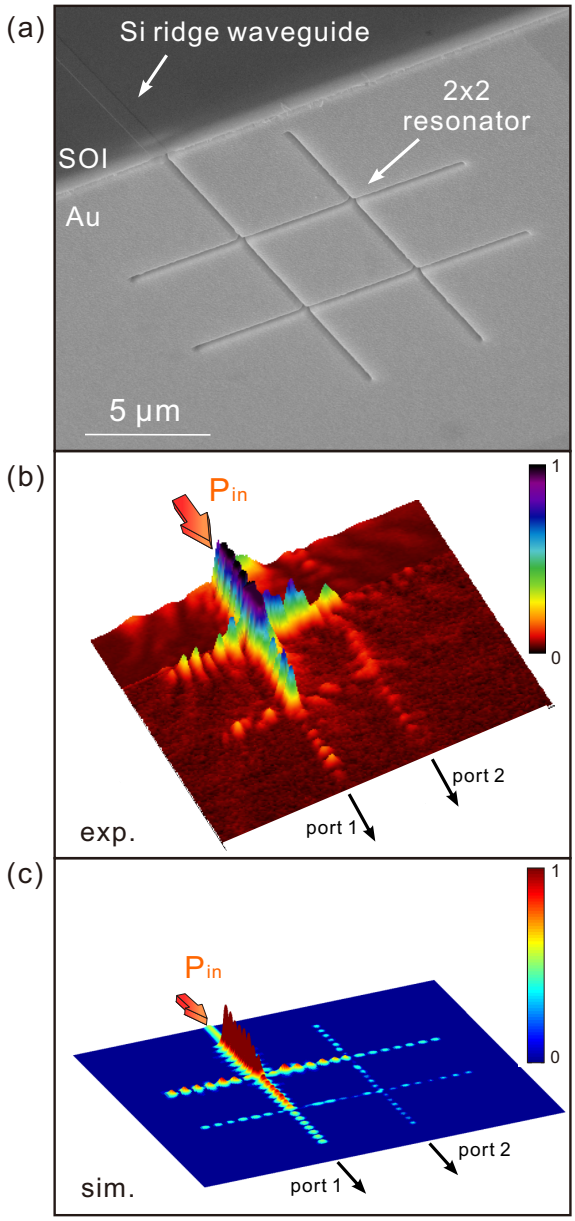

Figure 10.5: **2×2 RGWN optical logic device.** (a) Scanning electron micrograph of fabricated device consisting of four 15-μm-long waveguides in an evenly spaced 2×2 configuration, coupled from one of the arms with a Si-ridge waveguide. (d) Measured near field response of device shown in (a), when exciting it with $\lambda_0 = 1520$ nm TE polarized light from the Si-ridge waveguide. The output ports of interest are labeled for reference. (c) Simulated optical response of device shown in (a) when exciting one of its arms with the CPP mode at $\lambda_0 = 1520$ nm.

different wavelengths, causing light to route to different waveguide ports for different wavelengths.

The fabricated device is shown in Fig. 10.5a, coupled from one of its ports by the Si-ridge waveguide mode, which excites the CPP mode of the v-groove structure. The resulting NSOM intensity pattern for $\lambda_0 = 1505$ nm is shown in Fig. 10.5b, from which we can see that the network resonances result in selectively coupling into port 1 of the structure (on/off configuration). For comparison, we also plot in Fig. 10.5c the corresponding FDTD calculated field intensity at the surface of the structure, which shows to be in good agreement with the measurement. In Fig. 10.6e we plot the optical response of the ports of interest at the operation wavelength of $\lambda_0 = 1505$ nm.

10.7 Coupling Efficiency

Having demonstrated that hybrid Si-ridge coupled v-groove structures can serve as a useful platform for selectively coupling into the subwavelength CPP mode, which we have further demonstrated to serve as ideal elements for formulating power-splitters and logical devices, we proceed to investigate the coupling efficiencies associated in going from the photonic Si-ridge waveguide mode to the subwavelength plasmonic v-groove mode [134, 42, 50]. Previous work has been focused on the coupling to the SPP mode of various structures, including DLSPP [66, 15, 90], v-groove mode structures [13, 12, 137, 138, 139], and hybrid plasmo-photonic modes [76]. Here we investigate the coupling properties in going from the large modal volume of a Si-ridge waveguide to a subwavelength CPP waveguide mode. The modal volume of the Si-ridge TE mode is plotted in Fig. 10.2c, alongside that of the v-groove CPP mode 10.2d. From these images, we can see that the CPP mode is $\sim$1/5 the transverse size of the Si-ridge TE mode, so that we should expect to have coupling efficiencies on this order.

However, because the separation between the v-groove and Si-ridge waveguides is nonzero due to fabrication limitations, this coupling efficiency is expected to be

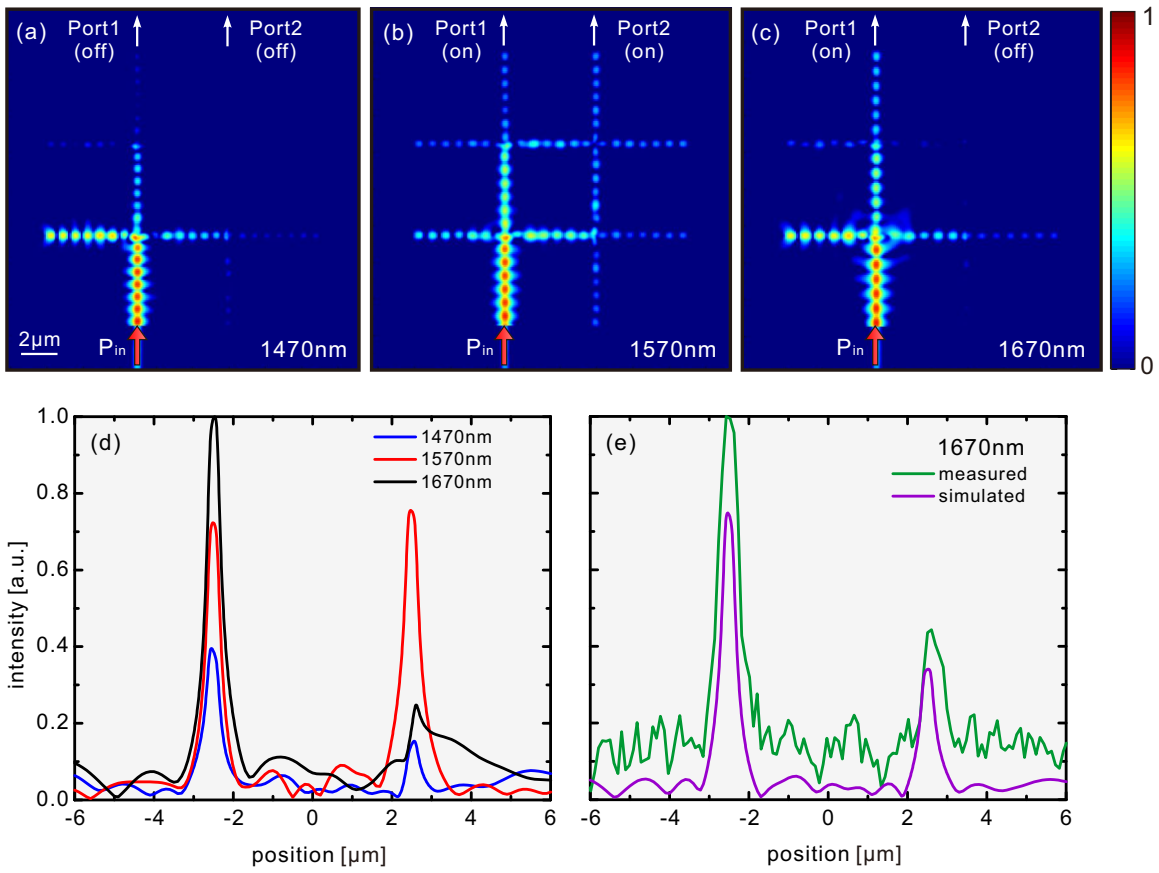

Figure 10.6: **2×2 RGWN logic device operation.** (a-c) Simulated near field intensity of plasmonic logic device consisting of four 15-μm-long v-groove waveguides in a 2×2 configuration, excited with the CPP mode from the bottom left port at (a) $\lambda_0 = 1470$ nm, (b) $\lambda_0 = 1570$ nm, and (c) $\lambda_0 = 1670$ nm. The top ports of interest are labeled along with their on/off state configuration based on the excitation wavelength. (d) Intensity cross-sections taken at top output ports of interest at the excitation wavelengths shown in (a-c). (e) Measured and simulated intensity response at the output ports of interest for $\lambda_0 = 1505$ nm.

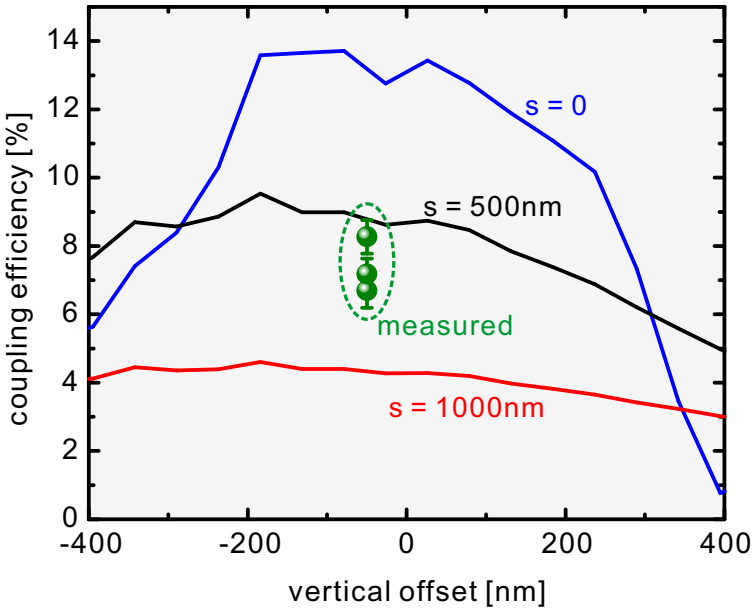

Figure 10.7: **Coupling efficiency as a function of waveguide position at λ_0 = 1520 nm.** Horizontal axis corresponds to vertical offset between Si-ridge and v-groove waveguides relative to their surface tops. The three dotted curves correspond to three different waveguide separations, with the blue corresponding to zero separation, black to 500 nm separation, and red to 1000 nm separation. The green dotted data corresponds to coupling efficiencies extracted from NSOM measurements for wavelengths λ_0 = 1500, 1510, and 1520 nm.

smaller than their modal volume ratios. The exact efficiency will, of course, depend on the amount of light radiated at the interface, along with the number of accessible modes that couple light from the Si-ridge to the CPP waveguide. However, since we are coupling through a volume of freespace, there are an infinite number of freespace modes which contribute to the coupling, making this calculation difficult to do analytically. Thus, we reduce the complexity of the calculation by resorting to FDTD simulations, in which we launch light from an aligned Si-ridge waveguide to a v-groove waveguide separated by some distance and having different offsets relative to their top surfaces.

Thus, we calculate the coupling efficiency simply by monitoring the amount of power transmitted into the v-groove waveguide when excited by the TE Si-ridge mode at 1520 nm as a function of the waveguide separation and vertical offset. The resulting transmission data is shown in Fig. 10.7, from which we can see that, indeed, for a zero separation, we get a maximum coupling efficiency of $\sim$14% at an offset of ~ -100 nm, which is only slightly lower than expected based on their modal volumes alone. However, we see that this efficiency quickly drops as the separation is increased, going down to $< 10\%$ for 500 nm separation, and $< 5\%$ for 1000 nm separation. From FIB cross-sections of the fabricated device, we get that the waveguides are separated by $\sim$500nm and offset by $\sim$ -50nm, thus placing our devices in the 10% theoretical range for 1520 nm light.

From NSOM measurements of the Si-ridge/v-groove interface at 1520 nm, the amount of light coupled from the Si-ridge waveguide into the v-groove CPP waveguide can be calculated by measuring the near field intensity distribution at the Si-ridge/v-groove waveguide junction and using FDTD to relate the intensity amplitudes to the power in the waveguides. By comparing the intensity amplitudes before the junction, which includes contributions from the incoming and reflected photonic modes of the structure, and after the junction, which includes the amount coupled into the CPP waveguide mode, we calculate a coupling efficiency of $\sim$8%, consistent with FDTD calculated values for similar geometries (see Fig. 10.7, green dotted data). We measure the wavelength-dependent coupling efficiencies by varying the excitation wavelength

between 1490-1520 nm and repeating the power coupling calculation for the resulting NSOM images. The resulting data is shown in Fig 10.7, showing coupling efficiencies in the 7-8% range.

10.8 Conclusion

In this work, we have demonstrated how a hybrid Si-photonic/v-groove plasmonic platform can serve as an efficient platform for designing integrated optical circuits exhibiting both the low loss propagation of Si photonics for long distance data transfer, and the compact subwavelength advantages of the confined plasmonic v-groove modes for designing compact optical devices. Furthermore, we have demonstrated how we can use this platform to selectively couple into the CPP v-groove waveguide mode, discarding the SPP mode based on the polarization of the incident light. The coupling efficiencies demonstrated here, although not high, are in good agreement with the theoretical values for direct coupling – demonstrating that for the geometry parameters of the reported configuration, our coupling in near ideal. Lastly, we have shown how, once coupled into the CPP mode, it can be used as a subwavelength platform for designing ultracompact power-splitters and logic devices, just two examples of what is possible with the design of waveguides and power-splitters in integrated subwavelength plasmonic circuitry.

Bibliography

[1] Surface plasmon resurrection. *Nat Photon*, 6(11):707–707, 11 2012.

[2] A. Alu and N. Engheta. Multifrequency optical invisibility cloak with layered plasmonic shells. *Physical Review Letters*, 100(11):113901, 2008.

[3] A. Alu, M. G. Silveirinha, A. Salandrino, and N. Engheta. Epsilon-near-zero metamaterials and electromagnetic sources: Tailoring the radiation phase pattern. *Physical Review B*, 75(15):155410, 2007.

[4] H. A. Atwater and A. Polman. Plasmonics for improved photovoltaic devices. *Nature materials*, 9(3):205–213, 2010.

[5] F. I. Baida, A. Belkhir, D. Van Labeke, and O. Lamrous. Subwavelength metallic coaxial waveguides in the optical range: Role of the plasmonic modes. *Physical Review B*, 74(20):205419, 2006.

[6] W. L. Barnes, A. Dereux, and T. W. Ebbesen. Surface plasmon subwavelength optics. *Nature*, 424(6950):824–830, 2003.

[7] W. L. Barnes, W. A. Murray, J. Dintinger, E. Devaux, and T. W. Ebbesen. Surface plasmon polaritons and their role in the enhanced transmission of light through periodic arrays of subwavelength holes in a metal film. *Physical Review Letters*, 92(10):107401, 2004.

[8] P. Berini. Plasmon-polariton modes guided by a metal film of finite width. *Optics Letters*, 24(15):1011–1013, 1999.

[9] P. Berini and I. De Leon. Surface plasmon-polariton amplifiers and lasers. *Nature Photonics*, 6(1):16–24, 2011.

[10] S. I. Bozhevolnyi. Effective-index modeling of channel plasmon polaritons. *Opt. Express*, 14(20):9467–9476, Oct 2006.

[11] S. I. Bozhevolnyi and J. Jung. Scaling for gap plasmon based waveguides. *Opt. Express*, 16(4):2676–2684, Feb 2008.

[12] S. I. Bozhevolnyi, V. S. Volkov, E. Devaux, and T. W. Ebbesen. Channel plasmon-polariton guiding by subwavelength metal grooves. *Phys. Rev. Lett.*, 95:046802, Jul 2005.

[13] S. I. Bozhevolnyi, V. S. Volkov, E. Devaux, J.-Y. Laluet, and T. W. Ebbesen. Channel plasmon subwavelength waveguide components including interferometers and ring resonators. *Nature*, 440(7083):508–511, 03 2006.

[14] J. Bravo-Abad, A. Degiron, F. Przybilla, C. Genet, F. Garcia-Vidal, L. Martin-Moreno, and T. Ebbesen. How light emerges from an illuminated array of subwavelength holes. *Nature Physics*, 2(2):120–123, 2006.

[15] R. M. Briggs, J. Grandidier, S. P. Burgos, E. Feigenbaum, and H. A. Atwater. Efficient coupling between dielectric-loaded plasmonic and silicon photonic waveguides. *Nano Letters*, 10(12):4851–4857, 2010.

[16] A. G. Brolo, S. C. Kwok, M. D. Cooper, M. G. Moffitt, C.-W. Wang, R. Gordon, J. Riordon, and K. L. Kavanagh. Surface plasmon-quantum dot coupling from arrays of nanoholes. *The Journal of Physical Chemistry B*, 110(16):8307–8313, 2006.

[17] S. P. Burgos, R. de Waele, A. Polman, and H. A. Atwater. A single-layer wide-angle negative-index metamaterial at visible frequencies. *Nature Materials*, 9(5):407–412, 2010.

[18] W. Cai, U. K. Chettiar, A. V. Kildishev, and V. M. Shalaev. Optical cloaking with metamaterials. *Nature Photonics*, 1(4):224–227, 2007.

[19] P. Catrysse and B. Wandell. Integrated color pixels in 0.18-mu m complementary metal oxide semiconductor technology. *Journal of the Optical Society of America a-Optics Image Science and Vision*, 20(12):2293–2306, 2003.

[20] C. Chen, A. De Castro, and Y. Shen. Surface-enhanced second-harmonic generation. *Physical Review Letters*, 46(2):145–148, 1981.

[21] Q. Chen, D. Chitnis, K. Walls, T. D. Drysdale, S. Collins, and D. R. S. Cumming. CMOS photodetectors integrated with plasmonic color filters. *Ieee Photonics Technology Letters*, 24(3):197–199, 2012.

[22] Q. Chen and D. R. S. Cumming. High transmission and low color cross-talk plasmonic color filters using triangular-lattice hole arrays in aluminum films. *Optics Express*, 18(13):14056–14062, 2010.

[23] Q. Chen, D. Das, D. Chitnis, K. Walls, T. D. Drysdale, S. Collins, and D. R. S. Cumming. A CMOS image sensor integrated with plasmonic colour filters. *Plasmonics*, 7(4):695–699, 2012.

[24] Y. J. Chen and G. M. Carter. Measurement of third order nonlinear susceptibilities by surface plasmons. *Applied Physics Letters*, 41(4):307–309, 1982.

[25] U. K. Chettiar, A. V. Kildishev, H.-K. Yuan, W. Cai, S. Xiao, V. P. Drachev, and V. M. Shalaev. Dual-band negative index metamaterial: double negative at 813nm and single negative at 772nm. *Optics Letters*, 32(12):1671–1673, 2007.

[26] C. Clavero, K. Yang, J. Skuza, and R. Lukaszew. Magnetic field modulation of intense surface plasmon polaritons. *Optics Express*, 18(8):7743–7752, 2010.

[27] M. Cohen, Z. Zalevsky, and R. Shavit. Towards integrated nanoplasmonic logic circuitry. *Nanoscale*, pages –, 2013.

[28] F. de León-Pérez, F. J. García-Vidal, and L. Martín-Moreno. Role of surface plasmon polaritons in the optical response of a hole pair. *Physical Review B*, 84(12):125414, 2011.

[29] R. de Waele, S. P. Burgos, H. A. Atwater, and A. Polman. Negative refractive index in coaxial plasmon waveguides. *Optics Express*, 18(12):12770–12778, 2010.

[30] R. de Waele, S. P. Burgos, A. Polman, and H. A. Atwater. Plasmon dispersion in coaxial waveguides from single-cavity optical transmission measurements. *Nano letters*, 9(8):2832–2837, 2009.

[31] R. de Waele, S. P. Burgos, A. Polman, and H. A. Atwater. Plasmon dispersion in coaxial waveguides from single-cavity optical transmission measurements. *Nano Letters*, 9(8):2832–2837, 2009.

[32] R. de Waele, A. F. Koenderink, and A. Polman. Tunable nanoscale localization of energy on plasmon particle arrays. *Nano Letters*, 7(7):2004–2008, 2007.

[33] J. A. Dionne, L. A. Sweatlock, H. A. Atwater, and A. Polman. Plasmon slot waveguides: Towards chip-scale propagation with subwavelength-scale localization. *Physical Review B*, 73(3):035407, 2006.

[34] J. A. Dionne, E. Verhagen, A. Polman, and H. A. Atwater. Are negative index materials achievable with surface plasmon waveguides? A case study of three plasmonic geometries. *Opt. Express*, 16(23):19001–19017, Nov 2008.

[35] H. Ditlbacher, A. Hohenau, D. Wagner, U. Kreibig, M. Rogers, F. Hofer, F. R. Aussenegg, and J. R. Krenn. Silver nanowires as surface plasmon resonators. *Physical Review Letters*, 95(25):257403, 2005.

[36] G. Dolling, C. Enkrich, M. Wegener, C. M. Soukoulis, and S. Linden. Simultaneous negative phase and group velocity of light in a metamaterial. *Science*, 312(5775):892–894, 2006.

[37] G. Dolling, M. Wegener, and S. Linden. Realization of a three-functional-layer negative-index photonic metamaterial. *Optics Letters*, 32(5):551–553, 2007.

[38] G. Dolling, M. Wegener, C. M. Soukoulis, and S. Linden. Negative-index metamaterial at 780 nm wavelength. *Optics Letters*, 32(1):53–55, 2007.

[39] T. W. Ebbesen, H. J. Lezec, H. F. Ghaemi, T. Thio, and P. A. Wolff. Extraordinary optical transmission through sub-wavelength hole arrays. *Nature*, 391(6668):667–669, 1998.

[40] F. Eftekhari, C. Escobedo, J. Ferreira, X. Duan, E. M. Girotto, A. G. Brolo, R. Gordon, and D. Sinton. Nanoholes as nanochannels: flow-through plasmonic sensing. *Analytical chemistry*, 81(11):4308–4311, 2009.

[41] A. Eftekharian, H. Atikian, and A. H. Majedi. Plasmonic superconducting nanowire single photon detector. *Optics Express*, 21(3):3043–3054, 2013.

[42] A. Emboras, R. M. Briggs, A. Najar, S. Nambiar, C. Delacour, P. Grosse, E. Augendre, J. M. Fedeli, B. de Salvo, H. A. Atwater, and R. E. de Lamaestre. Efficient coupler between silicon photonic and metal-insulator-silicon-metal plasmonic waveguides. *Applied Physics Letters*, 101(25):251117, 2012.

[43] S. Fan, P. Villeneuve, J. Joannopoulos, and H. Haus. Channel drop filters in photonic crystals. *Optics Express*, 3(1):4–11, 1998.

[44] W. J. Fan, S. Zhang, B. Minhas, K. J. Malloy, and S. R. J. Brueck. Enhanced infrared transmission through subwavelength coaxial metallic arrays. *Physical Review Letters*, 94(3):033902, 2005.

[45] N. Fang, H. Lee, C. Sun, and X. Zhang. Sub-diffraction-limited optical imaging with a silver superlens. *Science*, 308(5721):534–537, 2005.

[46] N. Fang and X. Zhang. Imaging properties of a metamaterial superlens. *Applied Physics Letters*, 82(2):161–163, 2003.

[47] E. Feigenbaum and H. Atwater. Dielectric based resonant guided wave networks. *Optics Express*, 20(10):10674–10683, 2012.

[48] E. Feigenbaum and H. A. Atwater. Resonant guided wave networks. *Physical review letters*, 104(14):147402, 2010.

[49] E. Feigenbaum, S. Burgos, and H. Atwater. Programming of inhomogeneous resonant guided wave networks. *Optics Express*, 18(25):25584–25595, 2010.

[50] E. Feigenbaum and M. Orenstein. Modeling of complementary (void) plasmon waveguiding. *Journal of Lightwave Technology*, 25(9):2547–2562, 2007.

[51] E. Feigenbaum and M. Orenstein. Perfect 4-way splitting in nano plasmonic x-junctions. *Optics Express*, 15(26):17948–17953, 2007.

[52] E. Feigenbaum and M. Orenstein. Ultrasmall volume plasmons, yet with complete retardation effects. *Physical Review Letters*, 101(16):163902, 2008.

[53] Y. Fu, X. Hu, C. Lu, S. Yue, H. Yang, and Q. Gong. All-optical logic gates based on nanoscale plasmonic slot waveguides. *Nano Letters*, 12(11):5784–5790, 2013/05/14 2012.

[54] H. Gao, J. Henzie, and T. W. Odom. Direct evidence for surface plasmon-mediated enhanced light transmission through metallic nanohole arrays. *Nano letters*, 6(9):2104–2108, 2006.

[55] F. Garcia-Vidal, L. Martin-Moreno, and J. Pendry. Surfaces with holes in them: new plasmonic metamaterials. *Journal of optics A: Pure and applied optics*, 7(2):S97, 2005.

[56] H. F. Ghaemi, T. Thio, D. E. Grupp, T. W. Ebbesen, and H. J. Lezec. Surface plasmons enhance optical transmission through subwavelength holes. *Physical Review B*, 58(11):6779–6782, 1998.

[57] D. K. Gramotnev and S. I. Bozhevolnyi. Plasmonics beyond the diffraction limit. *Nat Photon*, 4(2):83–91, 02 2010.

[58] M. I. Haftel, C. Schlockermann, and G. Blumberg. Enhanced transmission with coaxial nanoapertures: Role of cylindrical surface plasmons. *Physical Review B*, 74(23):235405, 2006.

[59] M. I. Haftel, C. Schlockermann, and G. Blumberg. Role of cylindrical surface plasmons in enhanced transmission. *Applied Physics Letters*, 88(19):193104, 2006.

[60] C. Hubert, A. Rumyantseva, G. Lerondel, J. Grand, S. Kostcheev, L. Billot, A. Vial, R. Bachelot, P. Royer, S. H. Chang, S. K. Gray, G. P. Wiederrecht, and G. C. Schatz. Near-field photochemical imaging of noble metal nanostructures. *Nano Letters*, 5(4):615–619, 2005.

[61] Y. Inaba, M. Kasano, K. Tanaka, and T. Yamaguchi. Degradation-free MOS image sensor with photonic crystal color filter. *Ieee Electron Device Letters*, 27(6):457–459, 2006.

[62] D. Inoue, A. Miura, T. Nomura, H. Fujikawa, K. Sato, N. Ikeda, D. Tsuya, Y. Sugimoto, and Y. Koide. Polarization independent visible color filter comprising an aluminum film with surface-plasmon enhanced transmission through a subwavelength array of holes. *Applied Physics Letters*, 98(9):093113, 2011.

[63] Z. Jacob, L. V. Alekseyev, and E. Narimanov. Optical hyperlens: Far-field imaging beyond the diffraction limit. *Optics Express*, 14(18):8247–8256, 2006.

[64] P. B. Johnson and R. W. Christy. Optical constants of noble metals. *Physical Review B*, 6(12):4370–4379, 1972.

[65] A. F. Koenderink, J. V. Hernandez, F. Robicheaux, L. D. Noordam, and A. Polman. Programmable nanolithography with plasmon nanoparticle arrays. *Nano Letters*, 7(3):745–749, 2007.

[66] A. V. Krasavin and A. V. Zayats. Passive photonic elements based on dielectric-loaded surface plasmon polariton waveguides. *Applied Physics Letters*, 90(21):211101, 2007.

[67] B. Lau, M. A. Swillam, and A. S. Helmy. Hybrid orthogonal junctions: wideband plasmonic slot-silicon waveguide couplers. *Opt. Express*, 18(26):27048–27059, Dec 2010.

[68] E. Laux, C. Genet, T. Skauli, and T. Ebbesen. Plasmonic photon sorters for spectral and polarimetric imaging. *Nature Photonics*, 2(3):161–164, 2008.

[69] H.-S. Lee, Y.-T. Yoon, S.-S. Lee, S.-H. Kim, and K.-D. Lee. Color filter based on a subwavelength patterned metal grating. *Optics Express*, 15(23):15457–15463, 2007.

[70] H. J. Lezec, J. A. Dionne, and H. A. Atwater. Negative refraction at visible frequencies. *Science*, 316(5823):430–432, 2007.

[71] H. J. Lezec and T. Thio. Diffracted evanescent wave model for enhanced and suppressed optical transmission through subwavelength hole arrays. *Optics Express*, 12(16):3629–3651, 2004.

[72] B. Little, S. Chu, H. Haus, J. Foresi, and J. Laine. Microring resonator channel dropping filters. *Journal of Lightwave Technology*, 15(6):998–1005, 1997.

[73] R. Liu, C. Ji, J. J. Mock, J. Y. Chin, T. J. Cui, and D. R. Smith. Broadband ground-plane cloak. *Science*, 323(5912):366–369, 2009.

[74] Y. Liu, G. Bartal, and X. Zhang. All-angle negative refraction and imaging in a bulk medium made of metallic nanowires in the visible region. *Optics Express*, 16(20):15439–15448, 2008.

[75] V. Lomakin, Y. Fainman, Y. Urzhumov, G. Shvets, et al. Doubly negative metamaterials in the near infrared and visible regimes based on thin film nanocomposites. *Opt. Express*, 14(23):11164–11177, 2006.

[76] F. Lou, Z. Wang, D. Dai, L. Thylen, and L. Wosinski. Experimental demonstration of ultra-compact directional couplers based on silicon hybrid plasmonic waveguides. *Applied Physics Letters*, 100(24):241105, 2012.

[77] K. F. MacDonald, Z. L. Sámson, M. I. Stockman, and N. I. Zheludev. Ultrafast active plasmonics. *Nature Photonics*, 3(1):55–58, 2008.

[78] R. Marani, A. D'Orazio, V. Petruzzelli, S. Rodrigo, L. Martin-Moreno, F. Garcia-Vidal, and J. Bravo-Abad. Gain-assisted extraordinary optical transmission through periodic arrays of subwavelength apertures. *New Journal of Physics*, 14:013020, 2012.

[79] D. Marcuse. *Light transmission optics*. Van Nostrand Reinhold, New York, 1972.

[80] L. Martin-Moreno, F. Garcia-Vidal, H. Lezec, K. Pellerin, T. Thio, J. Pendry, and T. Ebbesen. Theory of extraordinary optical transmission through subwavelength hole arrays. *Physical Review Letters*, 86(6):1114–1117, 2001.

[81] M. Meier and A. Wokaun. Enhanced fields on large metal particles - dynamic depolarization. *Optics Letters*, 8(11):581–583, 1983.

[82] Y. Minowa, T. Fujii, M. Nagai, T. Ochiai, K. Sakoda, K. Hirao, and K. Tanaka. Evaluation of effective electric permittivity and magnetic permeability in metamaterial slabs by terahertz time-domain spectroscopy. *Optics Express*, 16(7):4785–4796, 2008.

[83] H. T. Miyazaki and Y. Kurokawa. Squeezing visible light waves into a 3-nm-thick and 55-nm-long plasmon cavity. *Physical Review Letters*, 96(9):097401, 2006.

[84] E. Moreno, F. J. Garcia-Vidal, S. G. Rodrigo, L. Martin-Moreno, and S. I. Bozhevolnyi. Channel plasmon-polaritons: modal shape, dispersion, and losses. *Opt. Lett.*, 31(23):3447–3449, Dec 2006.

[85] R. G. Mote, H.-S. Chu, P. Bai, and E.-P. Li. Compact and efficient coupler to interface hybrid dielectric-loaded plasmonic waveguide with silicon photonic slab waveguide. *Optics Communications*, 285(18):3709 – 3713, 2012.

[86] P. Muhlschlegel, H. J. Eisler, O. J. F. Martin, B. Hecht, and D. W. Pohl. Resonant optical antennas. *Science*, 308(5728):1607–1609, 2005.

[87] W. Murray, S. Astilean, and W. Barnes. Transition from localized surface plasmon resonance to extended surface plasmon-polariton as metallic nanoparticles merge to form a periodic hole array. *Physical Review B*, 69(16):165407, 2004.

[88] J. Nakamura. *Image sensors and signal processing for digital still cameras*. CRC Press, Boca Raton, 2005.

[89] S. M. Nie and S. R. Emery. Probing single molecules and single nanoparticles by surface-enhanced raman scattering. *Science*, 275(5303):1102–1106, 1997.

[90] T. Nikolajsen, K. Leosson, I. Salakhutdinov, and S. I. Bozhevolnyi. Polymer-based surface-plasmon-polariton stripe waveguides at telecommunication wavelengths. *Applied Physics Letters*, 82(5):668–670, 2003.

[91] M. Noginov, L. Gu, J. Livenere, G. Zhu, A. Pradhan, R. Mundle, M. Bahoura, Y. A. Barnakov, and V. Podolskiy. Transparent conductive oxides: Plasmonic materials for telecom wavelengths. *Applied Physics Letters*, 99(2):021101–021101, 2011.

[92] I. V. Novikov and A. A. Maradudin. Channel polaritons. *Phys. Rev. B*, 66:035403, Jun 2002.

[93] L. Novotny and C. Hafner. Light-propagation in a cylindrical waveguide with a complex, metallic, dielectric function. *Physical Review E*, 50(5):4094–4106, 1994.

[94] S. M. Orbons, A. Roberts, D. N. Jamieson, M. I. Haftel, C. Schlockermann, D. Freeman, and B. Luther-Davies. Extraordinary optical transmission with coaxial apertures. *Applied Physics Letters*, 90(25):10896–10904, 2007.

[95] E. Ozbay. Plasmonics: Merging photonics and electronics at nanoscale dimensions. *Science*, 311(5758):189–193, 2006.

[96] D. Pacifici, H. J. Lezec, L. A. Sweatlock, R. J. Walters, and H. A. Atwater. Universal optical transmission features in periodic and quasiperiodic hole arrays. *Optics Express*, 16(12):9222–9238, 2008.

[97] E. D. Palik and G. Ghosh. *Handbook of optical constants of solids*. Academic Press, Orlando, 1985.

[98] S. Palomba and L. Novotny. Nonlinear excitation of surface plasmon polaritons by four-wave mixing. *Physical review letters*, 101(5):056802, 2008.

[99] D. Pan, H. Wei, and H. Xu. Optical interferometric logic gates based on metal slot waveguide network realizing whole fundamental logic operations. *Opt. Express*, 21(8):9556–9562, Apr 2013.

[100] L. Pan and D. B. Bogy. Data storage: Heat-assisted magnetic recording. *Nature Photonics*, 3(4):189–190, 2009.

[101] C. G. Parazzoli, R. B. Greegor, K. Li, B. E. C. Koltenbah, and M. Tanielian. Experimental verification and simulation of negative index of refraction using snell's law. *Physical Review Letters*, 90(10):107401, 2003.

[102] J. Parsons, E. Hendry, C. P. Burrows, B. Auguie, J. R. Sambles, and W. L. Barnes. Localized surface-plasmon resonances in periodic nondiffracting metallic nanoparticle and nanohole arrays. *Physical Review B*, 79(7):073412, 2009.

[103] J. B. Pendry. Negative refraction makes a perfect lens. *Physical Review Letters*, 85(18):3966–3969, 2000.

[104] J. B. Pendry, A. J. Holden, D. J. Robbins, and W. J. Stewart. Magnetism from conductors and enhanced nonlinear phenomena. *Ieee Transactions on Microwave Theory and Techniques*, 47(11):2075–2084, 1999.

[105] J. B. Pendry, D. Schurig, and D. R. Smith. Controlling electromagnetic fields. *Science*, 312(5781):1780–1782, 2006.

[106] J. Pitarke, V. Silkin, E. Chulkov, and P. Echenique. Theory of surface plasmons and surface-plasmon polaritons. *Reports on progress in physics*, 70(1):1, 2007.

[107] E. Popov, M. Neviere, S. Enoch, and R. Reinisch. Theory of light transmission through subwavelength periodic hole arrays. *Physical Review B*, 62(23):16100–16108, 2000.

[108] H. Raether. Surface plasmons on smooth and rough surfaces and on gratings. *Springer tracts in modern physics*, 111, 1988.

[109] S. Ravets, J.-C. Rodier, B. Ea Kim, J.-P. Hugonin, L. Jacubowiez, and P. Lalanne. Surface plasmons in the young slit doublet experiment. *JOSA B*, 26(12):B28–B33, 2009.

[110] N. Rotenberg, M. Spasenović, T. Krijger, B. Le Feber, F. García de Abajo, and L. Kuipers. Plasmon scattering from single subwavelength holes. *Physical Review Letters*, 108(12):127402, 2012.

[111] J. Salvi, M. Roussey, F. I. Baida, M. P. Bernal, A. Mussot, T. Sylvestre, H. Maillotte, D. Van Labeke, A. Perentes, I. Utke, C. Sandu, P. Hoffmann, and B. Dwir. Annular aperture arrays: study in the visible region of the electromagnetic spectrum. *Optics Letters*, 30(13):1611–1613, 2005.

[112] M. Sandtke and L. Kuipers. Slow guided surface plasmons at telecom frequencies. *Nature Photonics*, 1(10):573–576, 2007.

[113] G. Schider, J. R. Krenn, A. Hohenau, H. Ditlbacher, A. Leitner, F. R. Aussenegg, W. L. Schaich, I. Puscasu, B. Monacelli, and G. Boreman. Plasmon dispersion relation of Au and Ag nanowires. *Physical Review B*, 68(15):155427, 2003.

[114] V. M. Shalaev. Optical negative-index metamaterials. *Nature Photonics*, 1(1):41–48, 2007.

[115] V. M. Shalaev, W. S. Cai, U. K. Chettiar, H. K. Yuan, A. K. Sarychev, V. P. Drachev, and A. V. Kildishev. Negative index of refraction in optical metamaterials. *Optics Letters*, 30(24):3356–3358, 2005.

[116] G. Sharma, W. Wu, and E. Daa. The ciede2000 color-difference formula: Implementation notes, supplementary test data, and mathematical observations. *Color Research and Application*, 30(1):21–30, 2005.

[117] R. A. Shelby, D. R. Smith, and S. Schultz. Experimental verification of a negative index of refraction. *Science*, 292(5514):77–79, 2001.

[118] P. Shi, G. Zhou, and F. S. Chau. Enhanced coupling efficiency between dielectric and hybrid plasmonic waveguides. *J. Opt. Soc. Am. B*, 30(6):1426–1431, Jun 2013.

[119] G. Shvets. Photonic approach to making a material with a negative index of refraction. *Physical Review B*, 67(3):035109, 2003.

[120] G. Si, Y. Zhao, H. Liu, S. Teo, M. Zhang, T. J. Huang, A. J. Danner, and J. Teng. Annular aperture array based color filter. *Applied Physics Letters*, 99(3):033105, 2011.

[121] D. R. Smith, W. J. Padilla, D. C. Vier, S. C. Nemat-Nasser, and S. Schultz. Composite medium with simultaneously negative permeability and permittivity. *Physical Review Letters*, 84(18):4184–4187, 2000.

[122] D. R. Smith, J. B. Pendry, and M. C. K. Wiltshire. Metamaterials and negative refractive index. *Science*, 305(5685):788–792, 2004.

[123] D. R. Smith, D. C. Vier, T. Koschny, and C. M. Soukoulis. Electromagnetic parameter retrieval from inhomogeneous metamaterials. *Physical Review E*, 71(3):036617, 2005. Part 2.

[124] Y. Song, J. Wang, Q. Li, M. Yan, and M. Qiu. Broadband coupler between silicon waveguide and hybrid plasmonic waveguide. *Opt. Express*, 18(12):13173–13179, Jun 2010.

[125] Y. Song, J. Wang, M. Yan, and M. Qiu. Efficient coupling between dielectric and hybrid plasmonic waveguides by multimode interference power splitter. *Journal of Optics*, 13(7):075002, 2011.

[126] B. Steinberger, A. Hohenau, H. Ditlbacher, A. L. Stepanov, A. Drezet, F. R. Aussenegg, A. Leitner, and J. R. Krenn. Dielectric stripes on gold as surface plasmon waveguides. *Applied Physics Letters*, 88(9):094104, 2006.

[127] M. I. Stockman. Nanofocusing of optical energy in tapered plasmonic waveguides. *Physical Review Letters*, 93(13):137404, 2004.

[128] J. A. Stratton. *Electromagnetic Theory*. McGraw-Hill, New York, 1st edition, 1941.

[129] J. Valentine, S. Zhang, T. Zentgraf, E. Ulin-Avila, D. A. Genov, G. Bartal, and X. Zhang. Three-dimensional optical metamaterial with a negative refractive index. *Nature*, 455(7211):376–379, 2008.

[130] D. Van Labeke, D. Gerard, B. Guizal, F. I. Baida, and L. Li. An angle-independent frequency selective surface in the optical range. *Optics Express*, 14(25):11945–11951, 2006.

[131] E. Verhagen, R. de Waele, L. Kuipers, and A. Polman. Three-dimensional negative index of refraction at optical frequencies by coupling plasmonic waveguides. *Physical review letters*, 105(22):223901, 2010.

[132] E. Verhagen, A. Polman, and L. Kuipers. Nanofocusing in laterally tapered plasmonic waveguides. *Optics Express*, 16(1):45–57, 2008.

[133] G. Veronis and S. Fan. Bends and splitters in metal-dielectric-metal subwavelength plasmonic waveguides. *Applied Physics Letters*, 87(13):131102, 2005.

[134] G. Veronis and S. Fan. Theoretical investigation of compact couplers between dielectric slabwaveguides and two-dimensional metal-dielectric-metal plasmonicwaveguides. *Opt. Express*, 15(3):1211–1221, Feb 2007.

[135] G. Veronis, S. E. Kocabas, D. A. Miller, and S. Fan. Modeling of plasmonic waveguide components and networks. *J. Comput. Theor. Nanosci*, 6(8):1808–1826, 2009.

[136] V. G. Veselago. Electrodynamics of substances with simultaneously negative values of epsilon and mu. *Soviet Physics Uspekhi-Ussr*, 10(4):509, 1968.

[137] V. S. Volkov, S. I. Bozhevolnyi, E. Devaux, and T. W. Ebbesen. Bend loss for channel plasmon polaritons. *Applied Physics Letters*, 89(14):143108, 2006.

[138] V. S. Volkov, S. I. Bozhevolnyi, E. Devaux, and T. W. Ebbesen. Compact gradual bends for channel plasmon polaritons. *Opt. Express*, 14(10):4494–4503, May 2006.

[139] V. S. Volkov, S. I. Bozhevolnyi, S. G. Rodrigo, L. Martín-Moreno, F. J. García-Vidal, E. Devaux, and T. W. Ebbesen. Nanofocusing with channel plasmon polaritons. *Nano Letters*, 9(3):1278–1282, 2013/05/12 2009.

[140] J. Wang, X. Guan, Y. He, Y. Shi, Z. Wang, S. He, P. Holmström, L. Wosinski, L. Thylen, and D. Dai. Sub-μm2 power splitters by using silicon hybrid plasmonic waveguides. *Opt. Express*, 19(2):838–847, Jan 2011.

[141] J. C. Weeber, M. U. Gonzalez, A. L. Baudrion, and A. Dereux. Surface plasmon routing along right angle bent metal strips. *Applied Physics Letters*, 87(22), 2005.

[142] A. Yariv, Y. Xu, R. Lee, and A. Scherer. Coupled-resonator optical waveguide: a proposal and analysis. *Optics Letters*, 24(11):711–713, 1999.

[143] S. Yokogawa, S. Burgos, and H. Atwater. Plasmonic color filters for CMOS image sensor applications. *Nano Letters*, 12(8):4349–4354, 2012.

[144] S. Zhang, W. J. Fan, N. C. Panoiu, K. J. Malloy, R. M. Osgood, and S. R. J. Brueck. Experimental demonstration of near-infrared negative-index metamaterials. *Physical Review Letters*, 95(13):137404, 2005.